

CONJUGATED METALLOPOLYMERS CONTAINING
2,2'-BITHIAZOLE

CENTRE FOR NEWFOUNDLAND STUDIES

TOTAL OF 10 PAGES ONLY
MAY BE XEROXED

(Without Author's Permission)

BRIAN MacLEAN





National Library
of Canada

Acquisitions and
Bibliographic Services

395 Wellington Street
Ottawa ON K1A 0N4
Canada

Bibliothèque nationale
du Canada

Acquisitions et
services bibliographiques

395, rue Wellington
Ottawa ON K1A 0N4
Canada

Your file *Votre référence*
ISBN: 0-612-89696-X
Our file *Notre référence*
ISBN: 0-612-89696-X

The author has granted a non-exclusive licence allowing the National Library of Canada to reproduce, loan, distribute or sell copies of this thesis in microform, paper or electronic formats.

L'auteur a accordé une licence non exclusive permettant à la Bibliothèque nationale du Canada de reproduire, prêter, distribuer ou vendre des copies de cette thèse sous la forme de microfiche/film, de reproduction sur papier ou sur format électronique.

The author retains ownership of the copyright in this thesis. Neither the thesis nor substantial extracts from it may be printed or otherwise reproduced without the author's permission.

L'auteur conserve la propriété du droit d'auteur qui protège cette thèse. Ni la thèse ni des extraits substantiels de celle-ci ne doivent être imprimés ou autrement reproduits sans son autorisation.

In compliance with the Canadian Privacy Act some supporting forms may have been removed from this dissertation.

Conformément à la loi canadienne sur la protection de la vie privée, quelques formulaires secondaires ont été enlevés de ce manuscrit.

While these forms may be included in the document page count, their removal does not represent any loss of content from the dissertation.

Bien que ces formulaires aient inclus dans la pagination, il n'y aura aucun contenu manquant.

Canada

Conjugated Metallopolymers Containing 2,2'-Bithiazole

by

Brian MacLean

Honours Thesis, Dalhousie University
Halifax, Nova Scotia 1995
B.Sc. (Adv. Major), St. Francis Xavier University
Antigonish, Nova Scotia 1994

A thesis submitted to the School of Graduate Studies
in partial fulfillment of the requirements
for the degree of Doctor of Philosophy

Department of Chemistry
Memorial University of Newfoundland
St. John's, Newfoundland, Canada
December, 2002

Abstract

Ruthenium and osmium conjugated metallopolymers containing a bithiophene-co-bithiazole backbone have been synthesized and their electrochemistry investigated. This relatively new class of materials has demonstrated enhanced rates of charge transport relative to redox metallopolymers in which a saturated organic network connects pendant metal complexes. Applications requiring fast electrochemistry, such as molecular switching and electrocatalysis, clearly can benefit from this enhancement.

Electropolymerization from boron trifluoride diethyletherate (BF_3OEt_2) permitted facile deposition of polymer films for electrochemical experiments. Impedance spectroscopy has been used to investigate electron transport rates in these metallopolymers. $D_e C_M^{-2}$ was found to be over 20 times greater in poly-[Ru(5,5'-bis(2-thienyl)-2,2'-bithiazole)(bpy) $_2^{3+/2+}$] than in poly-[Ru((6,6'-bibenzimidazole-2,2'-diyl)-2,5-pyridine)(bpy) $_2^{3+/2+}$] as a result of better energy matching of the ruthenium t_{2g} orbital with the HOMO band in the poly[5,5'-bis(2-thienyl)-2,2'-bithiazole] backbone. A hole-type mechanism of superexchange is proposed for this system.

Acknowledgements

I would like to take this opportunity to thank the people who have helped me in my research, my learning, and in my journey towards this long awaited goal. I cannot begin with anyone other than my supervisor, Dr. Peter Pickup, and I probably couldn't fit all the thank you's I owe him between the covers of this work. I'd like to start by thanking him for his guidance and for his patience (a lot). I also thank him for his help during the latter part of my program, and for his friendship.

I would never have gotten to this point without the help from those closest to me. My parents have done more for me over the years than I can ever repay. Sherry has been with me through all of this, raising our daughter in my absence. I am fortunate to have them in my life.

The research group I've worked with in my years here has never been dull. The collection of interesting and intelligent people that I've had the pleasure of working with on a daily basis made the workplace very tolerable and sometimes a lot of fun. Thanks for all their help and for a lot of good memories.

Thank you to my supervisory committee members, Dr. Graham Bodwell and Dr. Niall Gogan, for their assistance and guidance, to my course instructors, to Dave Miller (NMR), Dr. Brian Gregory and Marion Baggs (MS) for their help with data acquisition, and to the kind people who work in the general office. Finally, the financial support of the Chemistry Department and the School of Graduate Studies is gratefully acknowledged.

Table of Contents

Title	i
Abstract	ii
Acknowledgements	iii
Table of Contents	iv
List of Figures	x
List of Schemes	xvii
List of Tables	xix
Glossary of Abbreviations	xx
Glossary of Symbols	xxii
Chapter 1 - An Introduction to Conjugated Metallopolymers	1
1.1 Conjugated Organic Polymers - A Brief Introduction	2
1.2 Classifications of Electroactive Polymer Systems	3
1.2.1 Redox Polymers	3
1.2.2 Conjugated Polymers	5
1.3 Synthetic Routes to Conjugated Polymers	10
1.4 Conjugated Polymers based on 2,2'-bithiazole	13
1.5 Conjugated Metallopolymers	15
1.6 Literature on Conjugated Metallopolymers	19

1.6.1	2,2'-Bithiazole Based Metallopolymers	19
1.6.2.1	2,2'-Bipyridine-based Materials	22
1.6.2.2	Bipyridine-bithiophene Copolymers	24
1.6.3	Benzimidazole-based Materials	36
1.6.4	Other Conjugated Metallopolymers	41
1.7	Goals	44
Chapter 2 - Syntheses of Monomers, Polymers, and Transition		47
Metal Complexes		
2.1	Chemicals and Instrumentation	48
2.2	Synthesis	49
2.2.1	Strategies to Electropolymerizable Ligands	49
2.2.2	Starting Materials	55
2.2.2.1	2,2'-Bithiazole, 6 (btz)	55
2.2.2.2	4,4'-Dimethyl-2,2'-bithiazole, 33 (bmtz)	56
2.2.2.3	5,5'-Dibromo-2,2'-bithiazole, 34	56
2.2.2.4	5,5'-Dibromo-4,4'-dimethyl-2,2'-bithiazole, 35	57
2.2.2.5	5,5'-Bis(trimethylstannyl)-2,2'-bithiazole, 36	58
2.2.2.6	2-Thiophene boronic acid, 37	59
2.2.2.7	5-Tributylstannyl-2,2'-bithiophene, 38	60
2.2.2.9	2-Tributylstannyl-3,4-(ethylenedioxy)thiophene, 39	61

2.2.3	Metal Salts	62
2.2.3.1	<i>Cis</i> -Bis(2,2'-bipyridine- <i>N,N'</i>) dichlororuthenium(II), 40	62
2.2.3.2	<i>Cis</i> -Bis(2,2'-bipyridine- <i>N,N'</i>)dichloroosmium(II)	62
2.2.3.2.1	<i>Cis</i> -Bis(2,2'-bipyridine- <i>N,N'</i>) dichloroosmium (III) chloride dihydrate,	63
	41	
2.2.3.2.2	<i>Cis</i> -Bis(2,2'-bipyridine- <i>N,N'</i>) dichloroosmium(II), 42	63
2.2.4	Bithiazole Monomers	64
2.2.4.1	5,5'-Bis(2-thienyl)-2,2'-bithiazole, 8	64
2.2.4.2	5,5'-Bis(2-thienyl)-4,4'-dimethyl-2,2'-bithiazole, 9	65
2.2.4.3	5,5'-Bis(2,2'-bithiophene)-4,4'-dimethyl-2,2'-bithiazole, 43	66
2.2.4.4	5,5'-Bis(5-3,4-(ethylenedioxy)thienyl)-4,4'-dimethyl-2,2'-bithiazole, 44	67
2.2.5	Transition Metal Complexes	69
2.2.5.1	Tris(2,2'-bithiazole)ruthenium(II) hexafluorophosphate, Ru(btz) ₃ (PF ₆) ₂	69
2.2.5.2	Bis(2,2'-bipyridine)[2,2'-bithiazole]ruthenium(II) perchlorate,	70
	Ru(btz)(bpy) ₂ (PF ₆) ₂	
2.2.5.3	Bis(2,2'-bipyridine)[5,5'-bis(2-thienyl)-2,2'-bithiazole]ruthenium(II)	71
	perchlorate, Ru(btbtz)(bpy) ₂ (PF ₆) ₂	
2.2.5.4	Bis(2,2'-bipyridine)[5,5'-bis(2-thienyl)-2,2'-bithiazole]osmium(II)	72
	perchlorate, Os(btbtz)(bpy) ₂ (PF ₆) ₂	
2.2.5.5	Bis(2,2'-bipyridine)[5,5'-bis(2-thienyl)-4,4'-dimethyl-2,2'-	73
	bithiazole]ruthenium(II) perchlorate, Ru(btbmtz)(bpy) ₂ (PF ₆) ₂	
2.2.5.6	Bis(2,2'-bipyridine)[5,5'-bis(2-thienyl)-4,4'-dimethyl-2,2'-	74

	bithiazole]osmium(II) perchlorate, Os(btbmtz)(bpy) ₂ (ClO ₄) ₂	
2.2.5.7	Bis(2,2'-bipyridine)[5,5'-bis(3-methoxy-2-thienyl)-4,4'-dimethyl-2,2'- bithiazole]osmium(II) perchlorate, Os(bmtbmtz)(bpy) ₂ (PF ₆) ₂	74
2.2.6	Conjugated Organic Polymers	75
2.2.6.1	Poly[5,5'-bis(2-thienyl)-2,2'-bithiazole], poly- btbtz	75
Chapter 3 - Electronic and Electrochemical Characterization of		77
2,2'-bithiazole based Monomers and Polymers		
3.1	Experimental	78
3.2	Monomers Containing 2,2'-bithiazole	78
3.3	Electronic Absorption Spectroscopy	79
3.3.1	Monomers	81
3.3.2	Polymers	84
3.3.3	Effect of Acid	86
3.4	Semi-empirical Calculations	89
3.5	Cyclic voltammetry	91
3.5.1	Cyclic Voltammetry of Monomers	91
3.5.2	Electropolymerization	94
3.5.3	Polymer Films	96

Chapter 4 - Characterization of Transition Metal Complexes	101
4.1 Syntheses of 2,2'-bithiazole Complexes	102
4.2 Metal Complexes for Electropolymerization	102
4.3 Characterization	104
4.3.1 ESI-MS of $M(L)(bpy)_2^{2+}$ Complexes	104
4.3.2 1H NMR of $M(L)(bpy)_2^{2+}$ Complexes	108
4.3.3 Crystal Structure for $Ru(\mathbf{btbmtz})(bpy)_2(PF_6)_2$	114
4.4 Electronic and Electrochemical Characterization	116
4.4.1 Electronic Absorption Spectroscopy	116
4.4.2 Cyclic Voltammetry of $M(L)(bpy)_2^{2+}$ Complexes	121
4.5 Electropolymerization of $M(L)(bpy)_2^{2+}$ Complexes	128
Chapter 5 - Electrochemistry and Electron Transport Studies of Conjugated Metallopolymers	137
5.1 Conjugated Metallopolymer Films	138
5.2 Electrochemical Studies on Metallopolymer Films	138
5.3 Electron Transport in Ruthenium and Osmium Metallopolymers	150
5.3.1 $D_e C_M^{-2}$	150

5.3.2	Methods for Obtaining $D_e C_M^{-2}$	152
5.3.2.1	AC Impedance Background	153
5.4	AC Impedance Experiments and Results	160
5.4.1	Polymer Film Preparation	160
5.4.2	Poly-Os(btbtz)(bpy) ₂ ²⁺	162
5.3.3	Poly-Ru(btbtz)(bpy) ₂ ²⁺	168
5.3.4	Superexchange Pathways	169
5.3.5	Comparisons with Literature Systems	170
Chapter 6 - Summary		179
References		182
Appendices		
A	Cyclic Voltammetry	189
B	¹ H NMR Spectra	197
C	¹³ C NMR Spectra	219
D	Electronic Absorption Spectra	226
E	Crystal Structure Data	229

List of Figures

1.1	Cyclic voltammogram for the redox polymer poly[Fe(5-amino-1,10-phenanthroline) ₃] ^{3+/2+} in CH ₃ CN/0.2M Et ₄ NClO ₄ , scanned from 100 - 900 mV.s ⁻¹	5
1.2	Bond reorganization during p-doping of polyparaphenylene	6
1.3	Changes in a conducting polymer's band structure with oxidation	6
1.4	Cyclic voltammogram of a conjugated polymer, polypyrrole.	9
1.5	Anodic dimerization of thiophene	12
1.6	Electron transport mechanisms in conjugated metallopolymers: A , outer sphere electron transfer (self-exchange); B , polymer mediated pathway; C , superexchange through a π -conjugation network	17
1.7	Hole and electron type superexchange	18
1.8	Valence band energy with position in poly- 8	21
1.9	Electrochemistry of (a) Ru- 5 material, (b) poly- 4 , (c) Ru(bpy) ₃ in CH ₃ CN/0.1 M Et ₄ NClO ₄	23
1.10	Cyclic voltammetry and conductivity profiles (<i>i</i> _a α conductivity) of: A) poly- 16 ; B) poly-Ru(16) ₃	26
1.11	Cyclic voltammetry of and conductivity of A: poly- 20 ; B: poly-Rot(20 , Zn); C: poly-Rot(20 ,Cu). Inset: poly-Rot(16 ,Cu)	31
1.12	Cyclic voltammetry (---) and conductivity (- - -) of ladder-type	34

	polymers: poly- 22 -L (A); poly- 23 -L (B); poly- 21 (C)	
1.13	Interchain electron-hopping mechanism existing in poly- 23 -L	35
1.14	Cyclic voltammetry of a thin film of 25 ($v=100 \text{ mV s}^{-1}$) in $\text{CH}_3\text{CN}/0.1\text{M}$ Et_4NClO_4 containing <i>ca.</i> 50 mM HClO_4 (solid line) or <i>ca.</i> 5 mM Bu_4NOH (dashed line)	37
1.15	a) Cyclic voltammetry of 26 in 2:1 $\text{CH}_2\text{Cl}_2/\text{CH}_3\text{CN}$ containing 0.1 M Et_4NClO_4 + <i>ca.</i> 0.05M HClO_4 ; b) Conductivity vs potential. Thinner line represents reverse scan	39
1.16	Current vs alkali metal concentration at fixed potential for electrodes covered with poly- 28 in the presence of Li^+ , Na^+ , and K^+	42
1.17	Metal centers coordinated to bidentate sites of a polyconjugated backbone	45
1.18	Electrocatalysis of the reaction $\text{O} + \text{e}^- \rightarrow \text{R}$ by a metallopolymer coating	46
2.1	Aromatic region of the ^1H NMR spectrum for 42	54
2.2	^1H NMR of the solution obtained by treatment of poly(btbtz) powder with TFA-d_6	76
3.1	Potential energy diagram representing an absorbing bithiazole monomer in solution. Bottom curve - before light absorption. Top curve - after light absorption, a transition occurs from the ground vibrational level of the ground electronic state to the vibrational state directly above it	80

3.2	Electronic absorption spectra for the monomers in CH_2Cl_2 : — btbtz ; - - - btbmtz ; \diamond bmtbmtz	83
3.3	Electronic absorption spectra for bithiazole polymers on ITO electrodes: - poly- btbtz ; - - - poly- btbmtz ; \diamond poly- bmtbmtz	85
3.4	The effect of adding acid to btbtz : — btbtz in CH_3CN ; \diamond btbtz in $\text{CH}_3\text{CN} + \text{HClO}_4$	87
3.5	Effect of acid on poly- btbtz . — poly- btbtz on ITO electrode; \diamond poly- btbtz in conc. H_2SO_4	88
3.6	Cyclic Voltammetry of 10 mM btbtz in CH_2Cl_2 / 0.1M Bu_4ClO_4 . $A=0.0052 \text{ cm}^2$; $v=100 \text{ mV sec}$	92
3.7	Anodic polymerization of 5.5 mM btbtz with recurrent potential scans in CH_2Cl_2 / 0.1 M Bu_4NPF_6 ($v = 100 \text{ mV sec}^{-1}$). $A=0.0052 \text{ cm}^2$	95
3.8	Cyclic voltammetry of two poly- btbtz coated electrodes in CH_2Cl_2 / 0.1 M Bu_4NClO_4 : positive scan first, — ; negative scan first - - -	98
4.1	Simulation of molecular peak distribution for $\text{Ru}(\text{btbtz})(\text{bpy})_2^{2+}$	107
4.2	C_2 symmetry of the bis(2,2'-bipyridine) ruthenium and osmium complexes of the bithiazole ligands leads to splitting of the 2,2'- bipyridine resonances	108
4.3	^1H NMR (300 MHz) in CD_3OD for $\text{Os}(\text{bpy})_3^{2+}$ and $\text{Ru}(\text{bpy})_3^{2+}$. Inset: ^1H NMR for 2,2'-bipyridine in DMSO-d_6	110
4.4	^1H NMR (300 MHz) in CD_3OD for (bottom to top): $\text{Ru}(\text{bmtz})(\text{bpy})_2^{2+}$,	111

- Ru(**btbmtz**)(bpy)₂²⁺, and Os(**btbmtz**)(bpy)₂²⁺
- 4.5 COSY spectrum of Ru(**btmtz**)(bpy)₂²⁺ in CD₃OD. COSY data permits hydrogens of each ring on a bipyridine ligand to be differentiated. One dimensional representation is shown on top and left axes 112
- 4.6 X-ray crystal structure for Ru(**btbmtz**)(bpy)₂(PF₆)₂ crystals grown from acetone-H₂O 115
- 4.7 Electronic absorption spectra for **btbtz** (o), Ru(**btbtz**)(bpy)₂²⁺ (thin line), and Os(**btbtz**)(bpy)₂²⁺ (thick line) 118
- 4.8 Electronic absorption spectra of M(L)(bpy)₂²⁺ complexes in methanol. **btbmtz** (o); Ru(**btbmtz**)(bpy)₂²⁺ (thin line); Os(**btbmtz**)(bpy)₂²⁺ (thick line) 119
- 4.9 Cyclic voltammogram of ca. 5.5 mM Ru(**btbtz**)(bpy)₂²⁺ in CH₃CN/Et₄NClO₄ (ν = 100 mV sec⁻¹). A=0.0052 cm² 122
- 4.10 Cyclic voltammetry of Ru(bpy)₃Cl₂ (—) and Ru(**btz**)₃(PF₆)₃ (- - -) in CH₃CN / 0.1 M Et₄NClO₄ (ν = 100 mV sec⁻¹) 126
- 4.11 Cyclic voltammetry of ca. 5.5 mM Os(**btbtz**)(bpy)₂²⁺ in CH₃CN/0.1 M Et₄NClO₄ (ν = 100 mV sec⁻¹). A=0.0052 cm² 127
- 4.12 Attempted electropolymerization of ca 5.5 mM Ru(**btbtz**)(bpy)₂²⁺ in CH₃CN/ 0.1 M Et₄NClO₄ (ν = 100 mV sec⁻¹). A=0.0052 cm². Inset: electrochemistry of a Pt electrode after potential cycling in Ru(**btbtz**)(bpy)₂²⁺ solution 128
- 4.13 Polymerization of ca. 5.1 mM Os(**btbtz**)(bpy)₂²⁺ in CH₃CN / (0.1 M) 131

	Et ₄ NClO ₄ with 0.45 M BF ₃ OEt ₂ ($v = 100 \text{ mV sec}^{-1}$). $A=0.0052 \text{ cm}^2$.	
	Arrows show changes with increasing cycle number	
4.14	Electropolymerization of 5 mM Ru(btbtz)(bpy) ₂ ²⁺ in neat BF ₃ OEt ₂ ($v = 100 \text{ mV sec}^{-1}$). $A=0.0052 \text{ cm}^2$. Arrows indicate current growth with cycle number	133
4.15	Electropolymerization of <i>ca</i> 2.7 mM Os(btbtz)(bpy) ₂ ²⁺ in neat BF ₃ OEt ₂ ($v = 100 \text{ mV sec}^{-1}$). $A=0.0052 \text{ cm}^2$	134
4.16	Complexation by BF ₃ OEt ₂ produces an adduct with less net electron density on the polymerizable bithiazole ligand. Oxidation of this complex produces a less stable intermediate, preventing radical coupling	136
5.1	Cyclic voltammogram of poly- btbmtz (top) and poly-[Ru(btbmtz)(bpy) ₂ ^{3+/2+}] (bottom). Scan numbers indicated	140
5.2	Cyclic voltammogram of poly-[Ru(btbtz)(bpy) ₂ ^{3+/2+}] in CH ₃ CN/0.1 M Et ₄ NClO ₄ . Scan numbers are indicated	144
5.3	Cyclic voltammogram of poly-[Ru(btbmtz)(bpy) ₂ ^{3+/2+}] in CH ₃ CN/0.1 M Et ₄ NClO ₄	145
5.4	Cyclic voltammetry of poly-Os(btbtz)(bpy) ₂ ²⁺ (grown from CH ₃ CN / Et ₄ NClO ₄ / BF ₃ OEt ₂)	147
5.5	Cyclic voltammetry of poly-Os(btbtz)(bpy) ₂ ²⁺ (grown from neat BF ₃ OEt ₂)	148
5.6	Equivalent circuit diagram for a polymer coated electrode	154

- 5.7 Representation of an ideal complex plane impedance plot 156
- 5.8 Plot of $-Z''$ vs ω^{-1} to obtain low frequency capacitance for poly-Os(**btbtz**)(bpy)₂²⁺. Data collected in CH₃CN/0.1M Et₄NClO₄ at 0.8 V vs SSCE 159
- 5.9 Dependence of surface coverage (Γ), \square ($\times 10^8$ mol cm⁻²) and $D_s C_M^2$, \bullet ($\times 10^{14}$ mol² cm⁻⁴ s⁻¹) on polymerization time. Films were grown at a constant current density of 0.15 mA cm⁻² from ca. 2.2 mM Ru(**btbtz**)(bpy)₂(PF₆)₂ in BF₃·Et₂O and tested in CH₃CN/0.1M Et₄NClO₄ at 1.32 V vs SSCE 162
- 5.10 AC impedance of a poly-Os(**btbtz**)(bpy)₂²⁺ film at 0.75 V (\square), 0.8 V (\bullet) and 0.89 V (\blacksquare) and 1.00 V (\circ) in CH₃CN/0.1M Et₄NClO₄. $\Gamma = 2.2 \times 10^{-8}$ mol cm⁻² 164
- 5.11 Electronic resistance (R_e , \blacksquare) and low frequency impedance intercept (R_{High} , \circ) for potentials spanning the Os^{III/II} wave of poly-[Os(**btbtz**)(bpy)₂^{3+/2+}] in CH₃CN/0.1M Et₄NClO₄. $\Gamma = 2.2 \times 10^{-8}$ mol cm⁻². The relative invariance of R_{High} with potential is indicative of a film in which $R_e \gg R_c$. 165
- 5.12 Low frequency capacitance for potentials which straddle the Os^{3+/2+} process of a poly-Os[(**btbtz**)(bpy)₂^{3+/2+}] film in CH₃CN / 0.1M Et₄NClO₄. $\Gamma = 2.2 \times 10^{-8}$ mol cm⁻² 166
- 5.13 $D_s C_M^2$ of a poly-[Os(**btbtz**)(bpy)₂^{3+/2+}] film over 0.75 V to 1.05 V in CH₃CN / 0.1M Et₄NClO₄. $\Gamma = 2.2 \times 10^{-8}$ mol cm⁻² 167

- 5.14 Decrease of $D_e C_M^{-2}$ with potential (1.22 V to 1.5 V) across a Ru^{III} wave due to backbone deactivation. Experiment performed in $CH_3CN/0.1M Et_4NClO_4$, $\Gamma_M = 4 \times 10^{-8} \text{ mol cm}^{-2}$. The second point at 1.22 V shows $D_e C_M^{-2}$ after deactivation. Scan duration $\sim 60 \text{ s}$ 169
- 5.15 Orbital energy diagrams (not drawn to scale) for ruthenium metallopolymers possessing a poly[(6,6'-bibenzimidazole-2,2'-diyl)-2,5-pyridine] (poly-**bbim**) backbone (top) and a poly[5,5'-bis(2-thienyl)-2,2'-bithiazole] (poly-**btbtz**) backbone (bottom) 176
- 5.16 Overoxidized poly-Ru(**btbtz**)(bpy)₂²⁺ segment (**49**) and its conjugated enol form (**50**) 178

List of Schemes

1.1	Derivatization of poly- 8	20
1.2	Extension of bithiophene termini to yield a polymerizable Ru ²⁺ complex	25
1.3	Complexation of 19 and either 16 or 20 with M (Zn ²⁺ or Cu ⁺) to yield polymerizable metallorotaxane complexes	30
1.4	Two-step ladder polymer formation from 22 or 23	33
2.1	Synthetic routes to 4-ring bis(thienyl)bithiazole ligands.	51
2.2	Organotin route to 2,2'-bipyridine monomers 43 and 44	53
2.3	Complexation of a 4-ring bis(thienyl)bithiazole ligand	69
4.1	Deactivation of the poly-btbtz backbone by nucleophilic attack by trace H ₂ O results in a breakdown of the long-range π -conjugation	130

List of Tables

3.1	Onset of (λ_{on}) absorption (nm) for monomers in CH_2Cl_2	82
3.2	Comparison of peak absorbances for monomers and polymer films on ITO electrodes	85
3.3	HOMO and LUMO energies calculated at the AM1 level	90
3.4	Monomer oxidation and reduction potentials vs SSCE in $\text{CH}_2\text{Cl}_2/\text{Bu}_4\text{NClO}_4$	93
3.5	p-Doping and n-doping potentials for bithiazole-bithiophene copolymers	100
4.1	Isotopic distributions of ruthenium and osmium at natural abundance	106
4.2	Electronic absorption data for metal complexes in MeOH	120
4.3	Redox potentials (V vs SSCE) for metal complexes in $\text{CH}_3\text{CN}/\text{Et}_4\text{NClO}_4$ vs SSCE. $E_g = \text{difference between } \mathbf{L}_{\text{Ox}}$ and \mathbf{L}_{Red}	124
5.1	$D_s C_M^{-2}$ values for Pt coated electrodes for several metallopolymers in $\text{CH}_3\text{CN}/0.1\text{M Et}_4\text{NClO}_4$	174

Glossary of Abbreviations

BL	bridging ligand
bmbmtz	"5,5'-bis(3-methoxy-2-thienyl)-4,4'-dimethyl-2,2'-bithiazole"
bmtz	"4,4'-dimethyl-2,2'-bithiazole"
BP	boiling point
bpy	"2,2'-bipyridine"
btbmtz	"5,5'-bis(2-thienyl)-4,4'-dimethyl-2,2'-bithiazole"
btbtz	"5,5'-bis(2-thienyl)-2,2'-bithiazole"
btz	"2,2'-bithiazole"
COSY	correlation spectroscopy
CV	cyclic voltammetry/voltammogram
DEV	dual electrode voltammetry
DMF	<i>N,N</i> -dimethyl formamide
EDOT	3,4-ethylenedioxythiophene
EIS	electrochemical impedance spectroscopy
ESI	electrospray ionization
GPC	gel permeation chromatography
HOMO	highest occupied molecular orbital
IR	infrared
IT	intervalence transfer
ITO	indium tin oxide
LED	light emitting diode
LUMO	lowest unoccupied molecular orbital
MeOH	methanol
MLCT	metal-to-ligand charge transfer
MP	melting point
MS	mass spectrometry
NIR	near-infrared
NMR	nuclear magnetic resonance
ORTEP	Oak Ridge thermal ellipsoid plot
RDE	rotating disk electrode
RDV	rotating disk voltammetry
RF	radio frequency
Rot	rotaxane
SSCE	saturated sodium chloride calomel electrode
TFA	trifluoroacetic acid
THF	tetrahydrofuran
TLC	thin layer chromatography

TMS	tetramethylsilane
tth	"tetrathiophene"
UV-Vis	ultraviolet-visible
vpy	vinylpyridine
XPS	x-ray photoelectron spectroscopy

Glossary of Symbols

δ	chemical shift
Γ	surface coverage
λ	average electron-hopping distance
λ	wavelength
λ_{\max}	wavelength of peak absorption
λ_0	wavelength of absorption onset
v	scan speed
θ	phase angle
ρ	redox capacity
ω	frequency
A	electrode area
AC	alternating current
Ag/Ag ⁺	silver wire reference
Bu	butyl
C	capacitance
C _F	Faradaic capacitance
C _{Low}	low frequency capacitance
C _M	concentration of metal complex sites in metallopolymer film
C _{Ox}	concentration of oxidized sites
C _{Red}	concentration of reduced sites
C _{Tot}	total concentration of redox active sites
d	doublet
d	film thickness
DC	direct current
dd	double doublet
D _c	electron diffusion coefficient
e	electron charge
E	potential
e ⁻	electron
E _{1/2}	half-wave potential
E _g	bandgap
E ^{0'}	formal potential
E _{p,a}	anodic peak potential
E _{p,c}	cathodic peak potential
Et	ethyl
F	Faraday's constant
Fc/Fc ⁺	ferrocene internal reference
I	current
i _p	peak current

j	$(-1)^{j/2}$
j	current density
J	coupling constant
k_{ex}	second order rate constant for electron exchange
m	multiplet
m/z	mass-to-charge ratio
M	molarity
M^+	molecular ion
Me	methyl
M_n	average molecular weight
n	number of monomer units
n	number of electrons
Q	charge
R	ideal gas constant
R_e	electronic resistance
R_e	equilibrium nuclear separation
R_{high}	high frequency resistance
R_i	ionic resistance
R_{low}	low frequency resistance
R_s	solution resistance
s	singlet
t	triplet
T	absolute temperature
V	volume
Z	impedance
Z'	real impedance
Z''	imaginary impedance

Chapter 1

An Introduction to Conjugated Metallopolymers

1. Conjugated Organic Polymers - A Brief Introduction

The first account of a material that is now classed among conducting polymers was published in 1862 [1], on the electrodeposition of polyaniline from dilute sulphuric acid. Some fourteen years later, the charging/discharging properties of polyaniline were investigated [2]. It was not until the late 1970's, however, that significant interest in these materials developed. In 1977, the discovery that polyacetylene underwent a ten billion-fold increase in conductivity when doped with iodine [3] sparked an explosion of research on the topic, so much so that it has evolved into a highly interdisciplinary field, embracing chemistry, physics, mathematics, theoretical and computational science, and more recently, biology and medicine [4]. The pioneering research of Heeger, MacDiarmid, and Shirakawa on the synthesis and properties of polyacetylene culminated recently with the 2000 Nobel Prize in Chemistry.

Electrical conductivity is not the only interesting property these polymers display. Studies on systems possessing a polyacetylene architecture (i.e., polymers possessing a high degree of linear π -conjugation), show that these materials may also exhibit non-linear optical [5], charge storage [6], and electrochromic properties [7], as well as mechanical attributes such as high tensile strength and resistance to high temperatures [5]. These qualities have translated into a diverse scope of applications for conducting polymers [8, 9], producing forays into such areas as drug delivery [10], electroanalysis [11], national defense [12], corrosion protection [4], and energy technology [13], to name a few. Some of the more novel proposed applications include molecular-level electronic

devices [8], artificial muscles [14], electrically conducting textiles [4], and membrane separations [15]. It is likely that the future will see this list grow even more as the properties of conducting polymer systems become better understood.

1.2 Classifications of Electroactive Polymer Systems

It is perhaps a good idea to distinguish between two important types of electroactive polymers, in order to limit confusion between closely related terms. The following classification is based on the mechanism of electron movement proposed for each system.

1.2.1 Redox Polymers

Prior to 1977, reports of electronically conducting polymer materials pertained to polymer chains having pendant electroactive groups. Electronic processes in these systems are governed by electron hopping, or self-exchange, between the fixed, isolated, electrochemically active sites and are characterized by the voltammogram shown in Figure 1.1. A wide variety of conducting polymers have been reported which conform to this architecture, and have been assigned the general label "redox polymers." Poly[1-methyl-4-vinylpyridinium] (**1**) is an example of an entirely organic redox polymer, while polyvinylferrocene (**2**) represents a system possessing transition metal-based redox sites. The latter polymer, a hybrid structure consisting of an organic backbone and a transition metal complex, is commonly referred to as a metallopolymer.

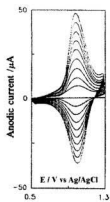
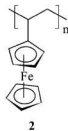
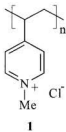


Figure 1.1: Cyclic voltammogram for the redox polymer poly[Fe(5-amino-1,10-phenanthroline)]^{3+/2+} in CH₃CN/0.2M Et₄NClO₄, scanned from 100 - 900 mV.s⁻¹. Reprinted from [16] with permission from

J. Electroanal. Chem. **1994**, 365, 289. Copyright 1994 Elsevier Science.



Electron transport in redox polymers is governed by the equation

$$D_e = k_{ex} \lambda^2 (C_{Ox} + C_{Red}) \quad (1.1)$$

where D_e is the electron diffusion coefficient, k_{ex} is the homogeneous second order rate constant for electron exchange between Ox and Red (the fixed, oxidized and reduced redox sites in the polymer), λ is the average distance an electron hops in the redox polymer, and C_{Ox} and C_{Red} are the concentrations of oxidized and reduced redox sites ($C_{Tot} = C_{Ox} + C_{Red}$) [4]. Typically, D_e values of $10^{-10} \text{ cm}^2 \text{ s}^{-1}$ have been reported for redox polymers, which can often correspond to a conductivity that is associated with the counterion movement which accompanies oxidation/reduction.

1.2.2 Conjugated Polymers

The feature that distinguishes conjugated organic polymers from redox polymers is their extensively delocalized π -orbital skeletons, which facilitate one-dimensional electron (hole) transfer along the backbone. This contrasts with the highly localized electrochemistry of redox polymers. For redox systems, electron hopping is through outer-sphere exchange between fixed, electroactive sites, while for conjugated organic polymers, charge transport occurs *via* movement of charged defects created during oxidation or reduction of the neutral polymer [1] (Figure 1.2). Metal complexes have been grafted onto conjugated organic polymer chains, mixing the d-orbitals of the metal with the π -network of the polymer. These so-called conjugated metallopolymers (also

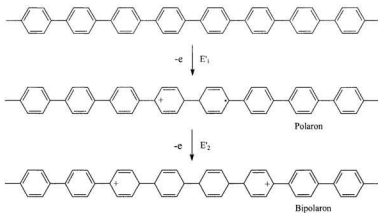


Figure 1.2: Bond reorganization during p-doping of poly(paraphenylene).

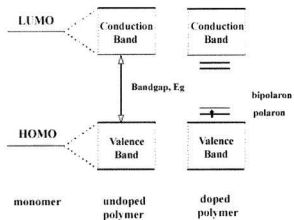


Figure 1.3: Changes in a conducting polymer's band structure with oxidation [18]. Reprinted with permission

from Modern Aspects of Electrochemistry, Vol. 33. Copyright 1999, Plenum Press.

called "redox/conjugated polymer hybrids") differ from the polyvinylferrocene redox metallopolymer discussed above in that there is no saturated linkage to isolate electronically redox active sites from one another.

Conjugated organic polymers are normally good insulators, behaving as wide bandgap semiconductors. It is not until their π -systems are oxidized ("p-doped") or reduced ("n-doped") that they display the electronic properties which make them so interesting. A modified band theory has been employed to explain why conductivity is so greatly enhanced by "doping" in conducting polymer systems [17]. For a material to be conductive, electrons must be promoted from a non-excited energy level (valence band) to an excited state (conduction band), the difference between these energy bands being designated the "energy bandgap." Thus, electronic movement arises from a partially empty valence band and/or a partially occupied conduction band (Figure 1.3). In a good electronic conductor (for example, a metal), the conduction band energy lies just above the energy of the valence band (i.e., zero bandgap). In the case of a semiconductor, an electron must acquire sufficient energy to reach the conduction band. The polymerization of conjugated monomers creates band structures from the discrete HOMO and LUMO energies of the monomer, due to the extended conjugation that is produced. Bandgaps in conjugated polymer systems are generally too large for these materials to exhibit appreciable intrinsic conductivities; however, intermediate energy states that are created during the oxidation or reduction of the polymer can significantly reduce the energy required for charge movement to occur. These new energy states are associated with

structural deformations accompanying polymer oxidation (or reduction). Oxidation results in the formation of an energy state just above the valence band due to the creation of a cation radical species called a "polaron." Correspondingly, new energy states below the conduction band are created during n-doping. With heavier doping, these excited states broaden to form intermediate energy bands. For p-doping, this results in a dication species, a "bipolaron," delocalized over several repeat units in the polymer. These charge carriers are highly mobile, and it is seen that the conductivity of conjugated polymers increases in proportion to their number.

A comparison of a cyclic voltammogram of a conjugated polymer (Figure 1.4) with that of the redox polymer (Figure 1.1) demonstrates interesting differences. The most notable is the shape of the voltammogram. The broader, less descript conjugated polymer electrochemistry owes to a larger number of available electronic energy states. This array of energy states is attributable to a wide variety of chain lengths, ranging between shorter chain oligomers to longer polymer systems, each having different oxidation and reduction characteristics. The observed response is thus a superposition of many closely spaced redox waves. Cross-linking and irregularities in chain connectivity offer an additional explanation.

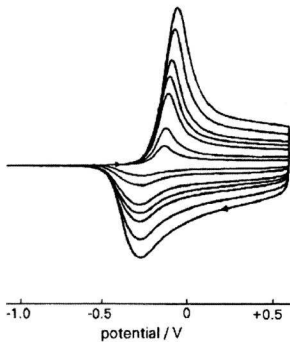


Figure 1.4: Cyclic voltammogram of a conjugated polymer, polypyrrole. Reprinted from [19] with permission from *J. Chem. Soc., Chem. Commun.* **1980**, 397. Copyright 1980 Royal Society of Chemistry.

For the redox polymer film, the electrochemistry behaves as for experiments conducted in a thin layer cell (peak current linearly related to scan speed, symmetric wave shape), with a current maximum localized close to the formal potential for the redox active sites of the polymer. This is described by:

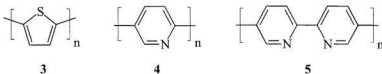
$$i_p = \frac{n^2 F^2 v V C_{\text{Tot}}}{4RT} \quad (1.2)$$

where i_p is the peak current, n is the number of electrons involved for the redox reaction, F is Faraday's constant (C mol^{-1}), v is the scan speed (V s^{-1}), V is the volume (cm^3), $C_{\text{Tot}} = C_{\text{Ox}} + C_{\text{Red}}$, R is the gas constant, and T is the temperature.

1.3 Synthetic Routes to Conjugated Polymers

A significant volume of research has been reported for conjugated polymers synthesized by chemical routes. Currently, some of the most interesting research in the field, from a synthetic view, involves the attachment of functionalities to the monomer to obtain polymers having desirable qualities like better solubility [20], controlled molecular weights [21, 22], higher doping levels [23], and increased regioregularity [20, 24]. Lowering of the electrochemical bandgap has also been accomplished, through the design of polymers with special skeletal architectures, and sometimes by functionalization with alkyl groups [23, 25]. Some of these alterations can affect chain conjugation length, and thus can improve the polymer's conductivity.

Conducting polymers can be synthesized by a variety of chemical routes. Oxidants such as Fe^{3+} have frequently been used to create polythiophenes and polypyrroles [26].



Zerivalent nickel polycondensations have been successfully employed in the syntheses of polyheteroaromatic systems such as poly(thiophene-2,5-diyl) (**3**), poly(pyridine-2,5-diyl) (**4**), and poly(2,2'-bipyridine-5,5'-diyl) (**5**) [27]. Grignard couplings have been utilized in the preparation of polyesters derived from oligothiophenes, producing systems having electroactive and photoactive moieties [22]. Dozens of synthetic routes to polyacetylenes are known [4]. Unfortunately, for all these routes, characterization is often not straightforward. Sometimes, tedious steps must be undertaken even to coat electrodes for electrochemical analyses. Low solubilities in commonly used solvents can sometimes lead to characterizations employing strong acids like H_2SO_4 and CF_3COOH [28].

One of the more useful synthetic approaches for the preparation of electroactive polymers does not involve chemical reagents to promote polymerization, but is carried out at an electrode-solution interface. Electropolymerizations have long been known, and are the preferred method for film preparation for several reasons. An obvious advantage over chemical routes is the avoidance of separations and purifications, which must be undertaken in order to remove catalysts, reactants, and side products. Speed and ease of product preparation are two more benefits of the electrochemical route, but probably the greatest advantage of this technique is that it allows one to bypass solubility problems commonly encountered with high molecular weight materials, permitting film growth on

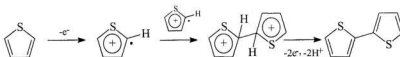


Figure 1.5: Anodic dimerization of thiophene.

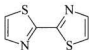
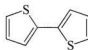
the electrode surface for immediate electrochemical characterization. Since film growth can be regulated by several methods (e.g. by regulating the quantity of charge passed during the polymerization step), highly regular films of controlled dimensions are possible, and are produced in their conducting (doped) form.

Although there have been several mechanisms proposed for oxidative electropolymerization [1], it is now generally accepted that this is a $E(CCE)_x$ -type process, which involves radical coupling of the products of monomer oxidation (Figure 1.5) with subsequent reoxidations and couplings. It can be seen that electropolymerization is possible only for monomers which produce stable oxidation intermediates. Less delocalized monomers and electron-deficient systems are not good candidates, as the cation radicals thus formed undergo nucleophilic attack at the high potentials required for their generation. A good comparison exists between thiophene and thiazole. Although structurally similar, thiophene has been reported to undergo facile electropolymerization, while for thiazole, no film formation is possible [29]. Another electrochemical route, involving reduction of a Ni^{2+} catalyst in the presence of the dihalogenated monomer, also permits polymerization [30, 31]. The method shows promise for monomers which are unable to be polymerized at an anode [32, 33]. It may also be superior in that monomer coupling could be more controlled.

1.4 Conjugated Polymers based on 2,2'-bithiazole

A conjugated polymer containing the 2,2'-bithiazole moiety (**6**) is interesting from several standpoints. Structurally, the bicycle resembles 2,2'-bithiophene (**7**). Polythiophenes and their derivatives are popular systems for electrochemical studies, in part due to facile film formation, good structural stabilities, and excellent conductivities. The introduction of an imine functionality into a thiophene chain has been found to significantly reduce conductivity. While polythiophenes having conductivities of 10^5 S cm^{-1} are known [4], chemically synthesized poly(2-thiazol-5-yl) exhibited a much lower conductivity (10^{-8} to $10^{-7} \text{ S cm}^{-1}$) when either p-doped or n-doped [29]. A broad absorption spectrum for this polymer, over the range of 0.8 eV - 4.0 eV, with an absorption maximum in the region of 550-600 nm, was found. The authors concluded that the broad nature of the absorbance suggested the presence of kink defects. A more recent report concerning poly(4,4'-alkyl bithiazoles) employed chemical polycondensations to generate more regular polymers having high molecular weights ($M_n = 22,000$) [34]. Subsequent studies on these materials showed that they are stable to n-doping, and that while in the neutral state they are insulating, n-doping greatly enhances their electron transport properties [35].

Electrochemical polymerization of 2,5-bis(2-thienyl)-thiazole resulted in a bithiophene-thiazole copolymer, with which comparisons to electrogenerated polythiophene films are much better suited. It was found that this copolymer displayed a

**6****7**

conductivity of $6 \times 10^{-5} \text{ S cm}^{-1}$, indicating that the introduction of a nitrogen atom into the polythiophene framework greatly hinders the movement of charge carriers [36].

A copolymer consisting of bithiazole-bithiophene segments was developed by Wolf and Wrighton, from 5,5'-bis(2-thienyl)-2,2'-bithiazole (**8**) [37]. Films of this polymer displayed good conductivity (0.2 S cm^{-1}), although the authors realized that reduced delocalization compared to a homothiophene system was the probable culprit of its lower charge transport rates, the energies of the valence and conduction bands being a function of the position in the polymer backbone. Polymers grown from 5,5'-bis(2-thienyl)-4,4'-dimethyl-2,2'-bithiazole (**9**) and 5,5'-bis(3-methoxy-2-thienyl)-4,4'-dimethyl-2,2'-bithiazole (**10**) were reported by Jenkins and Pickup [38], yielding maximum conductivities of $4 \times 10^{-3} \text{ S cm}^{-1}$ and $7 \times 10^{-3} \text{ S cm}^{-1}$, respectively, in the p-doped state, by dual electrode voltammetry.

Although the presence of an imine functionality in thiazole endows polythiazoles with less enviable p-doping characteristics than for polythiophenes, these materials are susceptible to n-doping, making them good candidates for applications in electrochromic devices [39], light emitting diodes (LED's) [40, 41], and lithium batteries [42]. A comparison between n-doping potentials of poly(3-methyl thiophene) and poly(3-methyl thiazole) (-2.30 V and -2.05 V, respectively, vs Ag/Ag^+) elucidates this effect [39]. It is seen that n-doping is more facile for the latter polymer.

Another attractive feature of polymers containing 2,2'-bithiazole is the possibility of coordinating transition metal ions to combine the interesting electrochemical properties of the conducting polymer backbone with the rich redox chemistry of metal complexes. Also, it has been shown that *N,N*-metal coordination occurs in these complexes (i.e., no sulfur

coordination) [43, 44]. Although the electrochemistry of a variety of conjugated metallopolymers containing 2,2'-bipyridine has been reported, only one account [37] outside our laboratory pertaining to metal complexes of polymers incorporating 2,2'-bithiazole is known.

1.5 Conjugated Metallopolymers

Hybrid materials which combine redox active sites with the conjugated π -orbital network of a conducting polymer have been known for some time [45, 46]. Recently, a new class of metallopolymer has been developed, in which the metal complex is coordinated directly to the delocalized π -orbital framework of a conducting polymer. This arrangement affords enhanced electron transport relative to redox polymers, due to d_M - π_L orbital overlap. In the past five years or so, the number of reports concerning conjugated metallopolymers and their new and interesting properties has grown substantially. One aim of the research in this group is directed at understanding the mechanisms at work during electron transport.

For the conjugated / redox polymer hybrid systems developed so far, there exist three possible mechanisms of electron (hole) transport [47] based on well known mechanisms for bimetallic systems [48]. All three may occur in a given metallopolymer to some extent. As shown in Figure 1.6, the first mechanism is the one that exists in redox polymers. Electron hopping, or self-exchange, consists of outer sphere electron transfer between fixed, adjacent metal complexes, and relies on contact between electron density surrounding these sites. In this case, no electron transport occurs through the polymer backbone. Movement in this manner is slow, driven by a concentration gradient across the

electroactive film starting with sites immediately neighboring the electrode surface.

Polymer-mediated electron transfer is a multistep process, which is possible in metallopolymers for which metal-based electrochemistry overlaps the electrochemistry of the polymer backbone. For the p-doping scenario, the backbone is oxidized by the higher valence metal center, which necessarily becomes reduced in the process. The adjacent, lower valence metal site is subsequently oxidized by the polymer backbone. Obviously, for this mechanism to occur, the oxidized metal site must be able to mediate polymer oxidation, and so the formal potentials for both processes must be similar. Electron transport through the backbone between complexed metal centers may also occur by a superexchange mechanism in which the polymer's π -orbital skeleton overlaps metal-based d-orbitals, providing a conduit for fast charge transit between metal centers.

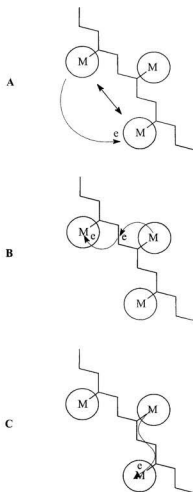


Figure 1.6: Electron transport mechanisms in conjugated metallopolymers [47]: **A**, outer sphere electron transfer (self-exchange); **B**, polymer mediated pathway; **C**, superexchange through a π -conjugation network. Reprinted with permission from *J. Mater. Chem.* **1999**, 9, 1641. Copyright 1999 Royal Society of Chemistry.

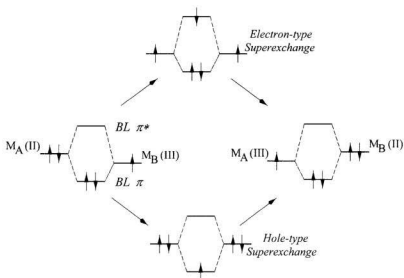


Figure 1.7: Hole and electron type superexchange. BL = bridging ligand. Reprinted with permission from *J. Mater. Chem.* **1999**, *9*, 1641. Copyright 1999 Royal Society of Chemistry.

Depending on the relative energies of the metal's d-orbitals and the backbone p-orbitals, superexchange may be of the hole or electron type. Both are represented in Figure 1.7 for a M^{III} binuclear system. From the orbital energy diagrams, it is apparent that electron superexchange involves d_M -orbital overlap with the LUMO of the polymer, while hole-type superexchange involves d-orbitals mixing with the polymer HOMO. This kind of electron transport has been demonstrated for metal complexes separated by a bridging ligand [48]. Very strong electronic communication between metal sites is manifested by a splitting of the M^{III} wave. It was expected from the outset of this research

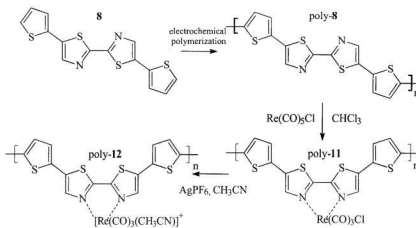
that conjugated metallopolymers containing the 2,2'-bithiazole moiety would demonstrate electronic communication *via* the superexchange-type mechanism, and that the extent of metal-metal communication could be tuned by substitution at sites on the polymerizable bithiazole ligand.

1.6 Literature on Conjugated Metallopolymers

It is only during the last decade that attempts have been made to study these redox/conjugated polymer hybrids. Early reports related to preformed polymer backbones reacted with metal salts to form incompletely and irregularly substituted products [49]. Since then, polymers having 100% coordination have been developed by the polymerization of monomer metal complexes. Several review articles dealing with conjugated metallopolymers and/or their applications have recently appeared [47, 50, 51]. What follows is a collection of interesting accounts concerning these intriguing systems.

1.6.1 2,2'-Bithiazole Based Metallopolymers

Wolf and Wrighton [37] first developed a metallopolymer containing the 2,2'-bithiazole moiety, by the anodic polymerization of 5,5'-bis(2-thienyl)-2,2'-bithiazole (**8**). Subsequent complexation with $\text{Re}(\text{CO})_3\text{Cl}$ centers (Scheme 1.1) provided a metallopolymer immobilized on a gold surface for expedient electrochemical analysis. The rationale behind the experiment was to use the electroactive backbone to modulate electron density at the metal center. Changes in the oxidation state of the polymer could be controlled by a



Scheme 1.1: Derivatization of poly-8.

potentiostat, permitting control of the electron density of the metal complex. IR stretching frequencies of the carbonyl ligands provided a convenient handle with which to gauge the effectiveness of the electron source/sink polymer film. The study implied the possibility of utilizing conjugated polymers to affect the potency of immobilized electrocatalysts.

Re centers were coordinated to films of poly-**8** by refluxing coated electrodes in $\text{Re}(\text{CO})_5\text{Cl}/\text{CHCl}_3$ solutions for 5 minutes, yielding poly-**11**. This was followed by conversion of the $\text{Re}(\text{CO})_5\text{Cl}$ groups to $[\text{Re}(\text{CO})_3(\text{CH}_3\text{CN})]^+$ (poly-**12**). XPS showed that 60-75% of the available coordination sites were occupied. Cyclic voltammetry showed that poly-**8** is p-doped at ~ 0.8 V vs Ag wire, and is stable to potential cycling to 1.4 V, while

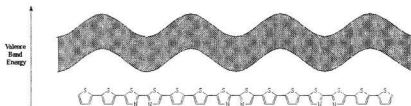


Figure 1.8: Valence band energy with position in poly-8. Adopted from [37].

the metallopolymer, poly-12, required a higher p-doping potential. No rhenium-centered wave was observed, presumably due to overlap with the backbone electrochemistry. The poly-12 film could be cycled to greater potentials. It is expected that the onset of polymer oxidation will shift to higher potentials upon coordination of a metal cation, as this will yield a less delocalized π -system.

The same intuition suggests that the film should be less stable to potential cycling and more susceptible to nucleophilic attack than the uncomplexed polymer. The authors postulated that this result may indicate that polymer deactivation occurs at the N sites of the backbone, and that metal coordination somehow blocks this process; however, the considerable degree of uncomplexed sites in the metallopolymer clouded this hypothesis. *In situ* conductivity measurements performed with microelectrode arrays showed that the onset of conductivity in the conjugated polymer is shifted to higher potentials upon metal coordination. The maximum p-type conductivity for poly-12 was determined to be $2 \times 10^{-3} \text{ S cm}^{-1}$, two orders of magnitude less than for poly-8. The decrease in conductivity

was attributed to decreased delocalization with metal cation coordination. The valence band energy, shown for the bithiophene-bithiazole backbone in Figure 1.8, was reasoned to vary with the position in the backbone. Free electrons created by doping would be found at lower energy (bithiazole segments) while holes would be localized on the higher energy bithiophene segments. The energy mismatch between bithiophene and bithiazole thus creates a barrier to charge movement, and this barrier will be more pronounced with a coordinated metal cation. The localization of charge carriers is also suggested by IR data, revealing only modest shifts (4-6 cm^{-1}) in CO stretches after polymer oxidation. Shifts of only 15 cm^{-1} in a similar polymer bearing pendant Re complexes have been shown to increase the rate of nucleophilic attack at a similar rhenium center by 200 times, so variants of this system might yet hold promise in altering the reactivity at electrocatalytic centers.

1.6.2.1 2,2'-Bipyridine-based Materials

Inaugural work by Yamamoto *et al.* on ruthenium complexes of poly(2,2'-bipyridine) (**5**), also examined a material formed by reaction of a preformed polymer with a metal complex, resulting in 10-15% occupation by $\text{Ru}^{\text{II}}(\text{bpy})_2$ groups [49]. The resulting metallopolymer displayed the poorly defined electrochemistry shown in Figure 1.9, characterized by very broad waves which extended over the entire potential window. The wave broadening in the polymer voltammogram indicated a polymeric structure with extended conjugation; however, the position of the Ru^{III} wave relative to the analogous model complex ($\text{Ru}(\text{bpy})_3$) wave, revealed that a shift to lower potentials had occurred, while bipyridine

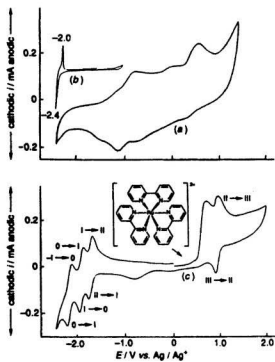


Figure 1.9: Electrochemistry of (a) Ru-5 material, (b) poly-4, (c) Ru(bpy)₃, in CH₃CN/0.1 M Et₄NClO₄.

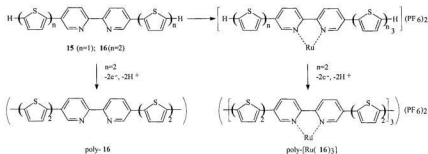
Reprinted from *J. Am. Chem. Soc.* 1994, 116, 4832. Copyright 1994 American Chemical Society.

ligand reduction waves migrated substantially positive. About the only thing which can be inferred from this data with any certainty is that the electronic structure of the backbone was affected by incorporation of the metal complex (compare reduction of **5** with that for **5-Ru(bpy)₂**). Due to poor characterization of the film studied, the results and conclusions drawn must be viewed with caution.

Polymers of 6,6'-dimethyl and 6,6'-dihexyl-2,2'-bipyridine systems (**13**, **14**) have been complexed with Cu^+ to form polymers with higher site occupancy (76-99%) which are better characterized and exhibit better-behaved electrochemistry [52]. The authors claimed these metallopolymers displayed conductivities of $\sim 1 \times 10^{-4} \text{ S cm}^{-1}$, although only the electrochemistry of the hexyl substituted polymer was discussed in detail. An oxidation process at 0.59 V vs Ag/Ag^+ was attributed to $\text{Cu}^{2+/+}$, while a more reversible process at -1.84 V was likely due to the reduction of 2,2'-bipyridine groups (although the authors assigned this wave to a reversible Cu^{+0} reduction). A decrease in peak current during potential cycling to -2.2 V was explained as Cu^0 dissociation.

1.6.2.2 Bipyridine-bithiophene Copolymers

The similarities which exist between thiophene-bithiazole copolymers and thiophene-bipyridine copolymers make the latter a useful system with which to compare results. Preliminary work on this composite was reported by Zhu and Swager [53], in which they adopted Wrighton's strategy of incorporating terminal, electropolymerizable thiophene substituents onto the ligating species in the hope of generating metallopolymers having



Scheme 1.2: Extension of bithiophene termini to yield a polymerizable Ru^{2+} complex.

100% coordination (Scheme 1.2). Strangely, neither **15** nor $\text{Ru}(\text{15})_3$ could be electropolymerized. Extending the conjugation to a six ring assembly raised the system's HOMO energy, permitting facile film growth of both poly-**16** and its tris- Ru^{2+} complex, poly- $\text{Ru}(\text{16})_3$ in CH_2Cl_2 (Figure 1.10). Poly-**16** displayed the cyclic voltammetry shown in Figure 1.10A. The oligothiophene segments of this polymer are responsible for the nondescript p-doping electrochemistry. Reduction of the polymer was seen to occur at less negative potentials than polythiophene, an influence of the electron deficient nature of bipyridine. Charge trapping peaks are evident at 0.3 V and -1.0 V vs Ag/Ag^+ , suggesting reduced delocalization (charge trapping is a phenomenon often displayed by redox polymers). The polythiophene-like p-doping properties and the similarity of the reduction potential with polybipyridine support this argument, suggesting polymer oxidation is localized on oligothiophene spacers while reduction occurs on the bipyridine sites. It is seen that n-type conductivity ($4 \times 10^{-3} \text{ S cm}^{-1}$) is twice as great as for p-type peak

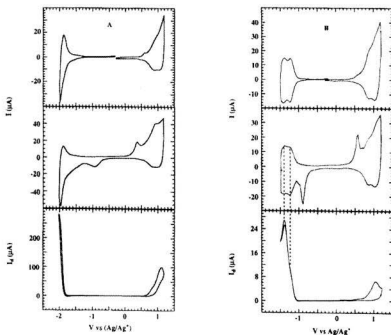
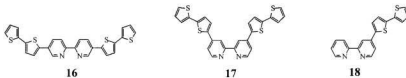


Figure 1.10: Cyclic voltammetry and conductivity profiles (i_{α} \propto conductivity) of: A) poly-**16**; B) poly-Ru(**16**)₃.

Reprinted with permission from *Adv. Mater.* **1996**, 8, 497. Copyright 1996 WILEY-VCH Verlag GmbH.

conductivity ($2 \times 10^{-3} \text{ S cm}^{-1}$) in $\text{CH}_3\text{CN}/\text{Bu}_4\text{NPF}_6$. These results point to a polymer with reduced delocalization, the bipyridine segments representing barriers to hole movement along the π -conjugated backbone.

The cyclic voltammetry of poly-Ru(**16**)₃ is shown in Figure 1.10B. Obvious similarities exist in the anodic regions for this metallopolymer and poly-**16**. Unfortunately,



it appears that the potential required to observe the $\text{Ru}^{3+/2+}$ wave is too high, and no mention is made of whether this process was seen. The cathodic electrochemistry is quite different, however, showing two well-defined, reversible waves at -1.23 V and -1.39 V, attributable to reductions localized on the 2,2'-bipyridine ligands. The charge-trapping peaks have increased in magnitude, possibly due to poorer energy matching between thiophene and bipyridine units upon coordination of the cationic metal center. The conductivity profile of poly-Ru(16), shows that n-type charge transport is much higher than for p-type. It appears from the data that overoxidation (probably due to nucleophilic attack in CH_3CN) at the potentials chosen resulted in film degradation, effectively deactivating the polymer backbone. The n-type conductivity was determined to be at a maximum at -1.37 V ($9.4 \times 10^{-4} \text{ S cm}^{-1}$). The appearance of the conductivity profile again indicates redox behavior, the shoulder and peak potentials being coincident with the formal reduction potentials in Figure 10B. This behavior is reminiscent of that displayed by non-conjugated poly-[Os(bpy)₂(4-vpy)₂] (4-vpy = 4-vinylpyridine) [54], suggesting that the n-type charge carriers generated by reduction of poly-Ru(16), are localized on the bipyridine segments of the backbone.

In order to assess the effect of thiophene substitution on through-metal conjugation, Swager and Zhu prepared *tris*-ruthenium and bis(2,2'-bipyridine)ruthenium(II) complexes

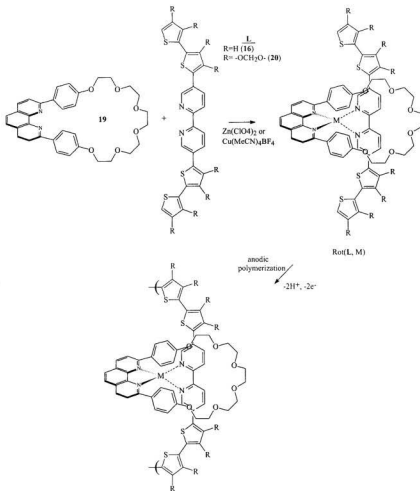
of **16**, **17** and **18** [55]. For Ru(**16**)₃, a meta relationship exists between the bithienyl end groups and the ruthenium center, while for the less delocalized Ru(**17**)₃, the relationship is para, across the pyridine ring. Reduction of the homoleptic complexes in CH₂Cl₂/Bu₄NPF₆ revealed one redox wave, while two processes were observed for each heteroleptic complex. Conversely, for the corresponding metallopolymers, one reduction wave was observed for heteroleptic structures, while poly-Ru(**L**)₃ type chains yielded only one reduction in the potential window investigated. The maximum conductivity of poly-Ru(**16**)₃ was determined again, this time in a less nucleophilic solvent; a value of 1.2x10⁻³ S cm⁻¹ was obtained. The ligand **17** lacks the extended conjugation that is present in **16**. Poly-**17**, therefore, should exhibit a much lower conductivity than poly-**16**. In fact, it was found that the conductivity of poly-**17** was too low to determine (i.e., below 10⁻⁶ - 10⁻⁷ S cm⁻¹). The conductivity of the metallopolymer, poly-Ru(**17**)₃, however, was estimated to be 3.3x10⁻³ S cm⁻¹, indicating that self-exchange between localized redox centers is enhanced by the para-substitution relationship between ruthenium and bithiophene units. Since poly-**17** does not show appreciable conductivity, the results indicate that the ruthenium center is incorporated in the conjugation path. Poly-Ru(**18**)₃ contains a ligand which can undergo oxidative polymerization at one end only, and so metallopolymers of this complex must form a conjugated bridge through ruthenium. The metallopolymer's conductivity (1.73x10⁻³ S cm⁻¹) is intermediate to the values obtained for the other systems, suggesting that the greater number of linkages in poly-Ru(**17**)₃ facilitates electron exchange between adjacent ruthenium sites. Metallopolymers formed from bis(bipyridine)ruthenium salts were not found to be as conductive, since no cross-linking is

possible for these complexes and electron hopping along the chain must be one-dimensional. Not surprisingly, the conductivity of poly-Ru(**16**)(bpy)₂ was found to be higher than for the non-conjugated analog, poly-Ru(**17**)(bpy)₂.

An intelligent strategy for the development of a discriminating metal ion sensor employing thiophene-pyridine copolymers was also presented by Swager's group [56]. The macrocyclic phenanthroline **19** was employed in conjunction with the polymers **16** and **20** to complex Zn²⁺ and Cu⁺ in forming metallorotaxanes, which could be electropolymerized and the metal center subsequently removed (Scheme 1.3). Since films of the demetallated polymer/macrocycle could coordinate metal cations from Zn²⁺ or Cu⁺ solutions, sensory applications have been envisaged.

Substitution of 3,4-ethylenedioxythiophene (EDOT) substituents for thiophenes appears to result in a less delocalized π -network, the EDOT ligands being more electron rich (and thus a poorer energy match for bipyridine) [57]. Cyclic voltammetry indicates two oxidation processes (Figure 1.11A), apparently resulting from polaron and then bipolaron formation. These results contrast with the broad charge envelope of poly-**16**. The maximum conductivity for poly-**20** coincided with the second redox peak, and was estimated to be $3.5 \times 10^{-2} \text{ S cm}^{-1}$. The conductivity peaks and their dependence on the peak potentials for ethylenedioxythiophene oxidation imply that this polymer behaves as a localized redox conductor.

Introduction of either Zn²⁺ or Cu⁺ into the polyrotaxane structure causes a drop in conductivity, the cationic centers enhancing the localization of the backbone's electronic



Scheme 1.3: Complexation of **19** and either **16** or **20** with M (Zn^{2+} or Cu^+) to yield polymerizable metallorotaxane complexes.

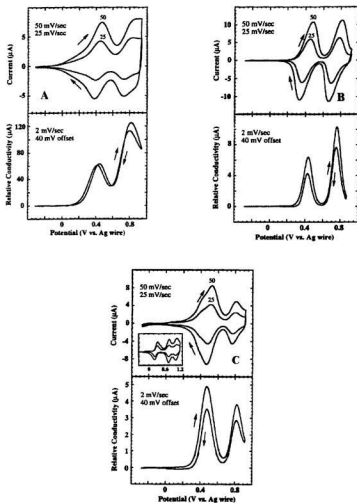


Figure 1.11: Cyclic voltammetry of and conductivity of A: poly-20; B: poly-Rot(20,Zn); C: poly-Rot(20,Cu).

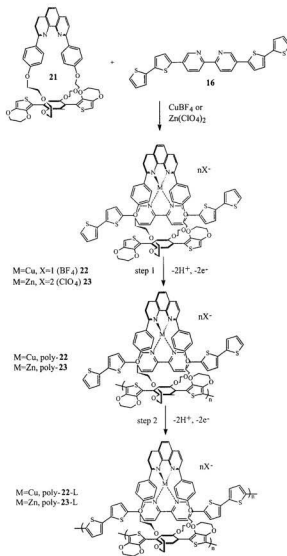
Inset: poly-Rot(16,Cu). Reprinted with permission from *J. Am. Chem. Soc.* 1997, 119, 12568. Copyright

1997, American Chemical Society.

wave functions. This effect is manifested in a sharpening of the redox peaks for poly-**20**. For poly-Rot(**20**,Cu), the $\text{Cu}^{2+/1+}$ process overlaps the p-doping wave of the backbone (Figure 1.11C), while for poly-Rot(**20**,Zn), metal oxidation occurs well below the polymer's oxidation potential (Figure 1.11B). The consequence is a higher conductivity associated with the first oxidation process in poly-Rot(**20**,Cu), as Cu^{2+} is able to mediate electron transport between oxidized tetra(ethylenedioxythiophene) segments. A demetallated, undoped film of poly-Rot(**20**) exposed to a Cu^{2+} solution resulted in a 10^6 - 10^7 -fold increase in the material's conductivity, while the same experiment performed with a Zn^{2+} solution only resulted in a tenfold increase, thereby providing an example of a conjugated polymer-based sensory material displaying ionic recognition.

A new polymer derivative of **19** was recently described in which the polyrotaxane structure **21** served as an internal pipe between two outer poly-**16** chains [58]. A two-step polymerization (Scheme 1.4) leads to a three-strand "ladder polymer" in which the polyrotaxane chain can effectively act as a molecular wire when the outer poly-**16** chains are kept at insulating potentials.

Polymerization of the macrocyclic phenanthroline metal complex in the presence of **16** by cycling between -0.5 V and +0.55 V resulted in polymer film deposition. Since cyclic voltammetry of poly-**21** and poly-**22** exhibited a similar response, it appears that polymerization occurs at the 3,4-ethylenedioxythiophene substituents and not at the bithiophene sites. Subsequent polymerization at higher potentials enables polymerization of the bis(bithienyl)bipyridine ligand, yielding the highly interconnected supramolecular

Scheme 1.4: Two-step ladder polymer formation from **22** or **23**.

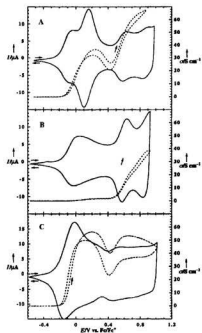


Figure 1.12: Cyclic voltammetry (—) and conductivity (---) of ladder-type polymers: poly-22-L (A); poly-23-L (B); poly-21 (C). Reprinted with permission from *Angew. Chem. Int. Ed.* **2000**, 39, 608. Copyright 2000, WILEY-VCH Verlag GmbH.

constructs poly-22-L and poly-23-L. In this step, the macrocyclic phenanthroline is effective in preventing close contact between adjacent polymer chains, lowering their tendency to undergo cross-linking reactions.

Figure 1.12 compares the electrochemistry of poly-22-L, poly-23-L, and poly-21. It can be seen by comparison that the waves at ca. 0.1 V vs Fc/Fc⁺ in A and B can be ascribed

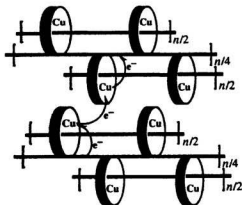


Figure 1.13: Interchain electron-hopping mechanism existing in poly-23-L [57]. Reprinted with permission from *Angew. Chem. Int. Ed.* **2000**, 39, 608. Copyright 2000, WILEY-VCH Verlag GmbH.

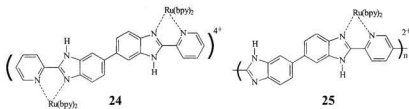
to oxidation of the macrocycle-containing polymer. The waves at ~ 0.6 V and ~ 0.85 V involve oxidation of both poly-**21** and poly-**16**, although since the polyrotaxane complexes have such low conductivities in comparison to these materials, these waves are attributed primarily to p-doping of the poly-**21** backbone. A comparison of *in situ* conductivity measurements shows that at low potentials, only the poly-**21** backbone demonstrates electron transport, with the copper derivative displaying redox-mediated behavior. The redox-inactive zinc form displays a twenty-fold lower value than for the copper macrocycle-polymer complex, validating the metal-polymer mediation theory. At higher (~ 0.9 V) potentials, poly-**22-L**, poly-**23-L** and poly-**21** all show comparable conductivities,

as the threading element, poly-**16**, becomes electroactive and can participate in interchain electron-hopping events (Figure 1.13).

1.6.3 Benzimidazole-based Materials

Polybenzimidazoles offer several advantages as backbones for conjugated metallopolymers. Their facile synthesis, structural rigidity, and robust nature [59] provide a sound foundation for experiments with these materials. The imidazole sites of this polymer possess an acidic proton, which may be removed and replaced, allowing control over the electron density of the backbone. This fact has been exploited by Cameron and Pickup [60-63] to provide strong evidence for the existence of a superexchange pathway in these systems.

The dinuclear ruthenium model complex **24** has been reported to oxidize in two steps [64], the peak separation being pH dependant. For the protonated ligand, the peak separation was estimated to be about 45 mV. Deprotonation of the benzimidazole ligand increases this separation to ~ 80 mV, indicating that increased electron density accumulated at the higher pH serves to stabilize the HOMO energy and improve metal-metal communication.



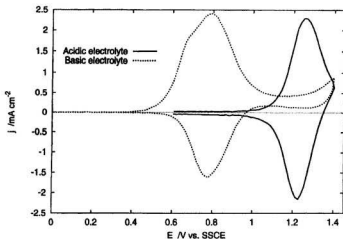
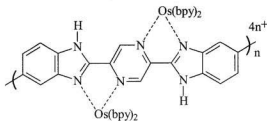


Figure 1.14: Cyclic voltammetry of a thin film of **25** ($\nu=100 \text{ mV s}^{-1}$) in $\text{CH}_3\text{CN}/0.1\text{M Et}_4\text{NClO}_4$ containing *ca.* 50 mM HClO_4 (solid line) or *ca.* 5 mM Bu_4NOH (dashed line). Reprinted with permission from *J. Am. Chem. Soc.* **1999**, 121, 11773. Copyright 1999, American Chemical Society.

Electron transport in the poly[2-(2-pyridyl)bibenzimidazole] metallopolymer **25** [60, 61] was investigated by dual electrode voltammetry, rotating disc voltammetry, and impedance spectroscopy, the last technique providing the greatest precision. D_e , the electron diffusion coefficient, was estimated to be $6 \times 10^{-9} \text{ cm}^2 \text{ s}^{-1}$ in acidic media, and $1.0 \times 10^{-8} \text{ cm}^2 \text{ s}^{-1}$ in basic conditions, reflecting the behavior of the dinuclear model complex. The voltammogram shown in Figure 1.14 illustrates the dependence of the position of the $\text{Ru}^{3+/2+}$ wave on solvent pH. By removal of the imidazole proton, the electron density at

the metal center is affected, increasing the potential required for Ru^{2+} oxidation at low pH and decreasing it at high values. Deactivation of the organic component by exposure to elevated potentials was shown to lower D_e , implicating an intimate role of the backbone in metal-metal communication. Since p-doping of the complexed polymer does not occur at the potentials chosen, the rate of electron transport is governed by electron hopping between metal sites. D_e values for a similar polymer in which insulation by a saturated linkage exists, $\text{poly}[\text{Ru}(\text{bpy})_2(4\text{-vpy})_2]^{3+/2+}$, are an order of magnitude lower ($7 \times 10^{10} \text{ cm}^2 \text{ s}^{-1}$), thus metal-metal communication must be enhanced by the conjugated backbone. UV-Vis-NIR experiments showing the appearance of an intervalence transfer (IT) band further support this argument.

Strong electronic communication between adjacent Os^{III} centers across a pyrazine bridge was demonstrated for the more rigid system **26** [62]. The existence of highly conductive states corresponding to 75:25 and 25:75 $\text{Os}^{3+}:\text{Os}^{2+}$ states was demonstrated by dual electrode voltammetry. Interestingly, poor conductivity was found in the 50:50 state, the condition which normally optimizes self-exchange. Two well separated (ΔE ca.



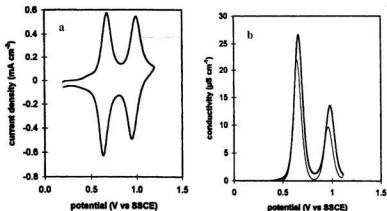
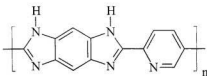


Figure 1.15: a) Cyclic voltammety of 26:90:2:1 CH₂Cl₂/CH₃CN containing 0.1 M Et₄NClO₄ + ca. 0.05M HClO₄; b) Conductivity vs potential. Thinner line represents reverse scan. Reprinted with permission from *J. Am. Chem. Soc.* 1999, 121, 7710. Copyright 1999, American Chemical Society.

320 mV) conductivity peaks correspond to the cyclic voltammety shown (Figures 1.15a and b). This large separation corresponds to the energy required to produce Os³⁺-Os³⁺ sites by oxidation of Os³⁺-Os²⁺. The higher conductivity associated with the first Os^{3+/2+} can be explained by a difference in the orbital overlap of Os centers with the conjugated backbone before and after oxidation. This suggests that higher energy electrons move faster through the conjugation network, pointing to an electron-type superexchange pathway. D_c values for this system at each wave were determined to be $\sim 1.3 \times 10^{-8} \text{ cm}^2 \text{ s}^{-1}$ and $7.0 \times 10^{-9} \text{ cm}^2 \text{ s}^{-1}$. D_c for the non-conjugated poly-[Os(bpy)₂(4-vpy)₂]^{3+/2+} was found to be $\sim 8 \times 10^{-9} \text{ cm}^2 \text{ s}^{-1}$ [65]. The low conductivity associated with the 50:50 Os^{3+/2+} population and the structural

rigidity of this metallopolymer suggest that an outer sphere mechanism is not the major contributor to electron transport, suggesting superexchange through the conjugated backbone. A higher D_e relative to the non-conjugated model clearly shows that the conjugated backbone enhances electron transport.

By varying the pH, and thereby modulating the electron density in the backbone, evidence for superexchange pathways were demonstrated for ruthenium and osmium complexes of several polybenzimidazoles [63]. Through comparison of D_e data, and by comparison against non-conjugated ruthenium and osmium polymers, it was shown that charge transport in these systems could be more readily explained assuming a superexchange pathway than for either a self-exchange or polymer-mediated mechanism. Ru(bpy)₂ and Os(bpy)₂ coordinated to the organic backbones of **25**, **26**, and **27** have been examined, yielding electron transport data of a magnitude similar to, or greater than, for poly-[Ru(bpy)₂(vpy)₂]^{3+/2+} [65], poly-[Os(bpy)₂(vpy)₂]^{3+/2+} [65], and poly-[Ru(bpy)₂(3-pyrrol-1-ylmethyl)pyridine]₂^{3+/2+} [66]. The benzimidazole polymers should be considerably less free to rotate, thus diminishing the likelihood of outer sphere exchange. The lack of overlapping backbone electrochemistry and a potential independent D_e both suggest that a polymer-mediated mechanism is not at work. Furthermore, the transport data are more similar between ruthenium and osmium complexes of the protonated benzimidazole polymers than in the redox metallopolymer. For a self-exchange mechanism, the bulkier Os has been shown to exhibit a larger D_e . Deprotonation augments D_e for the ruthenium complex of **25**, while it decreases D_e for the osmium analog. These changes are not readily explained for outer-sphere behavior, but do conform to arguments



27

based on relative HOMO and LUMO energies, considering the backbone's electron density as a function of pH. This lends support to the existence of a superexchange mechanism in these metallopolymer.

1.6.4 Other Conjugated Metallopolymer

A recent review concerning sensory applications of conjugated polymers has examined a wide variety of redox/conjugated polymer hybrids [51]. Crown ether functionalization of polythiophene systems (**28**, **29**) to produce conjugated polymers having covalently bound sensing elements has been reported [67,68]. Increasing the amount of alkali metal ions elicited a decreased current response and shifted film oxidation towards higher potentials in cyclic voltammetry experiments for electrodes coated with these polymer films. Plots of current vs. metal ion concentration for Li^+ , Na^+ , and K^+ resulted in linear relationships (Figure 1.16). The highest sensitivity was demonstrated for Li^+ , reflective of the higher binding constant of the 12-crown-4 moiety for this ion. Poly-**29** was found to give a poorer response than poly-**28**. The authors rationalized that the ether rings create a positively charged "shell" upon metal ion complexation, presenting a barrier to charge-compensating

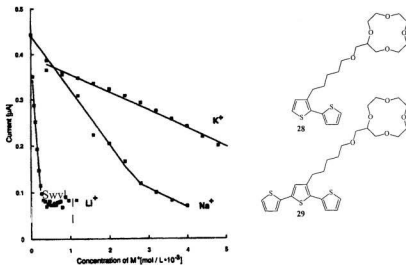
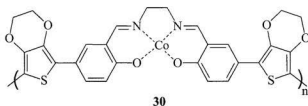


Figure 1.16: Current vs alkali metal concentration at fixed potential for electrodes covered with poly-28 in the presence of Li^+ , Na^+ , and K^+ . Reprinted with permission from *Adv. Mater.* **1993**, *5*, 848. Copyright

1993, WILEY-VCH Verlag GmbH.

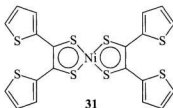
anions during redox cycling. Since poly-29 would have a lower number of ether rings, a less dense shell is created, lowering the restriction of counterion movement and resulting in higher currents (less sensitivity).

The Schiff base system **30** demonstrates an example of a conjugated metallopolymer in which the metal center forms an integral part of the transduction pathway [69]. The uncomplexed monomer clearly lacks conjugation at the ethylene bridge, electronically isolating the molecule into two equivalent halves. Although the



metal-free ligand is unable to be polymerized, complexation with Co allows polymerization to proceed readily. Exposure to Lewis bases like bipyridine significantly and irreversibly decreased the conductivity of thin films on interdigitated microelectrodes. The formation of five- and six-coordinate poly-**30**-bipyridine complexes was proposed as an explanation. The electroactivity of the metallopolymer, however, was unchanged due to overlapping of the backbone electrochemistry with that of the metal center.

Metal dithiolene salts have been shown to exhibit superconductivity. Redox-conjugated polymer blends containing these complexes were synthesized recently [70] to take advantage of this and other amiable properties offered by dithiolenes. Metal dithiolene-based electrochemistry was reported for both the monomer and polymer (i.e., redox processes delocalized over the Ni-dithiolene unit), as well as a process involving terminal thiophene oxidation. Polymerization of the planar molecule **31** produced a low bandgap (*ca.* 0.8 V) material having a conductivity of *ca.* 10^6 S cm^{-1} in a mixed valence state and *ca.* 10^4 S cm^{-1} when the polymer backbone was p-doped. The lower than expected conductivities were attributed to crosslinking, the four polymerizable thiophene moieties offering many possible pathways for non-linear electron movement.



1.7 Goals

The major aim of this research was directed at developing polymer materials possessing 2,2'-bithiazole coordination sites in which the extended conjugation afforded by the organic backbone could facilitate electronic communication between complexed, redox-active metal centers (Figure 1.17). A superexchange mechanism of electronic movement should exist for these systems, and electron transport experiments in which the electron diffusion coefficient, D_e , is obtained should provide evidence of this. It was also anticipated that polymers containing 2,2'-bithiazole would demonstrate better stability to p-doping than related 2,2'-bipyridine based polymers, and good n-doping characteristics.

A long-term aim of this project is the development of electrocatalysts. It is foreseeable that materials exhibiting enhanced rates of electron transfer will occupy an important niche in this area. Electrode coatings comprised of conjugated metallopolymer coatings provide a novel approach to the catalysis of electrochemical reactions. In this case, the polymer backbone acts as a support for the electrocatalyst sites. This arrangement (Figure 1.18) can provide several important advantages:

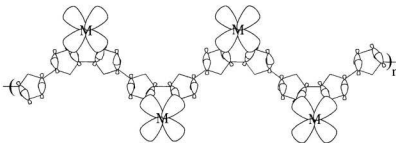


Figure 1.17: Metal centers coordinated to bidentate sites of a polyconjugated backbone.

- 1 A high effective concentration of electrocatalytic centers at the site of the reaction (i.e., the electrode surface), permitting interaction with multiple catalyst centers
- 2 Facile removal of the catalyst from the reaction flask
- 3 Facilitated (faster) regeneration of the catalyst through the conjugated π -system (relative to non-conjugated metallopolymers)
- 4 Some control over the rate of catalysis is obtained, by control of the current passed during the reaction

Ruthenium and osmium centers were chosen to form metal complexes with the polymerizable bithiazole monomers. $\text{Ru}(\text{bpy})_2^{2+}$ and $\text{Os}(\text{bpy})_2^{2+}$ complexes of bithiazole ligands exhibit well-behaved, reversible electrochemistry. Furthermore, ruthenium electrochemistry is well documented, particularly for electroactive polymers, enabling a wide library of comparison.

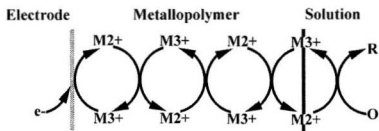


Figure 1.18: Electrocatalysis of the reaction $O + e^- \rightarrow R$ by a metallopolymer coating.

Chapter 2

Syntheses of Monomers, Polymers, and Transition

Metal Complexes

2.1 Chemicals and Instrumentation

All chemicals were used as received unless stated otherwise.

Nuclear magnetic resonance (NMR) spectra were acquired on a Bruker ASPECT 100 MHz NMR, a GE-300NB instrument at 300 MHz or a Bruker Avance 500 equipped with an inverse detect gradient probe at 500 MHz. Chemical shifts are reported against TMS ($(\text{CH}_3)_4\text{Si}$) as an internal standard. For all spectra, peaks are reported as chemical shift, σ (ppm), multiplicity (s = singlet, d = doublet, dd = double doublet, t = triplet, m = multiplet), and relative integration ratio. Data processing was accomplished with the NUTS software package (Acorn). Spectra for other compounds included in this thesis are located at the end of Appendix B.

Mass spectra were obtained with a V.G. Micromass 7070HS spectrometer or a Hewlett Packard Series 1100 Electrospray Mass Spectrometer equipped with an electrospray ionization source, a quadrupole mass analyzer (m/z range of 3000) and a HED electron multiplier. Atmospheric pressure ionization electrospray mass spectra (API-MS) analyses were performed in HPLC grade methanol (Aldrich). Fragments are reported as m/z (base peak and molecular peak, where possible) at a fragmentation voltage of 100 V.

Elemental analyses were performed by Canadian Microanalytical Services, 207-8116 Alexander Road, RR #7, Delta, BC, V4G 1G7.

The X-Ray crystal structure determination for $\text{Ru}(\text{btbmtz})(\text{bpy})_2(\text{PF}_6)_2$ was performed by Dr. Bob MacDonald, University of Alberta. Data workup was performed by David O. Miller, Memorial University of Newfoundland.

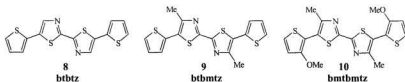
Electrochemical experiments were performed with a Pine Instruments RDE-4 potentiostat interfaced with a PC equipped with an analogue-digital digital-analogue converter computer board (Data Translations DT2801 analogue to digital converter card). Software for data translation was authored by Dr. Colin G. Cameron. Electrochemical impedance experiments were recorded with a Solartron Schlumberger 1268 electrochemical interface and 1250 frequency response analyzer equipped with custom software. Electrochemical potentials are reported vs SSCE unless otherwise noted.

10 (bmtbmtz) was synthesized by Dr. Ieuan Jenkins. $\text{Ru}(\text{bmtbmtz})(\text{bpy})_2(\text{ClO}_4)_2$ and $\text{Ru}(\text{bmtz})(\text{bpy})_2(\text{ClO}_4)_2$ were synthesized by Dr. Peter Pickup. $\text{Os}(\text{bpy})_3(\text{PF}_6)_2$ was synthesized by E. Bradley Easton. Reported yields are not optimized.

2.2 Synthesis

2.2.1 Strategies to Electropolymerizable Ligands

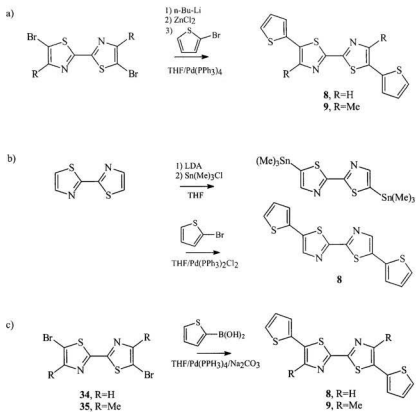
Since 2,2'-bithiazole cannot be polymerized electrochemically, terminal thiophene substituents were employed to provide easily oxidizable sites at which radical coupling could occur. The series of ligands investigated (**8 (btbtz, 5,5'-bis-(2-thienyl)-2,2'-bithiazole)**, **9 (btbmtz, 5,5'-bis-(2-thienyl)-4,4'-dimethyl-2,2'-bithiazole)**, **10 (bmtbmtz, 5,5'-bis-(3-methoxy-2-thienyl)-4,4'-dimethyl-2,2'-bithiazole)**) differ in the number of electron donating functionalities attached to a basic 4-ring skeleton. Methyl substituents in **9** act to raise the energy of the valence band (inductive effect), facilitating oxidation. They are also effective in blocking polymerization at the 4-positions of the thiazole rings. The



methoxy groups of **10** affect the energies of both the HOMO and LUMO bands. The electronegative oxygen makes the substituent electron-deficient, resulting in a lowering of the LUMO energy (inductive effect). Because of the non-bonding electron pairs of oxygen, resonance stabilization also occurs. This is manifested in an increase in HOMO energy.

Ligands containing the 2,2'-bithiazole moiety were synthesized for this thesis by three routes. Jenkins and Pickup [38] obtained ligands **9** (**btbmtz**) and **10** (**bmtbmtz**) via a Negishi coupling of an aryl zinc chloride intermediate with two equivalents of the appropriate bromothiophene (Scheme 2.1a). This route was also used to synthesize **8** (**btbtz**) in low yield. A Stille coupling reported by Wolf and Wrighton [37] was initially followed for the synthesis of **8**, giving a bright yellow product in 18% yield for the final reaction step (Scheme 2.1b). Subsequent to this, another palladium-catalyzed route (Scheme 2.1c) employing 2-thienyl boronic acid and 5,5'-dibromo-2,2'-bithiazole was used to produce a better overall yield from 2,2'-bithiazole (38 %).

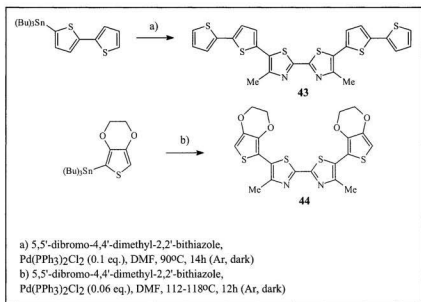
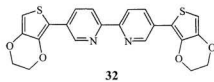
Attempts were also made at synthesizing two other bithiazole monomers, **43** (5,5'-bis(2,2'-bithienyl)-4,4'-dimethyl-2,2'-bithiazole) and **44** (5,5'-bis(3,4-ethylenedioxythiophene)-4,4'-dimethyl-2,2'-bithiazole), to take advantage of the lower oxidation potentials of 2,2'-bithiophene and 3,4-ethylenedioxythiophene termini relative



Scheme 2.1: Synthetic routes to 4-ring bis(thienyl)bithiazole ligands.

to thiophene end groups employed in **8-10**. This strategy had been exploited by Swager, *et al.* to electrogenerate metallopolymer films containing a tris(2,2'-bipyridine) core [53, 56]. They prepared ligands **16** and **20** via an organotin route in good yields (Section 1.6.2.2). **20** was synthesized only after it was found that the $\text{Ru}^{\text{II}}(\text{bpy})_3$ complex of the less extensive **32** was not able to be electropolymerized. This same strategy was used in attempts to synthesize **43** and **44**, and while the ^1H NMR spectrum for each product appears promising, exhibiting the expected peak splitting patterns (in addition to other, aliphatic hydrogen peaks presumably indicating impurities) efforts to purify these monomers have been frustrating, due to their very low solubilities in most solvents. Enough of these solids could be dissolved in CD_2Cl_2 and CDCl_3 to acquire ^1H NMR spectra (see Appendix B), but not for ^{13}C NMR data.

The attempted preparation of **43** was carried out in a manner analogous to the monomer **16** (section 1.6.2.2), by a Stille coupling in anhydrous DMF (Scheme 2.2). The purification of **16** on a similar scale was accomplished by column chromatography, although the authors recommended recrystallization for larger scale preparations [53]. Surely, the low solubility of **16** must have presented like problems to the original authors in the purification stage. The ^1H NMR spectrum for this compound elicited the expected splitting pattern, with a small impurity signal present at 7.08 ppm (Figure 2.1).

Scheme 2.2: Organotin route to 2,2'-bithiazole monomers **43** and **44**.

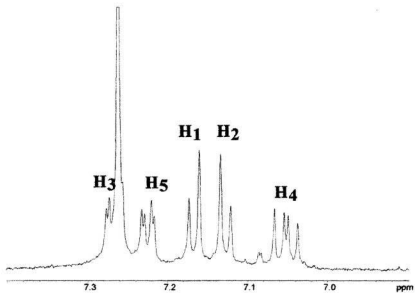
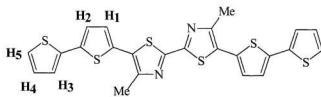
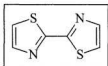


Figure 2.1: Aromatic region of the ¹H NMR spectrum for 43.

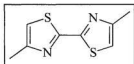
2.2.2 Starting Materials

2.2.2.1 2,2'-Bithiazole, 6 (btz) [71]



A procedure based on one outlined by Quiroga, *et al.* [71] was followed. Dithioamide (2.00 g, 16.6 mmol, 1 eq.) was stirred in anhydrous ethanol (10 mL). To this was added aminoacetaldehyde diethylacetal (4.58 g, 34.3 mmol, 2.1 eq.). The mixture was covered and stirred for 16 h. The reaction mixture was then filtered and concentrated *in vacuo* to yield a dark orange syrup. This was dissolved in H₂SO₄ (42 mL) and transferred into an ice cold P₂O₅/H₂SO₄ (5.00 g, 35.2 mmol, 2.1 eq in 5 mL) mixture under a flow of nitrogen. The mixture was then heated to 120°C for 20 min, after which time the flask was cooled to room temperature. It was then poured onto crushed ice (500 g) and neutralized with NH₄OH. Distillation yielded 2.80 g of a white crystalline product, which was recrystallized from heavy petroleum ether (BP 80°C) to yield long, white needles (1.50 g, 54%). MP 100-101°C (Lit [71]: 101°C). ¹H NMR (300 MHz, CDCl₃) δ (ppm): 7.91 (d, *J*=3.2 Hz, 1H), 7.45 (d, *J*=3.2 Hz, 1H).

2.2.2.2 4,4'-Dimethyl-2,2'-bithiazole, 33 (bmtz), [38]

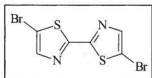


Dithiooxamide (5.00 g, 41.6 mmol, 1 eq.) was stirred in anhydrous ethanol (50 mL).

Chloroacetone (8.26 g, 87.4 mmol, 2.1 eq) was then added and the mixture was refluxed under nitrogen for 3 d. The mixture was then cooled in an ice bath and filtered, yielding black needles, which were purified by recrystallization (petroleum ether/ CHCl_3).

Additional product was recovered from the mother liquor by recrystallization from petroleum ether/ CHCl_3 . The beige/brown needles were air dried (4.59 g, 56%). $^1\text{H NMR}$ (300 MHz, CDCl_3) δ (ppm): 6.97 (s, 1H), 2.50 (s, 3H).

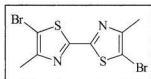
2.2.2.3 5,5'-Dibromo-2,2'-bithiazole, 34



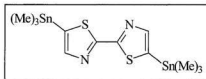
Br_2 in CHCl_3 (1.2 mL/10 mL) was slowly added to a stirred mixture of 2,2'-bithiazole (1.68 g) in CHCl_3 (200 mL). The mixture was refluxed under N_2 (24 h) in the absence of

light, followed by washing with dilute $\text{NaHSO}_3(\text{aq})$ and then H_2O . The organic layer was then dried (MgSO_4) and a pale yellow solid was obtained following removal of the solvent. This product was crystallized from heavy petroleum ether to yield cream-colored needles (1.47 g, 45%). MP 135-136°C. $^1\text{H NMR}$ (500 MHz, CDCl_3) δ (ppm): 7.75 (s). $^{13}\text{C NMR}$ (125 MHz, CDCl_3) δ (ppm): 161.9; 145.1; 112.1. Elemental analysis: Calc'd for $\text{C}_6\text{H}_2\text{Br}_2\text{N}_2\text{S}_2$: C 22.10%, H 0.62%, N 8.59%. Found: C 22.34%, H 0.62%, N 8.58%.

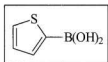
2.2.2.4 5,5'-Dibromo-4,4'-dimethyl-2,2'-bithiazole, 35 [38]



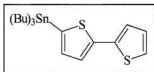
Br_2 in CHCl_3 (7.0 mL in 10 mL CHCl_3) was slowly added to a stirred mixture of 4,4'-dimethyl-2,2'-bithiazole (4.52 g, 23.0 mmol) in CHCl_3 (500 mL). The mixture was refluxed under N_2 (24 h) in the absence of light, followed by washing with dilute $\text{NaHSO}_3(\text{aq})$ and then H_2O . The organic layer was then dried (MgSO_4) and a pale yellow solid was obtained following solvent removal. This was crystallized from heavy petroleum ether to yield the product as cream-colored needles (7.46 g, 92%). $^1\text{H NMR}$ (300 MHz, CDCl_3) δ (ppm): 2.44 (s).

2.2.2.5 5,5'-Bis(trimethylstannyl)-2,2'-bithiazole, 36 [37]

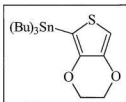
n-Butyllithium (2.5M in hexanes, 7.5 mL, 19 mmol, 2.1 eq.) was added dropwise at -78°C to a solution of diisopropylamine (2.6 mL, 19 mmol, 2.1 eq.) in THF (20 mL) under N_2 . The mixture was stirred for 30 min and then allowed to warm to room temperature for 5 min. After cooling to -78°C , a THF solution of 2,2'-bithiazole (1.49 g, 8.9 mmol, 1 eq. in 20 mL) was slowly added. The reaction mixture was allowed to stir for 1 h, and then trimethyltin chloride (1M in hexanes, 19 mL, 19 mmol, 2.1 eq.) was added, producing a pale yellow suspension. It was then stirred overnight, allowing the mixture to warm to room temperature. After this time, the mixture had taken on a clear, pale yellow appearance. Saturated $\text{NaHCO}_3(\text{aq})$ (100 mL) was then added, and the product was extracted in ether (3 x 90 mL) and dried over MgSO_4 . Gravity filtration yielded a colorless solution, which was concentrated to a white powder (2.69 g, 61%). $^1\text{H NMR}$ (100 MHz, CDCl_3) δ (ppm): 7.77 (s, 1H), 0.40 (s, 9H). m/z : 494 (M^+).

2.2.2.6 2-Thiophene boronic acid, 37 [72]

A general procedure for the preparation of arylboronic acids was followed [72]: 2-bromothiophene (2.40 g, 14.7 mmol, 1 eq.) was deoxygenated (freeze/pump/thaw x3) and dissolved in 10 mL of dry THF. After cooling to -78°C , n-butyllithium (2.36 M in hexanes, 6.4 mL, 15 mmol, 1 eq.) was added dropwise over 15 min. Stirring was continued for 15 min, after which time trimethylborate (4.64 g, 44.7 mmol, 3.04 eq.) was added. The solution was allowed to stir with gradual warming to room temperature over 18 h, yielding a foamy, white mixture. It was then cooled to 0°C , acidified to $\sim\text{pH} = 6$, and extracted into dichloromethane. Brine was added to expedite the extraction. The extract was dried over MgSO_4 . Removal of the solvent yielded 1.56 g of off-white crystals (83%) which were not pure, as indicated by $^1\text{H NMR}$. $^1\text{H NMR}$ (300 MHz, CDCl_3) δ (ppm): 8.04 (d, 1H), 7.81 (d, 1H), 7.31 (dd, 1H).

2.2.2.7 5-Tributylstannyl-2,2'-bithiophene, 38 [53]

A THF solution of 2,2'-bithiophene (0.50 g, 3 mmol, 1 eq. in 15 mL of THF) was deoxygenated (freeze/pump/thaw x3) and stirred at -78°C in a nitrogen atmosphere. *n*-Butyllithium (2.5 M in hexanes, 1.2 mL, 3.0 mmol, 1.0 eq.) was added dropwise over 15 min, yielding a pale yellow solution. The mixture was allowed to stir at -78°C for 30 min. Tributylstannyl chloride (1.00 g, 3.07 mmol, 1 eq.) was then added, and the mixture was allowed warm to room temperature with overnight stirring. After evaporation of the solvent, the residue was dissolved in hexanes and filtered. Workup yielded 1.39 g of a dark yellow liquid, which was used without further purification. ^1H NMR (300 MHz, CDCl_3) δ (ppm): 7.29 (d, 1H), 7.18 (m, 2H), 7.06 (d, 1H), 7.00 (dd, 1H), 1.57 (m, 6H), 1.35 (m, 6H), 1.11 (t, 6H), 0.90 (t, 9H).

2.2.2.8 2-Tributylstannyl-3,4-(ethylenedioxy)thiophene, 39 [56]

3,4-Ethylenedioxythiophene (2.02 g, 14.2 mmol, 1 eq.) was deoxygenated (freeze/pump/thaw) and dissolved in THF. *n*-Butyllithium was added (1.6 M in hexanes, 10.0 mL, 16.0 mmol, 1.1 eq.) after the mixture was cooled to -78°C. The mixture was stirred for 2 h, followed by the addition of tributylstannyl chloride (4.9 mL, 5.9 g, 18 mmol, 1.3 eq.). The reaction was then allowed to warm to room temperature with overnight stirring, resulting in a clear, colorless solution. The solvent was removed and the residue was dissolved in hexanes and filtered, yielding 7.50 g of a clear, colorless liquid, which was used without further purification. ¹H NMR (300 MHz, CDCl₃) δ (ppm): 6.56 (s, 1H), 4.14 (s, 4H), 1.54 (m, 6H), 1.33 (m, 6H), 1.09 (m, 9H), 0.09 (m, 6H).

2.2.3 Metal Salts

2.2.3.1 *Cis*-Bis(2,2'-bipyridine-*N,N'*) dichlororuthenium(II), **40** [73]

RuCl₃·H₂O (1.56 g, 6.9 mmol, 1 eq.) and 2,2'-bipyridine (2.05 g, 13 mmol, 1.9 eq.) were stirred in 50 mL of DMF. LiCl (1.70 g, 40 mmol, 5.8 eq.) was added and the mixture was refluxed for 5 h. The reaction mixture was then filtered and the volume was reduced to 10 mL under reduced pressure. Acetone was added (50 mL) and the flask was cooled to 0°C overnight, yielding a black solid which was collected by filtration and washed copiously with water until the filtrate was colorless.

A solution of the above product in 50/50 water/ethanol (250 mL) was refluxed for one hour. The solvent volume was then reduced to 10 mL, and the mixture was cooled for 3 h in an ice bath. The product was collected by filtration and washed copiously with water, yielding a black solid which was dried *in vacuo* (1.72g, 54%). The cyclic voltammetry of the solid dissolved in CH₃CN/0.1 M Et₄NClO₄ was identical with a previously synthesized sample of this complex whose purity had been verified by elemental analysis. E_{1/2}(Ru^{3+/2+})(CH₃CN/0.1 M Et₄NClO₄): 0.31 V.

2.2.3.2 *Cis*-Bis(2,2'-bipyridine-*N,N'*) dichloroosmium(II) [74]

This procedure first involves making *cis*-bis(2,2'-bipyridine-*N,N'*) dichloroosmium(III) chloride dihydrate (**41**) followed by reduction of this product to form *cis*-bis(2,2'-bipyridine-*N,N'*) dichloroosmium(II) (**42**).

2.2.3.2.1 *Cis-Bis(2,2'-bipyridine-N,N')* dichloroosmium(III) chloride dihydrate,
41

K_2OsCl_6 (0.51 g, 1 mmol, 1 eq.) and 2,2'-bipyridine (0.35 g, 2.2 mmol, 2.2 eq.) were stirred in DMF (20 mL), producing a reddish brown mixture which turned a darker red upon boiling. Refluxing was continued for 3 h, turning the color brown. At this time, the reaction was cooled to room temperature, and the solvent volume was reduced to about 10 mL. It was then cooled to 0°C and filtered, removing a white powder. 100% ethanol (10 mL) was then added, and the solution was rapidly stirred. Diethyl ether (~250 mL) was added slowly until a cloudy reddish brown suspension resulted. The mixture was allowed to sit, permitting the brown microcrystals to settle. The supernatant solution was then slowly poured off and the solid was collected. It was then washed with ether and air-dried, yielding 0.54 g of a dark brown powder (79%). 1H NMR (300 MHz, CD_3OD) δ (ppm): 8.75 (d, 1H), 7.95 (dd, 1H), 7.74 (d, 1H), 7.43 (dd, 1H).

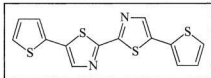
2.2.3.2.2 *Cis-Bis(2,2'-bipyridine-N,N')* dichloroosmium(II), 42

Sodium dithionite (1.04 g) in H_2O (100 mL) was slowly added to a stirred solution of the above product in methanol/DMF (10 mL/ 20 mL). The mixture was stirred over a period of 8 h and then cooled in an ice bath. A purple solid was collected by filtration and washed with ice cold H_2O (2 x 5 mL), ice cold methanol (2 x 2 mL) and ether (2 x 5 mL), yielding 0.24 g of dark brown powder (50%). The voltammetry of this solid matched that for a previously synthesized sample tested by elemental analysis.

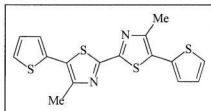
$E_{1/2}(Os^{3+/2+})(CH_3CN/0.1 M Et_4NClO_4)$: 0.04 V.

2.2.4 Bithiazole Monomers

2.2.4.1 5,5'-Bis(2-thienyl)-2,2'-bithiazole, 8 (btbtz)

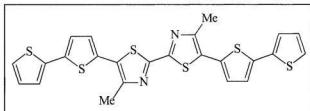


2-Thiophene boronic acid (1.56 g, 12.2 mmol, 3.7 eq.), dissolved in a minimal amount of ethanol, was added to a solution of 5,5'-dibromo-2,2'-bithiazole (1.08 g, 3.3 mmol, 1 eq.) and Pd(PPh₃)₄ (296 mg, 0.08 eq.) in dimethoxyethane (30 mL) under N₂. Next, 2M Na₂CO₃(aq) (10 mL, 20 mmol) was added, and the mixture was heated at reflux for 18 h. The mixture was then cooled, filtered, and the solvent removed. Purification by column chromatography (silica/CH₂Cl₂) yielded 0.93 g of a yellow product (85%). MP 205°C (Lit[37]: 208°C). ¹H NMR (CDCl₃), δ (ppm): 7.92 (s, 1H), 7.35 (d, *J*=5.2 Hz, 1H), 7.29 (d, *J*=3.7 Hz, 1H), 7.09 (dd, *J*=5.1, 3.6 Hz, 1H). *m/z*: 332 (M⁺).

2.2.4.2 5,5'-Bis(2-thienyl)-4,4'-dimethyl-2,2'-bithiazole, 9 (btbmtz)

2-Thiophene boronic acid (1.25 g, 9.8 mmol, 6 eq.) was dissolved in ethanol (15 mL) and added to a stirring solution of 5,5'-dibromo-4,4'-dimethyl-2,2'-bithiazole (0.58 g, 1.6 mmol, 1 eq.) and Pd(PPh₃)₄ (0.19 g, 0.1 eq.) in dimethoxyethane (10 mL) under a flow of nitrogen. 2M Na₂CO₃ (2 mL, 7 mmol, 4.4 eq.) was then added, turning the solution from orange to brown. The mixture was refluxed for 20 h, after which time it was cooled and filtered. Following removal of the solvent, the residue was purified on a CH₂Cl₂/silica column. Evaporation of the solvent yielded 0.13 g of bright yellow solid (22%). MP 225°C (Lit[38]: 225-228°C). ¹H NMR (CDCl₃), δ (ppm): 7.40 (d, *J*=5.5 Hz, 1H), 7.24 (d, *J*=3.7 Hz, 1H), 7.13 (dd, *J*=5.1, 3.6 Hz, 1H), 2.66 (s), 3H.

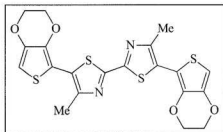
2.2.4.3 5,5'-Bis(2,2'-bithienyl)-4,4'-dimethyl-2,2'-bithiazole, 43



5,5'-Dibromo-4,4'-dimethyl-2,2'-bithiazole (117 mg, 0.33 mmol, 1 eq.), 5-tributylstannyl-2,2'-bithiophene (0.58 g), and Pd(PPh₃)₂Cl₂ (24 mg, 0.033 mmol, 0.1 eq.) were stirred in anhydrous DMF (40 mL) under Ar and heated to 90°C (under a foil cover). The color of this mixture changed from brown to dark orange over the course of the reaction. After 14 h, TLC (silica/CH₂Cl₂) showed two spots. The reaction mixture was cooled and filtered, and the solvent was evaporated. Column chromatography (silica/CH₂Cl₂) produced two bands. The second, broad, orange band was collected and the solvent was evaporated to produce a bright orange solid. The ¹H NMR spectrum contained the expected signals in addition to other aromatic peaks. The solid was again columned (silica, 80: 20 petroleum ether:ethyl acetate), producing a bright red solid (60 mg). MP 238-243°C. ¹H NMR (300 MHz, CDCl₃) δ (ppm): 7.27 (d, 1H), 7.23 (d, *J*=3.7 Hz, 1H), 7.17 (d, *J*=3.8 Hz, 1H), 7.13 (d, *J*=3.8 Hz, 1H), 7.05 (dd, *J*=5.0, 3.6 Hz, 1H), 2.69 (s, 3H). *m/z*: 524 (M⁺).

2.2.4.4 5,5'-Bis(5-3,4-(ethylenedioxy)thiophene)-4,4'-dimethyl-2,2'-bithiazole,

44



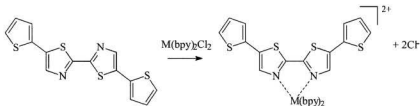
5,5'-Dibromo-4,4'-dimethyl-2,2'-bithiazole (316 mg, 0.89 mmol, 1 eq.), 5-tributylstannyl-3,4-(ethylenedioxy)thiophene (1.50 g), and $\text{Pd}(\text{PPh}_3)_2\text{Cl}_2$ (40 mg, 0.06 eq.) were stirred in anhydrous DMF (40 mL) under Ar, and the temperature was maintained between 110°C and 118°C for 12 h. The color of this mixture changed from clear yellow to orange to brown over the course of the reaction. The progress of the reaction was followed by TLC, to confirm that the 5,5'-dibromo-4,4'-dimethylbithiazole reactant had been completely consumed. The reaction mixture was cooled, filtered, and boiled in CH_2Cl_2 (2L). This mixture was filtered and the residue was washed with CH_2Cl_2 until the filtrate was almost colorless. Evaporation of the solvent produced a reddish brown semisolid (410 mg) which was crystallized from 5% MeOH in CHCl_3 (2L) to produce a very fine, bright orange powder (172 mg). MP >250°C. ^1H NMR (300 MHz, CDCl_3) δ (ppm): 6.44 (s, 1H), 4.33 (m, 2H), 4.26 (m, 2H), 2.63 (s, 3H).

2.2.5 Transition Metal Complexes

Two routes to synthesize transition metal coordinated polymers were investigated. One involved synthesis of the organic polymer first, followed by coordination of the metal center. This method has been applied successfully for coordination of a rhenium center to electrosynthesized poly[5,5'-bis(2-thienyl)-2,2'-bithiazole], resulting in occupation of about 60% of the coordination sites [37]. Attempts to achieve coordination of ruthenium to the same polymer, in the form of both an electropolymerized film and a chemically prepared powder were made; however, neither method proved fruitful, with no polymer-metal coordination evidenced by cyclic voltammetry. A second route involving the syntheses of transition metal complexes of electropolymerizable monomers would, if successful, result in metallopolymers having 100% coordination to the organic backbone. To this end, $\text{Ru}(\text{bpy})_2^{2+}$ and $\text{Os}(\text{bpy})_2^{2+}$ complexes of the above ligands were prepared for anodic polymerization.

Complexes were made by reacting the bis(2,2'-bipyridine)metal(II) chloride with the appropriate ligand in solvents ranging from aqueous ethanol (70-80%) to glycerol (Scheme 2.3). Progress was monitored by following the reaction with gel-permeation chromatography (GPC).

Removal of unreacted ligand by filtration and precipitation of either the perchlorate or hexafluorophosphate salt was followed by purification on a Sephadex Lh-20 column in methanol and/or crystallization. Yields for metal perchlorates are reported in parentheses.



Scheme 2.3: Complexation of a 4-ring bis(thienyl)bithiazole ligand.

2.2.5.1 Tris(2,2'-bithiazole)ruthenium(II) hexafluorophosphate, $\text{Ru}(\text{btz})_3(\text{PF}_6)_2$ [75]

A procedure for the preparation of tris(2,2'-bipyridine)ruthenium chloride was followed [75]. A mixture of 2,2'-bithiazole (1.01 g, 6.0 mmol, 3 eq.) and $\text{RuCl}_3 \cdot \text{H}_2\text{O}$ (0.45 g, 1.9 mmol, 1 eq.) in H_2O (40 mL) was refluxed long enough to dissolve the reactants. A solution of sodium phosphinate was prepared by adding enough NaOH to phosphinic acid (31 %, 1.2 mL) to form a cloudy solution, followed by the addition of enough phosphinic acid to redissolve the precipitate formed. This solution was added to the above mixture and then boiled for 2.5 h, resulting in a color change from green to brown to reddish brown. The solution was filtered and a solution of NH_4PF_6 was added to the filtrate. The dark red product was collected by suction filtration and washed well with water (1.64 g, 92 %). ^1H NMR (500 MHz, acetone- d_6) δ (ppm): 8.34 (d, $J=3.4$ Hz, 1H), 7.59 (d, $J=3.3$ Hz, 1H). ^{13}C NMR (125 MHz, acetone- d_6) δ (ppm): 160.9; 144.5; 127.9. Elemental analysis: Calc'd for $\text{C}_{18}\text{H}_{12}\text{F}_{12}\text{N}_6\text{P}_2\text{RuS}_6$: C 24.14%, H 1.35%, N 9.38%. Found: C 23.28%, H 1.41%, N 9.10%. m/z : 751 (29%, $\text{M} - \text{PF}_6^-$), 303 (44%, $\text{M} - 2\text{PF}_6^-$; $z = 2+$).

**2.2.5.2 Bis(2,2'-bipyridine)[2,2'-bithiazole]ruthenium(II)
hexafluorophosphate, Ru(btz)(bpy)₂(PF₆)₂**

A mixture of Ru(bpy)₂Cl₂ (290 mg, 0.60 mmol, 1 eq.) in 75% aqueous ethanol (20 mL) was refluxed until the metal salt was fully dissolved. 2,2'-Bithiazole (114 mg, 0.68 mmol, 1.1 eq.) was added and the mixture was refluxed (24 h). GPC of the reaction mixture showed only one orange band, indicating that the reaction was complete. The solution was then cooled, filtered, and the solvent removed. The residue was redissolved in H₂O, cooled in an ice bath, and precipitated as the hexafluorophosphate salt by addition of a KPF₆(aq) solution. The dark red product was then filtered, dried, and crystallized from CH₃CN/toluene to produce violet needles (313 mg, 60%). ¹H NMR (500 MHz, acetone-d₆) δ (ppm): 8.81 (d, *J*=8.1 Hz, 2H), 8.30 (d, *J*=3.4 Hz, 1H), 8.26-8.21 (m, 2H), 8.12 (d, *J*=5.7 Hz, 1H), 8.05 (d, *J*=5.5 Hz, 1H), 7.65-7.50 (m, 3H). ¹³C NMR (125 MHz, acetone-d₆) δ (ppm): 160.7; 158.7; 158.2; 153.5; 153.2; 143.6; 139.0; 138.9; 128.9; 128.5; 128.4; 125.2; 125.0. Elemental analysis: Calc'd for C₂₆H₂₀F₁₂N₆P₂RuS₂: C 35.83%, H 2.31%, N 9.64%. Found C 35.83%, H 2.33%, N 9.63%. *m/z*: 727 (44%, M - PF₆⁻), 291 (42%, M - 2PF₆⁻; *z* = 2+).

2.2.5.3 Bis(2,2'-bipyridine)[5,5'-bis(2-thienyl)-2,2'-bithiazole]ruthenium(II) hexafluorophosphate, Ru(btbtz)(bpy)₂(PF₆)₂

A mixture of Ru(bpy)₂Cl₂ (201 mg, 0.41 mmol, 1 eq.) in 80% aqueous ethanol (20 mL) was refluxed until the metal salt was fully dissolved. 5,5'-Bis(2-thienyl)-2,2'-bithiazole (159 mg, 0.47 mmol, 1.1 eq.) was added and the mixture was refluxed for 2 d, by which time GPC indicated that reaction was complete. The solution was then cooled, filtered, and the solvent was removed. The residue was redissolved in H₂O, cooled in an ice bath, and precipitated as the hexafluorophosphate salt by addition of a NH₄PF₆(aq) solution. The dark brown product was then filtered and crystallized from acetone/H₂O to yield fine, purple needles (352 mg, 79%) which were vacuum dried overnight. (M(ClO₄)₂: 59%). ¹H NMR (500 MHz, acetone-d₆) δ (ppm): 8.79 (d, *J*=8.1 Hz, 1H), 8.78 (d, *J*=8.0 Hz, 1H), 8.31 (d, *J*=5.7 Hz, 1H), 8.26-8.19 (m, 2H), 8.06 (d, *J*=5.7 Hz, 1H), 7.80 (s, 1H), 7.70 (d, *J*=5.1 Hz, 1H), 7.66 (t, *J*=5.7 Hz, 1H), 7.58 (t, *J*=5.8 Hz, 1H), 7.50 (d, *J*=3.7 Hz, 1H), 7.17 (dd, *J*=5.1, 3.8 Hz, 1H). ¹³C NMR (125 MHz, acetone-d₆) δ (ppm): 158.7; 158.3; 156.9; 153.8; 153.1; 140.1; 139.3; 139.1; 139.0; 130.9; 130.3; 129.8; 129.6; 128.9; 128.5; 125.21; 125.1. Elemental analysis: Calc'd for C₃₄H₂₄F₁₂N₆P₂RuS₄·2H₂O: C 38.10%, H 2.63%, N 7.84%, S 11.96%. Found: C 38.09%, H 2.28%, N 7.87%, S 12.17%. *m/z*: 891 (37%, M - PF₆), 373 (100%, M - 2PF₆, *z* = 2+).

2.2.5.4 Bis(2,2'-bipyridine)[5,5'-bis(2-thienyl)-2,2'-bithiazole]osmium(II) hexafluorophosphate, Os(btbtz)(bpy)₂(PF₆)₂

A mixture of Os(bpy)₂Cl₂ (97 mg, 0.17 mmol, 1 eq.) in 20 mL of 70% aqueous ethanol was refluxed until the metal salt was fully dissolved. 5,5'-Bis(2-thienyl)-2,2'-bithiazole (58 mg, 0.17 mmol, 1 eq.) was then added and the reaction mixture was refluxed for 5 d, by which time GPC indicated the reaction was complete. The solution was then cooled, filtered, and the solvent was removed. The residue was redissolved in H₂O, cooled to 0°C, and precipitated as the hexafluorophosphate salt by addition of a NH₄PF₆(aq) solution. The product was collected by filtration, crystallized from acetone/ether, and air dried (89 mg, 42%) (M(ClO₄)₂: 67%). ¹H NMR (500 MHz, acetone-d₆) δ (ppm): 8.78 (d, *J*=8.1 Hz, 1H), 8.77 (d, *J*=8.1 Hz, 1H), 8.15 (d, *J*=5.7 Hz, 1H), 8.06 (t, *J*=7.4 Hz, 1H), 8.02 (t, *J*=7.4 Hz, 1H), 7.97 (d, *J*=5.7 Hz, 1H), 7.76 (s, 1H), 7.69 (d, *J*=5.1 Hz, 1H), 7.57 (t, *J*=7.2 Hz, 1H), 7.52 (t, *J*=7.2 Hz, 1H), 7.47 (d, *J*=3.7 Hz, 1H), 7.17 (dd, *J*=5.1, 3.8 Hz, 1H). ¹³C NMR (125 MHz, acetone-d₆) δ (ppm): 160.5 (2C); 158.6; 153.3; 152.1; 140.9; 138.6; 138.5 (2C); 130.9; 130.4; 129.7 (2C); 129.3; 129.0; 125.3; 125.2. Elemental analysis: Calc'd for C₃₄H₂₄F₁₂N₆OsP₂S₄2[(CH₃)₂CO]: C 38.71%, H 2.92%, N 6.77% S 10.33%. Found: C 39.43%, H 2.88%, N 6.28%, S 10.62%. *m/z*: 935 (23%, (M - ClO₄)₂), 418 (100%, M - 2 ClO₄⁻, *z* = 2+).

**2.2.5.5 Bis(2,2'-bipyridine)[5,5'-bis(2-thienyl)-4,4'-dimethyl-2,2'-
bithiazole]ruthenium(II) hexafluorophosphate,
Ru(btbtz)(bpy)₂(PF₆)₂**

A mixture of Ru(bpy)₂Cl₂ (0.58 mmol, 1.1 eq.) in 75% aqueous ethanol (20 mL) was refluxed until the metal salt was fully dissolved. 5,5'-Bis(2-thienyl)-4,4'-dimethyl-2,2'-bithiazole (189 mg, 0.52 mmol, 1 eq.) and chloroform (5 mL, to increase ligand solubility) were added and the mixture was refluxed. After 4 d, GPC indicated that only a small fraction of the starting materials had reacted so the mixture was evaporated to dryness and glycerol (20 mL) was added. Refluxing was continued for 2 d, after which time GPC showed no reactants remained. The solution was cooled, diluted with H₂O (100 mL), and filtered. After cooling to 0°C, the dark red product was precipitated as the hexafluorophosphate salt by addition of a KPF₆(aq) solution. The product was then filtered and crystallized from H₂O/acetone to yield violet needles, which were air dried (364 mg, 62%). (M(ClO₄)₂; 83%). ¹H NMR (500 MHz, acetone-d₆) δ (ppm): 8.85 (d, *J*=8.1 Hz, 1H), 8.82 (d, *J*=8.2 Hz, 1H), 8.41 (d, *J*=5.2 Hz, 1H), 8.28 (t, *J*=7.8 Hz, 1H), 8.20 (t, *J*=7.8 Hz, 1H), 8.04 (d, *J*=5.3 Hz, 1H), 7.77 (d, *J*=5.1 Hz, 1H), 7.68 (t, *J*=6.4 Hz, 1H), 7.54 (t, *J*=6.5 Hz, 1H), 7.40 (d, *J*=3.1 Hz, 1H), 7.22 (t, *J*=4.3 Hz, 1H), 1.87 (s, 3H). ¹³C NMR (125 MHz, acetone-d₆) δ (ppm): 158.6; 157.8; 157.2; 153.9; 152.9; 152.4; 138.8; 138.5; 132.0; 130.5; 130.4; 130.0; 129.0; 128.6; 128.4; 125.1; 125.0; 14.8. *m/z*: 387 (100%, M - 2PF₆⁻; *z* = 2+), 360 (btbtz). The identity of this compound was verified by X-ray crystallography (Appendix E).

2.2.5.6 Bis(2,2'-bipyridine)[5,5'-bis(2-thienyl)-4,4'-dimethyl-2,2'-bithiazole]osmium(II) perchlorate, Os(btmbtz)(bpy)₂(ClO₄)₂

A mixture of Os(bpy)₂Cl₂ (78 mg, 0.14 mmol, 1 eq.) in 70% aqueous ethanol was refluxed until the metal salt was dissolved. 5,5'-Bis(2-thienyl)-4,4'-dimethyl-2,2'-bithiazole (51.1 mg, 0.14 mmol, 1 eq.) was then added and the mixture was refluxed (24 h). The reaction, as followed by GPC, appeared to be very slow. After evaporation of the solvent, glycerol was added and the mixture was refluxed for five days, when it appeared that no reactant remained (GPC). The mixture was diluted with H₂O and filtered. Addition of a solution of sodium perchlorate produced a dark brown, cloudy suspension. The product was collected by filtration and purified by GPC (Sephadex Lh-20, MeOH). Removal of the solvent yielded black flakes (83.7 mg, 71%). ¹H NMR (300 MHz, CD₃OD) δ (ppm): 8.69 (d, J=8.0 Hz, 1H), 8.66 (d, J=8.3 Hz, 1H), 7.99 (t, J=8.0 Hz, 1H), 7.93 (d, J=5.7 Hz, 1H), 7.86 (t, J=7.8 Hz, 1H), 7.68 (d, J=5.2 Hz, 1H), 7.63 (d, J=5.6 Hz, 1H), 7.56 (t, J=6.7 Hz, 1H), 7.39-7.33 (m, 2H), 7.18 (dd, J=5.2, 3.8 Hz, 1H). *m/z*: 432 (100%, M - 2ClO₄⁻, z = 2+).

2.2.5.7 Bis(2,2'-bipyridine)[5,5'-bis(3-methoxy-2-thienyl)-4,4'-dimethyl-2,2'-bithiazole]osmium(II) hexafluorophosphate, Os(bmtbmtz)(bpy)₂(PF₆)₂

A mixture of Os(bpy)₂Cl₂ (69 mg, 0.12 mmol, 1 eq.) and 5,5'-bis(3-methoxy-2-thienyl)-4,4'-dimethyl-2,2'-bithiazole (51 mg, 0.12 mmol, 1 eq.) in glycerol (15 mL) were refluxed until the reactants dissolved. Methanol (3 mL) was added to increase the solubility of the ligand. The mixture was then refluxed for 3 d, after which time GPC indicated the reaction had finished. The mixture was diluted with H₂O and filtered. The product was precipitated

as the hexafluorophosphate salt by addition of NH_4PF_6 (aq). Suction filtration yielded a dark brown powder which was purified on Lh-20 Sephadex (MeOH). Following removal of the solvent, the product was crystallized from methanol/ether and filtered to yield 92 mg of black powder (63%), which ^1H NMR indicated was not pure. ^1H NMR (500 MHz, acetone- d_6) δ (ppm): 8.80 (d, 1H), 8.17 (d, 1H), 8.03 (t, 1H), 7.99 (t, 1H), 7.90 (d, 1H), 7.72 (d, 1H), 7.57 (t, 1H), 7.47 (t, 1H), 7.25 (d, 1H), 4.08 (s, 3H), 1.92 (s, 3H). There were also small impurity peaks over the 4 - 3.3 ppm range and a large singlet at ca. 2.8 ppm.

2.2.6 Conjugated Organic Polymers

2.2.6.1 Poly[5,5'-bis(2-thienyl)-2,2'-bithiazole], poly-(btbtz)

A mixture of 5,5'-bis(2-thienyl)-2,2'-bithiazole (102 mg) in 35 mL of dry CH_3CN was refluxed with stirring (to dissolve) under a flow of nitrogen. To this was added a CH_3CN solution of anhydrous FeCl_3 (0.16 g in 9 mL), turning the solution of monomer from yellow to a dark green. Stirring was continued overnight. After cooling in an ice bath, the solution was filtered and washed with dilute HCl. The product was then boiled in CHCl_3 to extract unreacted monomer, leaving a dark brown powder (88 mg, 87%). The solid was not soluble in a wide variety of organic solvents, and concentrated HCl and HNO_3 . When trifluoroacetic acid (TFA- d_6) was added to a small quantity of the solid (with sonication) a deep purple solution was obtained; however, a considerable quantity of the solid remained undissolved. ^1H NMR spectroscopy of this solution showed four resonances. Since dissolution of the monomer in trifluoroacetic acid produces a deep red solution, this suggested dimeric product. A heavier, crosslinked product (polymer) most likely remained undissolved.

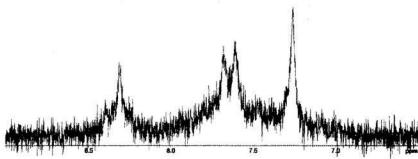


Figure 2.2: ^1H NMR of the solution obtained by treatment of poly(btbtz) powder with TFA-d_4 .

Chapter 3

Electronic and Electrochemical Characterization of 2,2'-Bithiazole-Based Monomers and Polymers

3.1 Experimental

All electronic absorption measurements were carried out on a CARY-5E UV-Vis-NIR spectrophotometer. Absorption spectra of the monomers were collected on solutions contained in quartz cuvettes (path length = 1 cm). For the polymers, an Indium Tin Oxide (ITO) electrode was coated with a thin film by electropolymerization from a dilute monomer solution.

Semi-empirical calculations for orbital energies were made with the SPARTAN molecular modeling package at the AM1 level of theory.

Cyclic voltammetry of the ligands were conducted in dichloromethane / tetrabutylammonium perchlorate (Bu_4NClO_4 , 0.1 M) solutions, unless otherwise noted. Polymer films were grown on platinum disk electrodes (area = 0.0078 cm^2 or 0.0052 cm^2), and tests were carried out in $\text{CH}_3\text{CN} / 0.1 \text{ M Et}_4\text{NClO}_4$. Acetonitrile was purified by first passing it over activated alumina and then refluxing it over CaH_2 for two hours under UHP grade argon before collecting.

3.2 Monomers Containing 2,2'-Bithiazole

The 2,2'-bithiazole based ligands considered in this project were chosen to allow electropolymerization at moderate potentials. Being less electron deficient than materials incorporating 2,2'-bipyridine, the oxidized intermediates (i.e., radical cations) formed should be more stable and be able to participate in radical coupling to form polymer films.

This same reasoning should hold true for metal complexes involving these same ligands.

The monomers' electronic properties were characterized by electronic absorption spectroscopy and cyclic voltammetry. Electronic absorption experiments provide an estimate of the HOMO-LUMO energy gap (the bandgap, E_g), which is estimated from the onset of absorption. Cyclic voltammetry can also yield energy bandgap information, from the difference between a ligand's formal potentials for oxidation and reduction. In addition, cyclic voltammetry is particularly useful for investigating the electropolymerization of the ligands and their complexes. Theoretical investigations of these systems can provide insight into the effects of structure (e.g. substituents) on HOMO and LUMO energies.

3.3 Electronic Absorption Spectroscopy

In this section, HOMO-LUMO energy gaps are estimated from the onset of the π - π^* absorption peak. The theory for this is explained by invoking the Franck-Condon principle [76]:

Following light absorption, a new, excited species is created in which electron density is redistributed within the molecule. This movement of the electrons occurs much faster than the nuclei of the absorbing species can adjust, and so the new electronic fields generated by excitation will subsequently cause the bonds between these nuclei to oscillate until a new geometry corresponding to the final electronic state is reached. In Figure 3.1, it is seen that the absorbing molecule is in the ground vibrational state of the ground electronic state. Absorption of light causes a transition into an excited vibrational energy

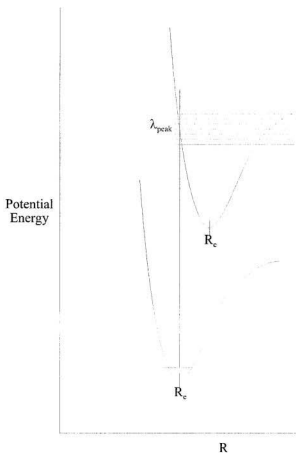


Figure 3.1: Potential energy diagram representing an absorbing bithiazole monomer in solution. Bottom curve - before light absorption. Top curve - after light absorption, a transition occurs from the ground vibrational level of the ground electronic state to the vibrational state directly above it.

of the excited electronic state (upper curve). In the ground electronic state, the most probable location of the nuclei is at their equilibrium separation, R_e . Because nuclear movement is slow in comparison to this electronic shift, the transition into the excited state is most likely to occur for a geometry most closely resembling the ground state. This is shown by the vertical transition between the two curves. Since this transition marks the most probable point of termination, it corresponds to the absorption peaks seen in Figure 3.2. However, from Figure 3.1, it can be seen that this does not correspond to the transition between the lowest vibrational state of the ground electronic state to the lowest vibrational level of the excited electronic state. This transition is less probable, and thus occurs with less intensity. Its energy must therefore be estimated from the lowest energy (highest wavelength) region of the absorption curve.

Comparisons between absorption onsets for monomers and polymers are not possible, due to difficulties in assigning these data for polymer films, as will be seen later. For this reason, E_g for the polymer films studied here are unknown. Still, the absorption data are useful in describing changes in the Franck-Condon electronic structures of the monomer skeletons accompanying polymerization.

3.3.1 Monomers

The electronic absorption spectra of the π -conjugated organic monomers studied in this project are presented in Figure 3.2. The absorption spectra of all bithiazole ligands are fairly simple, dominated by a broad peak attributable to the monomers' π - π^* transitions. The wavelengths for absorption onsets (λ_o) corresponding to π - π^* transitions for the

monomers are presented in Table 3.1. HOMO-LUMO energies from λ_0 are also presented. Longer wavelength peak absorptions correspond to lower energy transitions (lower bandgaps). The lowest energy π - π^* transition in the series of monomers occurs for **bmtbmtz**, as a result of the substituent effects discussed in section 2.2.1. As expected, the HOMO-LUMO gap is seen to drop with increased substitution. Two methyl substituents can be seen to decrease the bandgap of **btbtz** by *ca.* 0.31 eV, and the methoxy groups of **bmtbmtz** by another 0.04 eV.

	λ_0 / nm	E_g / eV
btbtz	457	2.73
btbmtz	512	2.42
bmtbmtz	520	2.38

Table 3.1: Onset of absorption (λ_0 , nm) for monomers in CH_2Cl_2 .

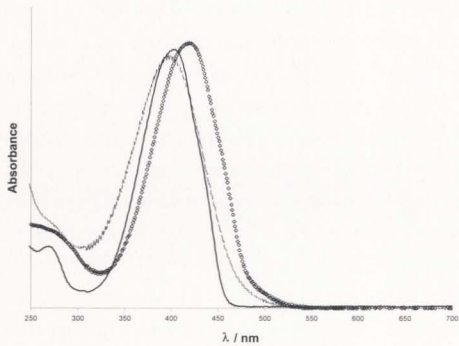


Figure 3.2: Electronic absorption spectra for the monomers in CH_2Cl_2 : — btbtz; - - - btbmtz;

◊ bmtbmtz.

3.3.2 Polymers

Since the conjugated organic polymers of this study are insoluble in organic solvents, electronic absorption experiments must be carried out on thin films deposited on conducting glass (ITO) electrodes. The absorption peak is used here in lieu of the onset of absorption. One immediately noticeable feature in the spectra for these films (Figure 3.3) is their broad profile, in contrast to the sharp π - π^* peaks observed for the less conjugated monomers. In addition, the peak absorbance is shifted towards longer wavelengths (lower energy) as the excited species formed by light absorption are delocalized over an extended conjugation system, resulting in peak absorption shifts of 40-53 nm (0.27-0.37 eV) upon polymerization of the bithiazole monomers of this study [77]. The broadening of the absorbance spectra is attributed to the existence of many closely spaced orbital energies for the polymer film. The polymer product deposited on the ITO slide by electropolymerization likely consists of a range of conjugation lengths, separated by nonconjugated linkages (α , β -connectivity). Chain defects created by doping during electrochemical polymerization further enhance this broadening. Both of these occurrences provide strong evidence of an extended conjugation system.

* In a solid polymer film, solvent influences on light absorption are restricted to sites at the film-solution interface, and should not contribute to a significant degree in these electronic absorption experiments. For conjugated monomer (soluble) species, solvent effects will influence the energy of light absorption, and thus it is acknowledged here that the longer wavelength absorption observed for the polymer films may not only result from an extended conjugation network.

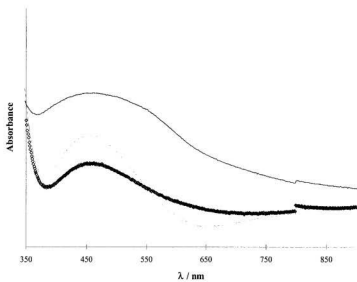


Figure 3.3: Electronic absorption spectra for bithiazole polymers on ITO electrodes:

- poly-btbtz; - - - poly-btbmtz; ⋄ poly-bmtbmtz.

	$\lambda_{(\text{max, monomer} / \text{nm})}$	$\lambda_{(\text{max, polymer} / \text{nm})}$
btbtz	401	450
btbmtz	396	449
bmtbmtz	415	455

Table 3.2: Comparison of peak absorbances for monomers and polymer films on ITO electrodes.

3.3.3 Effect of Acid

The diimine coordination sites in the bithiazole monomers and polymers are susceptible to protonation. A visible change is produced upon treatment of both monomers and polymers with strong acids such as sulfuric acid and perchloric acid. **Bbtz** is seen to change color from yellow to a yellow-orange when just a few drops of perchloric acid are added to an acetonitrile-monomer solution. This behavior is demonstrated in the electronic absorption spectra. Figure 3.4 shows a red shift of about 50 nm (*ca.* 0.3 eV) for **bbtz** upon acidification. Similarly, when poly-**bbtz** is protonated, a dramatic color change results, the brown, neutral polymer dissolving to produce a deep blue solution (Figure 3.5). Semiempirical calculations modeled at the AM1 level of theory indicate that the energies of the frontier orbitals are both affected considerably by diprotonation. For **bbtz**, the HOMO and LUMO energies decreased, by ~ 5.6 and 7.2 eV, respectively, reducing the bandgap by about 1.6 eV. These results predict a bandgap much smaller than that indicated by the absorption data, due to the influence of solvation effects and the presence of counterions on the experimental measurement.

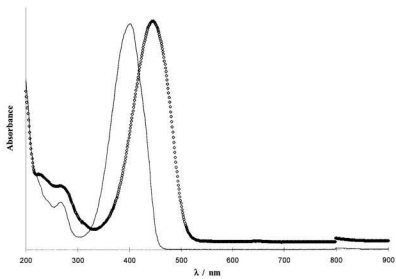


Figure 3.4: The effect of adding acid to **btbzt**: — **btbzt** in CH_3CN ; \diamond **btbzt** in $\text{CH}_3\text{CN} + \text{HClO}_4$.

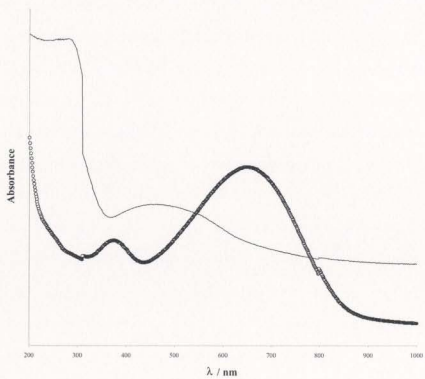


Figure 3.5: Effect of acid on poly-btbtz. — poly-btbtz on ITO electrode; o poly-btbtz in conc. H_2SO_4 .

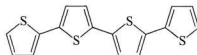
3.4 Semi-empirical Calculations

Table 3.3 shows calculated HOMO and LUMO energies for the series of ligands investigated, as well as for 2,2'-bithiazole (**btz**), tetrathiophene (**tth**), and 5,5'-bis(2-thienyl)-2,2'-bipyridine (**btbpy**). Comparisons between these data demonstrate substituent effects on the frontier orbitals of 2,2'-bithiazole. For example, thiophene end groups affixed to the 5-positions of each thiazole ring will raise the HOMO energy, while lowering the LUMO energy. Not only does this permit oxidation of **btbztz** at potentials less positive than for **btz**, but these substituents are predicted to lower the HOMO-LUMO gap. The bithiazole core of **btbztz** is predicted to lower its HOMO energy relative to that for tetrathiophene, but it will also lower the LUMO by about the same amount. Consequently, the predicted energy gaps are not that different. This is reflected in experimental data ($\lambda_{\text{Max, th}}=390 \text{ nm}$) [78]. For the 2,2'-bipyridine core, the HOMO energy is lower still, and the LUMO energy is close to that predicted for tetrathiophene. Thus, the bandgap is calculated to be larger for **btbpy** than for **btbztz**.

It can be seen that methyl and methoxy substituents are effective in raising the HOMO energy, facilitating oxidation. However, a similar energy increase is also produced for the LUMO energy. Consequently, HOMO-LUMO energy gaps for the four ring series (**btbztz**, **btbmtz**, **bmtbmtz**) are only slightly different. The methoxy substituents will be more effective than methyl groups in stabilizing the oxidized form of these monomers, and the HOMO and LUMO energies predict this monomer to have the lowest bandgap.

	HOMO / (eV)	LUMO / (eV)	E _{HOMO-LUMO} / (eV)
btbtz	-8.39404	-1.41751	6.97653
btbmtz	-8.29632	-1.33009	6.96623
bmtbmtz	-8.11097	-1.26399	6.84698
btz	-9.14336	-1.09617	8.04719
tth (45)	-8.07200	-1.10669	6.96531
btbpy	-8.50293	-1.13566	7.36727

Table 3.3: HOMO and LUMO energies calculated at the AM1 level.



3.5 Cyclic Voltammetry

3.5.1 Cyclic Voltammetry of Monomers

Cyclic voltammetry was employed to gather information on the redox properties of the bithiazole-based monomers. Monomer formal potentials are shown in Table 3.4. The difference between these potentials corresponds approximately to the HOMO-LUMO energy bandgap. Monomer oxidation invariably produced an irreversible wave, so only peak potentials are assigned for these processes ($E_{pa, Ox}$). Reduction of the monomers always yielded a reversible waveform, and so formal potentials are assigned here (E°_{Red}).

Oxidation and reduction profiles for **btbtz** are illustrated in Figure 3.6. This voltammogram was obtained by first scanning the potential of the working electrode through the oxidation peak potential, followed by examination of the reductive electrochemistry in a separate experiment. It was necessary to polish the electrode between oxidative and reductive scans in order to avoid film deposition during the former, which will affect the reductive electrochemistry of the monomer, as detailed later. For all voltammograms, the potential region between oxidation and reduction waves produces negligible current, since there are no accessible energy states for occupation. This region falls within the HOMO-LUMO energy gap. An estimate of the energy gap is thus reported as the difference in the obtained peak and formal potentials.

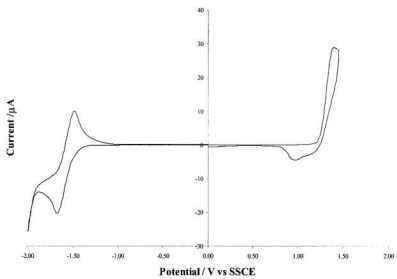


Figure 3.6: Cyclic Voltammery of 10 mM **bbtz** in CH_2Cl_2 / 0.1M Bu_4ClO_4 . $A=0.0052 \text{ cm}^2$;

$\nu=100 \text{ mV sec.}$

	$E_{\text{pa Ox}} / \text{V}$	$E^{\circ}_{\text{Red}} / \text{V}$	Energy HOMO-LUMO / eV
btbtz	1.36	-1.65	3.01
btbmtz	1.30	-1.65	2.95
bmtbmtz	0.94	-1.7	2.64

Table 3.4: Monomer oxidation and reduction potentials evaluated from electrochemical data (vs SSCE in $\text{CH}_2\text{Cl}_2/\text{Bu}_4\text{NClO}_4$).

It appears that the electrochemical data indicate that the substituents employed in the first series have a more pronounced effect on the HOMO energy than on the LUMO energy, since the formal potentials for reduction of the four-ring series do not deviate to any great extent (50 mV between unsubstituted **btbtz** and tetrasubstituted **bmtbmtz**), while the two methyl and methoxy substituents of **bmtbmtz** cause a 420 mV decrease in the peak potential for oxidation, relative to **btbtz**.

3.5.2 Electropolymerization

In this work, most of the polymers studied were grown by potential cycling. This involved cycling the potential of the working electrode through the monomer oxidation wave from a potential where no redox process was observed, usually 0 V. Film growth was monitored by current increases on successive scans. These currents are much larger than can be accounted for by diffusion controlled electrochemistry, and are a result of the electrochemistry of the growing film and an increasing surface area concurrent with the film's growth [79]. The advantages of generating polymer films *via* anodic polymerization were discussed in Section 1.3.

The anodic polymerization of **btbtz** [37], **btbmtz**, and **bmtbmtz** [38] have been reported. A cyclic voltammogram recorded for the electropolymerization of **btbtz** is shown in Figure 3.7. For all bithiazole monomers, the second and subsequent cycles exhibit new waves at lower potentials than observed for the monomer oxidation wave. Presumably, radical coupling yields products which can undergo oxidation at lower potentials than the parent monomer, yielding greater conjugation length (polymerization). Since oxidation of these products will allow further coupling, the voltammogram becomes broadened. This behavior is typical of polythiophenes and other electropolymerizable systems, and is observed because of an increasing number of electronic energy states which are accessible to excitation in the polymer that is formed.

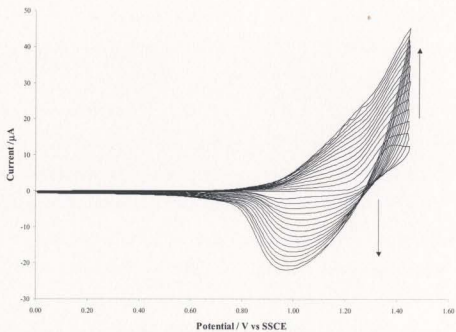


Figure 3.7: Anodic polymerization of 5.5 mM **btbzt** with recurrent potential scans in $\text{CH}_2\text{Cl}_2 / 0.1 \text{ M Bu}_4\text{NPF}_6$ ($\nu = 100 \text{ mV sec}^{-1}$). $A=0.0052 \text{ cm}^2$. Current increases with scan number.

The appearance of a new wave during the polymerization step is most apparent for **btbmtz**, which shows a distinct, new wave centered at about 1.13 V vs SSCE (Appendix A). Not surprisingly, **btbmtz** can be polymerized at a lower potential than **btbtz** (1.3 V vs 1.45 V). It was possible to electropolymerize a 2.5 mM dichloromethane solution of **btbmtz** in CH_2Cl_2 at potentials as low as 0.8 V vs SSCE. A shoulder appears at ~ 0.55 V during cycling, but when polymerization is carried out at 1V, this shoulder is not seen.

3.5.3 Polymer Films

The behavior of the energy bandgap as a function of chain length has been modeled at the semi-empirical level [80]. In a report concerning monomers through seximers of acetylene, thiophene, pyrrole, and thiazole, a decrease of the HOMO-LUMO gap accompanied increased conjugation length. The onset of oxidation, or p-doping, should be seen at potentials lower than for the parent monomer, owing to the greater degree of delocalization which exists in the polymer. This is experimentally observable in voltammograms obtained for polymer coated electrodes. Polymer films generated by potential cycling were transferred to monomer-free electrolyte solutions ($\text{CH}_2\text{Cl}_2/\text{Bu}_4\text{NClO}_4$) after washing with acetone. p-Doping (oxidation) and n-doping (reduction) potentials were estimated from the onset of oxidation and reduction, respectively, in the voltammograms for these films.

The cyclic voltammogram shown for poly-**btbtz** (Fig 3.8) demonstrates the effect of doping on the electrochemistry of a polymer film. The solid curve presents the voltammogram of an as-grown film initially scanned to positive potentials, while the

dashed curve is for a film grown under the same conditions, but first scanned to negative potentials. For the first case, the film was scanned to a potential just below the oxidation peak (not shown) at *ca.* +1.6 V. After the scan direction is switched, two undoping peaks are observed (+1.28 V and +0.84 V). Continuing the scan, a cathodic peak at -1.44 V (attributable to trapped ions in the film) precedes reversible n-doping/undoping at a formal potential of -1.57 V. For the second curve, n-doping requires a lower potential (*ca.* -1.8 V), and does not exhibit the reversible behavior shown for the solid curve. The undoping peak is seen to appear at approximately the same potential as before, while the onset of p-doping of the polymer is now seen at a lower potential. A peak at +0.66 V and a reversible wave at $E^{\circ} = +1.23$ V are also now present. For both films, a small, reversible peak centered at *ca.* -0.3 V is observed. This process may correspond to n-doping/undoping of protonated poly-**btbtz** segments, which should occur at considerably less negative potentials than for a deprotonated structure (see section 3.3).

The stark contrast in the appearance of these two voltammograms derives from ion transport effects. For an untested poly-**btbtz** film (grown from a 0.1 M $\text{Bu}_4\text{NPF}_6 / \text{CH}_2\text{Cl}_2$ / monomer solution), oxidation or reduction in 0.1 M $\text{Et}_4\text{NClO}_4 / \text{CH}_3\text{CN}$ results in structural changes in the polymer associated with an ingress/egress of counterions (necessary to balance the charge generated by doping) and solvent. A “break-in” scan thus produces a film having counterions and solvent in place, and so on the return scan, the electrochemistry is more facile. Thus, for the solid curve, n-doping is observed at less negative potentials, while for the dashed curve, p-doping occurs at less positive potentials.

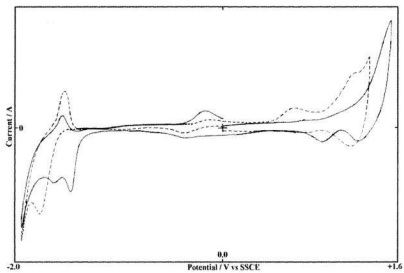


Figure 3.8: Cyclic voltammograms of two poly-btbtz coated electrodes in $\text{CH}_2\text{Cl}_2 / 0.1 \text{ M Bu}_4\text{NClO}_4$; positive scan first, —; negative scan first - - .

Table 3.5 presents the p-doping and n-doping potentials for the bithiazole-bithiophene copolymers of this project, as well as their bandgaps. Poly-**bmtbmtz** has a significantly lower bandgap than either poly-**btbtz** or poly-**btbmtz**, largely due to the stability of the p-doped form of this polymer. As can be seen, the n-doping potentials for all polymers do not differ greatly. Poly-**bmtbmtz** undergoes facile oxidation, starting at about 400 mV (see Appendix A). Cycling to higher potentials does not result in film degradation until about 1.2 V. At this potential, overoxidation of the backbone reduces conjugation in the film, significantly affecting the voltammogram. It is assumed that this occurs due to nucleophilic attack at the oxidized sites by trace impurities present in the solvent, electrolyte, or monomer. Oxidation of poly-**btbmtz** begins at about 0.9 V, while for poly-**btbtz**, p-doping is not seen until about 1.23 V.

Reduction of poly-**bmtbmtz** is observed at -1.71 V, lower than that for poly-**btbtz** and poly-**btbmtz**. For poly-**btbtz**, n-doping is seen at about -1.57 V, at about the same potential for poly-**btbmtz** (-1.52 V). Since the LUMO energies for **btbtz** and **btbmtz** are also not significantly different (section 3.4.1), it appears that the methyl substituents of the bithiazole core of **btbtz** and **bmtbmtz** do not significantly affect the LUMO energies of these monomers, or the LUMO band energies of their polymers.

	E° p-doping	E° n-doping	E_g (V)
poly- btbtz	+1.23	-1.57	2.80
poly- btbmtz	~+0.9	-1.52	~2.4
poly- bmtbmtz	+0.40	-1.71	2.11

Table 3.5: p-Doping and n-doping potentials for bithiazole-bithiophene copolymers, evaluated from the onset of oxidation and reduction currents for each polymer film.

Chapter 4
Characterization of
Transition Metal Complexes

4.1 Syntheses of 2,2'-bithiazole Complexes

Semiempirical calculations on 2,2'-bithiazole and 2,2'-bipyridine confirm that the former is a less electron-deficient system. This fact makes ligands incorporating 2,2'-bithiazole better candidates for electropolymerization. Unfortunately, this same fact makes them less susceptible to metal complexation, as they do not accept back-donated electron density as readily. Although heteroleptic complexes of ruthenium and osmium with bis(thienyl)bithiazoles were successfully prepared, attempts at making $\text{Ru}(\text{bibtz})_2^{2+}$ were unsuccessful. Endeavors to make complexes of iron, nickel, copper and cobalt were also undertaken, but only returned starting materials. Complexes of the less delocalized 2,2'-bithiazole could be prepared with ruthenium, copper, and cobalt, but not iron.

4.2 Metal Complexes for Electropolymerization

The metal complexes discussed here were synthesized in order to produce electropolymerizable monomers. Ruthenium and osmium were chosen to make complexes with the bis(thienyl)bithiazole ligands for reasons summarized in section 1.7. It was anticipated that polymers constructed from these materials would demonstrate fast electrochemistry and be electronically conductive over a greater potential window than for analogous redox metallopolymers.

Attempts to electropolymerize metal complexes of the series of ligands (**bibtz**, **bibtmtz**, **bmtbmtz**) in a variety of common solvent-electrolyte systems were invariably met with failure. It appeared that at the potentials necessary for ligand oxidation, a

competing process dominated, resulting in electrode passivation. Swager *et al.* circumvented this problem by extending their 2,2'-bipyridine-based ligand from four rings to six [53]. This modification, however, produced greater spacing between adjacent metal sites, probably reducing metal-metal communication. A copolymer of Ru(**mtbmtz**)(bpy)₂²⁺ and 2,2'-bithiophene was produced in our laboratory, but electron transport in the material, as measured by impedance spectroscopy, was low ($D_e = 10^{-10}$ cm²sec⁻¹) [81].

A primary goal of this project was to develop a metal-conjugated organic polymer hybrid material with enhanced electron transport properties relative to non-conjugated analogs. Metal-metal communication has been reported for metallopolymers in which coordination of the metal occurs directly to the polymer backbone, albeit across a shorter π -system than in the polymers presented here [62]. In order to synthesize a metallopolymer with only two thiophene spacer groups, boron trifluoride diethyletherate (BF₃OEt₂) was added to a CH₃CN/Et₄NClO₄ solution containing Os(**btbtz**)(bpy)₂²⁺. It was initially assumed that trace water (nucleophile) was present and deactivated the products of oxidation as they formed, coating the electrode with an electronically insulating film and precluding electropolymerization of the monomer complex. BF₃OEt₂ presumably complexes this water, allowing radical coupling to proceed. Even without added electrolyte, electropolymerization is observed in this solvent, at significantly lower potentials.

4.3 Characterization

Characterization of the metal complexes was conducted at two levels:

1. Identification was accomplished with analytical techniques (mass spectrometry, ^1H , ^{13}C NMR spectroscopy, and in one case, by X-ray crystallography).
2. Electronic and electrochemical characterizations were carried out with electronic absorption spectroscopy and cyclic voltammetry.

4.3.1 ESI-MS of M(L)(bpy)_2^{2+} Complexes

Electrospray ionization mass spectrometry provides a fast and convenient method for the identification of low valence ruthenium and osmium complexes [82-84]. Since these complexes are charged, they can be introduced into the mass spectrometer as ions in solution. This eliminates the need to ionize samples with "hard" methods (e.g. electron impact or other commonly used techniques), resulting in relatively simple mass spectra which are dominated by the molecular ion peak series. By supplying energy to break apart complexes, mass fragments can also be analysed by this technique. It was seen that as the fragmentation energy was increased, the number of ion species (fragments) produced similarly increased, resulting in fairly complex spectra.

Ruthenium and osmium each have several isotopes, the relative natural abundances of which are listed in Table 4.1. Although the existence of a multitude of isotopes leads to more complicated mass spectra, at the same time it provides evidence for the identification of isotopic clusters because fragments containing these metals take

the form of characteristic peak distributions. A simulation of one such molecular peak distribution is shown in Figure 4.1 for the Ru(**btbtz**)(bpy)₂²⁺ ion.

Although both perchlorate (ClO₄⁻) and hexafluorophosphate (PF₆⁻) complexes were synthesized during this project, it was preferable to study the latter, not only because of the danger with handling and heating perchlorates, but also since chlorine has more than one isotope ($M_{Cl} = 34.968852, 75.77\%; 36.965903, 24.23\%$) [85].

Mass spectra for the all complexes studied showed significant M/z ($z = 2+$) peak series (with successive peaks separated by $\frac{1}{2}$ mass units) when a comparatively low fragmentation energy (100 V) was supplied. The series of metal complexes studied contain common fragments (e.g. the Ru(bpy)₂²⁺ fragment is present in several complexes) so it is to be expected that as fragmentation energy is supplied (the fragmentation energy could be varied in these experiments), similar fragmentation patterns should be observed. The Ru(bpy)₂⁺ ion was observed for all ruthenium complexes for fragmentation energies 150 V and higher, at $M/1+ = 414$.

Element	Atomic Mass	Natural Abundance (%)
⁹⁶ Ru	95.907556	5.54(2)
⁹⁸ Ru	97.905287	1.86(2)
⁹⁹ Ru	98.905939	12.7(1)
¹⁰⁰ Ru	99.904219	12.6(1)
¹⁰¹ Ru	100.905582	17.1(1)
¹⁰² Ru	101.904348	31.6(2)
¹⁰⁴ Ru	103.905424	18.6(2)
¹⁸⁴ Os	183.952488	0.02
¹⁸⁶ Os	185.953830	1.58(10)
¹⁸⁷ Os	186.955741	1.6(1)
¹⁸⁸ Os	187.955860	13.3(2)
¹⁸⁹ Os	188.958137	16.1(3)
¹⁹⁰ Os	189.958436	26.4(4)
¹⁹² Os	191.961467	41.0

Table 4.1: Isotopic distributions of ruthenium and osmium at natural abundance [85].

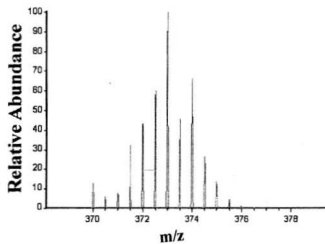


Figure 4.1: Simulation of the molecular peak distribution for $\text{Ru}(\text{btbtz})(\text{bpy})_2^{2+}$ ion.

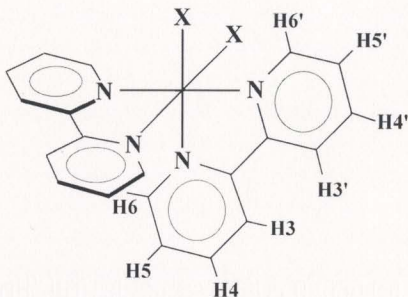


Figure 4.2: C_2 symmetry of the bis(2,2'-bipyridine) ruthenium and osmium complexes of the bithiazole ligands leads to splitting of the 2,2'-bipyridine resonances.

4.3.2 ^1H NMR Spectra of $\text{M}(\text{L})(\text{bpy})_2^{2+}$ Complexes

The ^1H NMR spectra for the $\text{M}(\text{L})(\text{bpy})_2^{2+}$ complexes studied here are interesting.

Several groups have reported on the changes in the spectra of pyridine systems upon metal complexation [86, 87]. Upon coordination to a metal center to form the $\text{M}(\text{bpy})_2^{2+}$ complex described in Figure 4.2, the hydrogens marked H3 and H3' experience increased van der Waals repulsion as they are forced closer together, resulting in a deshielding effect for these hydrogens relative to an uncomplexed 2,2'-bipyridine molecule. H6 and

H6', on the other hand, experience increased shielding from the neighboring ring current of the adjacent 2,2'-bipyridine (diamagnetic anisotropic effect). Figure 4.3 illustrates the ^1H NMR spectra for the ruthenium and osmium *tris* complexes, as well as for uncomplexed 2,2'-bipyridine.

Figure 4.4 shows that for such a complex, if $L \neq 2,2'$ -bipyridine, complex splitting patterns can emerge due to the differing chemical environments between each ring of a bipyridine ligand, imposed by C_2 symmetry. For $L = \text{bmtz}$, there are two sets of bipyridine signals. Note in Figure 4.2 that H6 in this complex will be adjacent to a bipyridine system, while H6' will neighbor the bithiazole ligand. For this particular complex, the split into separate signals is easily followed. Assignment of individual peak identities requires more information.

A COSY experiment can reveal which hydrogens are spin-spin coupled. One such experiment was conducted on $\text{Ru}(\text{bmtz})(\text{bpy})_2(\text{ClO}_4)_2$ (Figure 4.5), revealing more completely the peak relationships in one of the simpler $\text{M}(\text{L})(\text{bpy})_2^{2+}$ spectra. In these experiments, the sample tube is subjected to a radio frequency (RF) pulse of a specific frequency, bringing a specific proton into resonance. The free induction decay, obtained from the non-specific excitation pulse is then measured. The obtained spin-coupled signals must be due to hydrogens on the same bipyridine ring, since spin-coupling only occurs through bonds. The output for this experiment is displayed in a two dimensional map. The diagonal of this spectrum corresponds to the one dimensional output for this complex detailed in Figure 4.4 (bottom, also shown on the top and left axes of the COSY

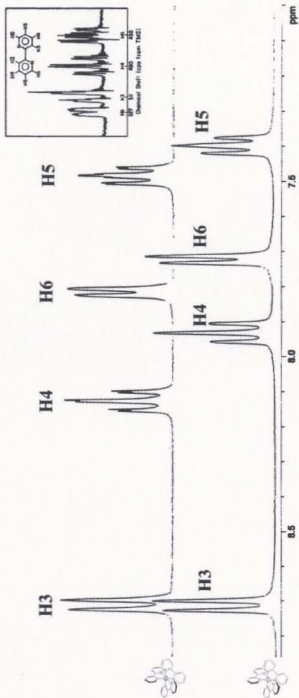


Figure 4.3: ¹H NMR (300 MHz) in CD₃OD for Os(bpy)₃²⁺ (bottom) and Ru(bpy)₃²⁺ (top). Inset: ¹H NMR for 2,2'-bipyridine in DMSO-d₆ [87]. Reprinted with permission from *Anal. Chim. Acta* 1971, 57, 240. Copyright 1971, Elsevier Science.

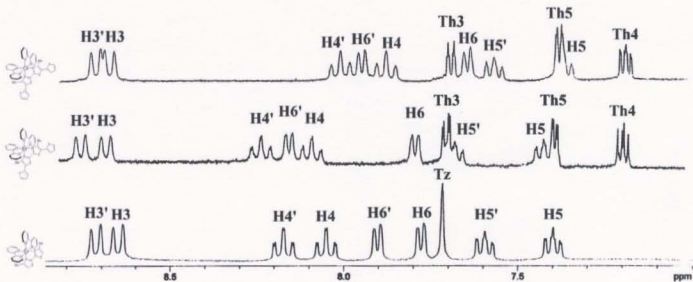
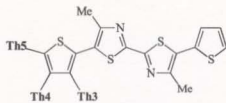


Figure 4.4: ^1H NMR (300 MHz) in CD_3OD for (bottom to top): $\text{Ru}(\text{bmtz})(\text{bpy})_2^{2+}$, $\text{Ru}(\text{btbtz})(\text{bpy})_2^{2+}$, and $\text{Os}(\text{btbtz})(\text{bpy})_2^{2+}$.

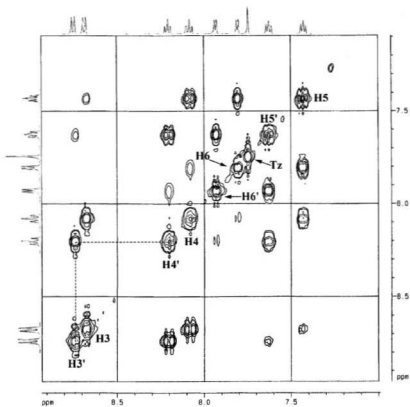


Figure 4.5: COSY spectrum of $\text{Ru}(\text{bmtz})(\text{bpy})_2^{2+}$ in CD_3OD . COSY data permits hydrogens of each ring on a bipyridine ligand to be differentiated. One dimensional representation is shown on top and left axes.

spectrum). Off-diagonal signals represent spin-coupled protons. To establish which protons participate in this coupling, horizontal and vertical lines are drawn from this signal to the diagonal. The example shown in the figure establishes that the signals denoted H3 and H4 are spin-coupled, and thus are on the same ring. Similarly, it can be shown that the signals labeled H5 and H6 also must be caused by hydrogens of this ring.

The assignment of H3' rather than H3 to the first peak of this spectrum was made after comparing the relative chemical shifts for each set of proton signals against those for the *tris* complex. The H3', H4', H5', and H6' signals showed better agreement with Ru(bpy)₃²⁺ shifts, implying that these hydrogens are probably affected by the π-cloud of an adjacent bipyridine. Further support for this argument is seen by the relatively large shift observed for the H6 signals of Ru(**btbmtz**)(bpy)₂²⁺ and Os(**btbmtz**)(bpy)₂²⁺ compared to Ru(**bmtz**)(bpy)₂²⁺. This hydrogen would be most affected by a change in the structure of the bithiazole ligand. However, the second point is based on the assumption that the peak assignments for the Ru(**bmtz**)(bpy)₂²⁺ complex extrapolate to the bis(2-thienyl)dimethylbithiazole complexes (see Figure 4.4).

The introduction of a thiophene ring complicates the spectra. Three thiophene signals are present instead of the thiazole (**Tz**) peak, in addition to the bipyridine signals. These signals are all shifted downfield relative to the corresponding signals for the free monomer (**btbmtz**). This behavior was also reported for bipyridine signals when complexed to Fe, Ru, and Os centers, and it is believed to be a consequence of coordination to the dipositive metal cations [87]. A comparison between

$\text{Ru}(\text{btbmtz})(\text{bpy})_2^{2+}$ and $\text{Os}(\text{btbmtz})(\text{bpy})_2^{2+}$ shows that all signals exhibit an upfield shift for the larger metal center, although this shift is small for the thiophene signals. This trend holds for $\text{Os}(\text{bpy})_3^{2+}$ and $\text{Ru}(\text{bpy})_3^{2+}$, and is likely a consequence of increased metal-to-ligand back bonding [86].

4.3.3 Crystal Structure for $\text{Ru}(\text{btbmtz})(\text{bpy})_2(\text{PF}_6)_2$

For the ruthenium (II) complexes synthesized as part of this project, it was found that several mixed solvent systems were effective for the crystallization of hexafluorophosphate and perchlorate salts of the bithiazole complexes. Sargeson *et al.* [74] reported a slow addition of diethyl ether to a rapidly stirred methanol solution of $[\text{Os}(\text{bpy})_2\text{Cl}_2]\text{Cl}$ yielded microcrystals. Slow evaporation of either acetone or acetonitrile, however, from either water or toluene was found to result in needle-like crystals of $\text{Ru}(\text{btbmtz})(\text{bpy})_2(\text{PF}_6)_2$. Crystals obtained from acetone-water were found to be suitable for X-ray analysis. Although the same system produced similar crystals for $\text{Ru}(\text{btbtz})(\text{bpy})_2(\text{PF}_6)_2$, these were found to decompose during irradiation with X-rays. Large crystals were also produced for $\text{Ru}(\text{btz})_3(\text{PF}_6)_2$ and $\text{Ru}(\text{btz})(\text{bpy})_2(\text{PF}_6)_2$, but were not analysed.

The ORTEP structure shown in Figure 4.6 confirms the predicted structure for this metal complex. The geometry is approximately octahedral about the ruthenium center, with the bipyridine rings positioned in a manner which would result in the discussed ^1H NMR splitting. The thiophene rings of **btbmtz** are twisted when complexed

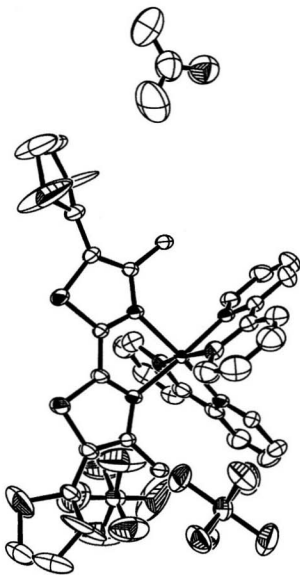


Figure 4.6. X-ray crystal structure for Ru(bibmtz)(bpy)₂(PF₆)₃ crystals grown from acetone-H₂O.

to Ru(bpy)₂. Furthermore, the two hexafluorophosphate ions confirm the Ru²⁺ oxidation state. A coordinated acetone molecule completes the unit cell.

The shape of a thermal ellipsoid in the ORTEP is an indicator of the uncertainty for a given atom's position. The oblong shape of the ellipsoids for the thiophene rings suggest that ring twisting will yield one of two possible orientations (positive or negative twist) for a thienyl group in this complex.

4.4 Electronic and Electrochemical Characterization

Electronic absorption spectroscopy and cyclic voltammetry can be employed to gain an understanding the nature of the metal-ligand coordination in these complexes. As was the case for the uncomplexed ligands, UV-Vis experiments are useful for studying π - π^* transitions. Cyclic voltammetry provides estimates of both HOMO and LUMO energies, not just their difference (i.e., the bandgap). MLCT energies can also be estimated, by the difference between the M^{3+/2+} formal potential and the formal potential for reduction of the bithiazole ligand.

4.4.1 Electronic Absorption Spectroscopy

Metal coordination to 2,2'-bithiazole involves σ donation from the ligand to the metal, and back-donation from the metal's t_{2g} orbitals to the ligand's π^* orbital. Consequently, the absorption spectra for these complexes are dominated by three peaks. The lowest intensity, longest wavelength peak is attributable to metal back-donation (metal to ligand

charge transfer, MLCT), while the other peaks are caused by intraligand π - π^* transitions in the bithiazole ligand (middle peak) and the ancillary bipyridine moieties (highest energy peak). The electronic absorption spectrum for **btbtz**, as well as its complexes with $\text{Ru}(\text{bpy})_2^{2+}$ and $\text{Os}(\text{bpy})_2^{2+}$ are shown in Figure 4.7. It is apparent from this comparison that coordination to a metal center affects the energy of the frontier orbitals of the bithiazole ligand, as the energy of the π - π^* transition (the ligand's energy bandgap) is red shifted by 28 nm in the ruthenium(II) complex and 34 nm in the osmium(II) complex. This peak is broader for $\text{Os}(\text{btbtz})(\text{bpy})_2^{2+}$ than for $\text{Ru}(\text{btbtz})(\text{bpy})_2^{2+}$, resolving into two shoulders (420 nm and 435 nm). This "shoulder" appearance has been reported for several osmium(II) complexes [88].

Introduction of the metal center has the effect of lowering both the HOMO and LUMO energies, making the bithiazole ligand more difficult to oxidize, while at the same time, facilitating its reduction. This behavior is analogous to that observed for diprotonation (section 3.2.3). Correspondingly, ligand π - π^* transition energies are found to decrease moderately from those for the uncoordinated ligands. Peak wavelengths (λ_{max}) for ligand and MLCT absorptions for the complexes studied are shown in Table 4.2. It can be seen from this data that MLCT absorptions for the osmium complexes are at lower energy than their ruthenium analogues, consistent with the higher energy d-electrons in descending a group in the periodic table.

The absorption spectra of $\text{Ru}(\text{btz})_3^{2+}$, $\text{Ru}(\text{btz})(\text{bpy})_2^{2+}$, and $\text{Ru}(\text{bmtz})(\text{bpy})_2^{2+}$ are more complicated than the spectra of the four ring metal complexes, having shoulders on

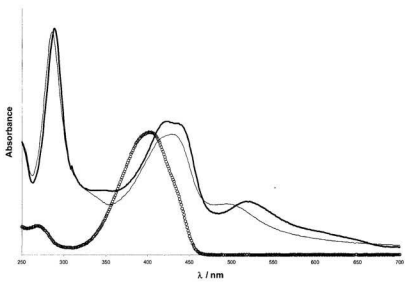


Figure 4.7: Electronic absorption spectra for **btbz** (o), $\text{Ru}(\text{btbz})(\text{bpy})_2^{2+}$ (thin line), and $\text{Os}(\text{btbz})(\text{bpy})_2^{2+}$ (thick line)

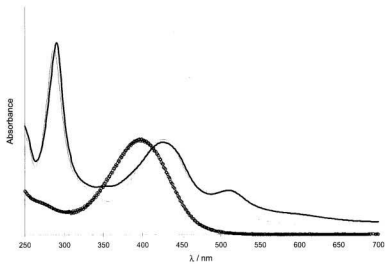


Figure 4.8: Electronic absorption spectra of $M(L)(bpy)_2^{2+}$ complexes in methanol. **btbtz** (o); **Ru(btbtz)(bpy)₂²⁺** (thin line); **Os(btbtz)(bpy)₂²⁺** (thick line).

	$\lambda_{\text{max(L)}}$	$\lambda_{\text{max(MLCT)}}$
Ru(bpy) ₃ ²⁺	287	414, 450
Ru(btzt) ₃ ²⁺	325	441, 473
Ru(btzt)(bpy) ₂ ²⁺	325	427, 457
Ru(bmtz)(bpy) ₂ ²⁺	343	424, 453
Ru(btbtz)(bpy) ₂ ²⁺	429	495
Ru(btbtmtz)(bpy) ₂ ²⁺	423	480 ^a
Os(bpy) ₃ ²⁺	289	435, 478
Os(btbtz)(bpy) ₂ ²⁺	420, 435	512
Os(btbtmtz)(bpy) ₂ ²⁺	430	485
Os(bmtbtmtz)(bpy) ₂ ²⁺	457	^b

Table 4.2: Electronic absorption data for metal complexes in MeOH.

a: the MLCT absorption for Ru(btbtmtz)(bpy)₂²⁺ was partially obscured by the π - π^* absorption of the btbtmtz ligand (see Figure 4.7).

b: the MLCT absorption peak for Os(bmtbtmtz)(bpy)₂²⁺ was almost completely obscured by the π - π^* absorption (see Appendix D).

the π - π^* and MLCT peaks (see Appendix D). While the spectra for Ru(**btz**)(bpy)₂²⁺ and Ru(**bmtz**)(bpy)₂²⁺ look nearly identical, the π - π^* absorption peak occurs about 18 nm higher in the latter. For the analogous bis(thienyl)bithiazole complexes, the shift is in the opposite direction. Crystal data for Ru(**btbmtz**)(bpy)₂(PF₆)₂ shows that the thiophene rings of this complex are twisted out of plane, reducing the delocalization in the bithiazole ligand and resulting in a higher energy π - π^* transition. The addition of methyl substituents to Ru(**btz**)(bpy)₂²⁺ and Ru(**btbztz**)(bpy)₂²⁺ makes back donation less favorable, as indicated by shifts to higher energy MLCT energies (Figure 4.8).

4.4.2 Cyclic Voltammetry of M(L)(bpy)₂²⁺ Complexes

Cyclic voltammetry of ruthenium and osmium complexes of the bithiazole ligands produced redox behavior similar to that of well-studied Ru(bpy)₃²⁺ [89]. Four reversible one-electron waves are observed for this system, one for a Ru^{3+/2+} process, and the other three corresponding to bipyridine ligand-based reductions. Scanning to lower potentials (*ca.* -2.4 V) is reported to result in irreversible decomposition of the complex [89]. For ruthenium complexes incorporating bis(thienyl)bithiazole ligands, an additional oxidation wave is seen, corresponding to irreversible oxidation of a thiophene ring of the ligand (which normally leads to radical coupling reactions and polymerization).

Ru(**btbztz**)(bpy)₂²⁺ exemplifies this redox behavior (Figure 4.9). An easily distinguishable Ru^{3+/2+} wave is seen at about 1.24 V, about 40 mV less positive than for Ru(bpy)₃²⁺; it is to be expected that this Ru^{3+/2+} process will occur at a lower potential when coordinated

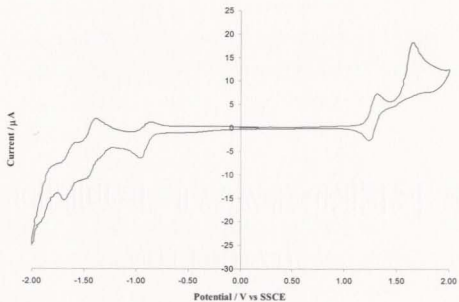


Figure 4.9: Cyclic voltammogram of ca. 5.5 mM $\text{Ru}(\text{btbtz})(\text{bpy})_2^{2+}$ in $\text{CH}_3\text{CN}/\text{Et}_4\text{NClO}_4$

($\nu = 100 \text{ mV sec}^{-1}$, $A = 0.0052 \text{ cm}^2$).

to the more delocalized **btbtz**.

There is a substantial shift of the ligand oxidation peak upon complexation of **btbtz** with $\text{Ru}(\text{bpy})_2^{2+}$ (to 1.58 V from 1.36 V for free **btbtz**) and an even greater shift in reduction waves (-0.88 V for $\text{Ru}(\text{btbtz})(\text{bpy})_2^{2+}$ vs -1.65 V for metal-free **btbtz**). This clearly shows that coordination to the ruthenium center has a dramatic effect on the electronic structure of the ligand, as was shown by electronic absorption experiments (Section 4.4.1). It is seen in Table 4.3, that the energy gap (the difference between the ligand oxidation peak and the ligand reduction half-wave potential) is significantly lower than that found in the uncomplexed ligand (3.01 eV, Table 3.4), a consequence of donor-acceptor behavior in the complexes.

An explanation for the position of the ruthenium and osmium III/II waves in the complexes of the bis(thienyl)bithiazole ligands is not straightforward. It would be expected that the methyl groups of **btbtz** would result in lower $\text{M}^{3+/2+}$ potentials when compared with complexes incorporating **btbtz**. The inductive stabilizing effect of these substituents may be offset, however, by geometric strain caused by their proximity to the bipyridine rings in the complex, as mentioned in section 4.4.1. This would lead to a less planar **btbtz**, and a lower HOMO energy. Thus, electron donation to the metal would be diminished. The methoxy substituents in $\text{Ru}(\text{bmtbmtz})(\text{bpy})_2^{2+}$ do not cause increased steric crowding relative to **btbtz**, and so resonance stabilization can affect the $\text{M}^{3+/2+}$ process for this complex (+1.17 V). The position of the $\text{Os}^{3+/2+}$ wave appears to be fairly independent of the ligand to which it is coordinated.

	L_{Ox}	M^{III}	L_{Red}	bpy	bpy	bpy	E_g / eV^a
Ru(bpy) ₃ ²⁺		1.27		-1.31	-1.51	-1.73	
Ru(btz) ₃ ²⁺		1.33	-1.04		-1.23 ^b	-1.44 ^b	
Ru(btz)(bpy) ₂ ²⁺		1.25	-1.15		-1.55	-1.79	
Ru(btbtz)(bpy) ₂ ²⁺	1.58	1.24	-0.88		-1.43	-1.64	2.46
Ru(btbtmtz)(bpy) ₂ ²⁺	1.60	1.29	-0.97		-1.47	-1.64	2.55
Ru(bmtbtmtz)(bpy) ₂ ²⁺	1.64	1.17	-1.05		-1.47	-1.71	2.69
Os(bpy) ₃ ^{2+ c}		0.82		-1.26	-1.45	-1.76	
Os(btbtz)(bpy) ₂ ²⁺	1.65	0.84	-0.89		-1.31	-1.63	2.54
Os(btbtmtz)(bpy) ₂ ²⁺	1.69	0.86	-0.92		-1.35	-1.60	2.61
Os(bmtbtmtz)(bpy) ₂ ²⁺		0.85	-1.04		-1.42	-1.70	

Table 4.3: Redox potentials (V vs SSCE) for metal complexes in CH₃CN/Et₄NClO₄ vs SSCE. Eg = difference between L_{Ox} and L_{Red} .

a: from the difference of ligand oxidation and reduction potentials

b: 2,2'-bithiazole based reductions

c: from ref. [90]

The positions of the reduction waves for the bithiazole ligands in these complexes appear to follow a more predictable pattern. Comparing ruthenium complexes of **btbtz** and **bmtbmtz**, it is seen that a lower potential is needed to reduce the latter, similar to what is found for these ligands when not forming part of a complex. The same behavior is found in the osmium(II) complexes. Because the potentials for this reduction are so similar between both complexes, it seems that the nature of the metal center has little influence on this process.

The first reduction wave for $\text{Ru}(\text{btbtz})(\text{bpy})_2^{2+}$ is assigned to reduction of the four ring ligand because the first reduction wave for $\text{Ru}(\text{btz})_3^{2+}$ occurs at -1.04 V, while this wave is not seen until -1.31 V for $\text{Ru}(\text{bpy})_3^{2+}$. The other two waves, due to reduction of the the bipyridine segments, are excellent markers for gauging a ligand's influence on the electronic structure of the complex. The bipyridine-centered reductions in $\text{Ru}(\text{btbtz})(\text{bpy})_2^{2+}$ do not occur until -1.43 V and -1.64 V, while in $\text{Ru}(\text{bpy})_3^{2+}$, these reductions take place at -1.51 V and -1.73 V (Figure 4.10). There is a noticeable trend in the redox potentials for the bipyridine-based processes of the ruthenium bis(2-thienyl)bithiazole complexes. It was found that these processes occurred at lower potentials as electron donating functions were added to the **btbtz** ligand (**btbtz**, **btbmtz**, **bmtbmtz**), since for these complexes, less electron density is back-donated to the bithiazole system while more is delocalized onto the bipyridine ligands.

The higher energy d-orbitals of osmium are a better match for the bipyridine π^* -orbital energies than ruthenium, as indicated by less negative potentials to observe their reduction (see Figure 4.11).

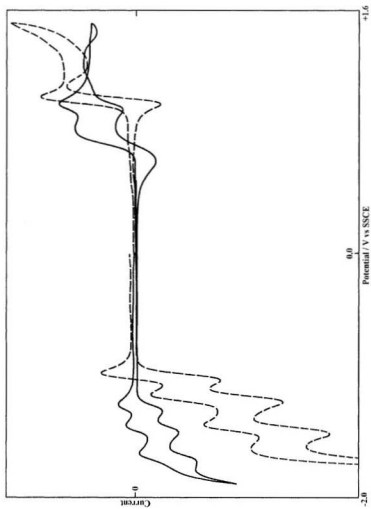


Figure 4.10: Cyclic voltammogram of $\text{Ru}(\text{bpy})_3\text{Cl}_3$ (—) and $\text{Ru}(\text{btz})_3(\text{PF}_6)_3$ (---) in CH_3CN / 0.1 M Et_4NClO_4 ($\nu = 100 \text{ mV sec}^{-1}$).

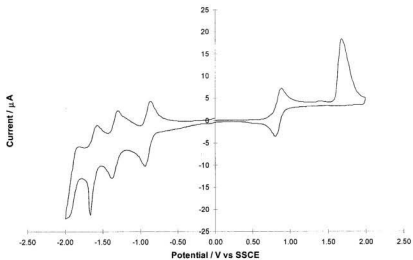


Figure 4.11: Cyclic voltammogram of *ca.* 5.5 mM Os(btbtz)(bpy)₂²⁺ in CH₃CN/0.1 M Et₄NClO₄ ($\nu = 100$ mVsec⁻¹). $A = 0.0052$ cm².

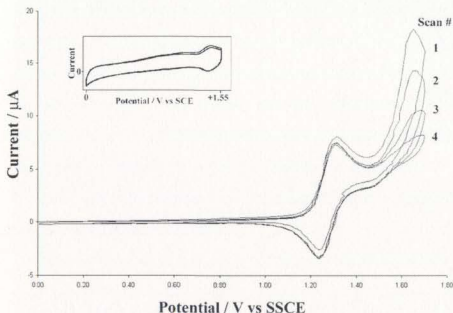


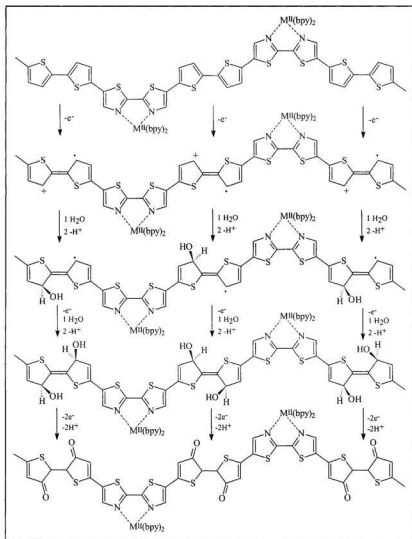
Figure 4.12: Attempted electropolymerization of *ca* 5.5 mM $\text{Ru}(\text{btbtz})(\text{bpy})_2^{2+}$ in $\text{CH}_3\text{CN}/0.1 \text{ M Et}_4\text{NClO}_4$ ($v = 100 \text{ mV sec}^{-1}$). $A = 0.0052 \text{ cm}^2$. Inset: electrochemistry of a Pt electrode after potential cycling in $\text{Ru}(\text{btbtz})(\text{bpy})_2^{2+}$ solution.

4.5 Electropolymerization of $\text{M}(\text{L})(\text{bpy})_2^{2+}$ Complexes

Potential cycling through the ligand oxidation peak should permit polymer film formation in a manner analogous to the mechanism previously described for bithiazole monomers (Section 3.5.2). Unfortunately, recurrent potential scanning in common solvent-electrolyte systems failed to produce sustained polymerization. In order to electropolymerize these metal complexes, it was necessary to either add boron trifluoride diethyletherate ($\text{BF}_3 \text{ OEt}_2$) to a solvent-electrolyte system, or to electropolymerize the

monomer complex in this medium alone. Figure 4.12 demonstrates the failure of $\text{Ru}(\text{btbtz})(\text{bpy})_2^{2+}$ to electropolymerize in $\text{CH}_3\text{CN}/0.1 \text{ M Et}_4\text{NClO}_4$. Subsequent scans exhibit current decreases, implying that something occurs which prevents the formation of a conductive coating. Although faint films were visible on electrodes used in these experiments, testing in $\text{CH}_3\text{CN}/\text{Et}_4\text{NClO}_4$ showed only a small, isolated ruthenium(III/II) wave. It was reasoned that electrode passivation took place, a consequence of nucleophilic attack by trace water (or some other nucleophile) on the oxidized species involved in radical coupling (Scheme 4.1).

Electropolymerizations conducted in BF_3OEt_2 have been reported to produce high strength polymer films, even for normally non-electropolymerizable compounds [91-93]. The addition of this solvent to a $\text{CH}_3\text{CN}/\text{Et}_4\text{NClO}_4$ solution of $\text{Os}(\text{btbtz})(\text{bpy})_2^{2+}$ enabled anodic polymerization, yielding dark metallopolymer films (Figure 4.13). Current gains were seen for the $\text{Os}^{3+/2+}$ process with each cycle, although the expected increases for the ligand oxidation peak were not observed. The lack of current gains attributable to oxidation of a polymerizable segment is not new. It has also been reported during the electropolymerization of a pyrrole-substituted metal complex [94]. As potential cycling continues, new waves begin to appear in the region between the potential for ligand oxidation and the metal wave. Although the appearance of these waves is expected, due to oxidation of chains of increasing conjugation lengths, their direction moves toward higher potentials with successive cycles. The polymerization should produce an opposite



Scheme 4.1: Deactivation of the poly-btbtz backbone by nucleophilic attack by trace H_2O results in a breakdown of the long-range π -conjugation.

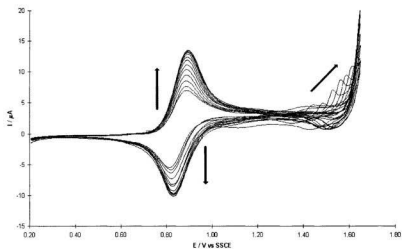


Figure 4.13: Polymerization of ca. 5.1 mM $\text{Os}(\text{btbtz})(\text{bpy})_2^{2+}$ in $\text{CH}_3\text{CN} / (0.1 \text{ M}) \text{Et}_4\text{NClO}_4$ with 0.45 M BF_3OEt_2 ($v = 100 \text{ mV sec}^{-1}$). $A=0.0052 \text{ cm}^2$. Arrows show changes with increasing cycle number.

migration for these new waves, suggesting that the film formed on the electrode underwent loss of conjugation with each cycle.

The polymerization of $\text{Ru}(\text{btbtz})(\text{bpy})_2^{2+}$ in neat BF_3OEt_2 is shown in Figure 4.14. From a comparison with Figure 4.11, it is evident that facile polymerization of the monomer complex occurs at a lower potential in BF_3OEt_2 , by about 200 mV. Furthermore, current increases for the ligand oxidation wave are observed in subsequent cycles, although these gains are not as great as those for the $\text{Ru}^{3+/2+}$ process. The metal wave peak separation increases as cycling is continued, the greater current and less broad shape of the cathodic portion of this wave being indicative of film formation. The prewave at ca. 0.8 V is commonly reported for redox polymer systems, and has been attributed to trapping of some species in processes associated with the reduction and reoxidation of a film [53,61].

The voltammetry for the polymerization of $\text{Os}(\text{btbtz})(\text{bpy})_2^{2+}$ in BF_3OEt_2 (Figure 4.15) shares some features with Figure 4.14. Polymerization is indicated by current gains with scanning (again more so at the metal wave potential than at the ligand peak potential). Similar to the voltammogram for $\text{Os}(\text{btbtz})(\text{bpy})_2^{2+}$ in $\text{CH}_3\text{CN}/\text{BF}_3\text{OEt}_2/\text{Et}_4\text{NClO}_4$, new waves appear just beyond the $\text{Os}^{3+/2+}$ wave and these waves are pushed to higher potentials on subsequent cycles (although this time, the migration appears to be more regular). On the fourth cycle, a new cathodic prewave begins, its position migrating to lower potentials with each scan. Unlike for $\text{Ru}(\text{btbtz})(\text{bpy})_2^{2+}$, the positions of the osmium peaks appear to be fairly constant.

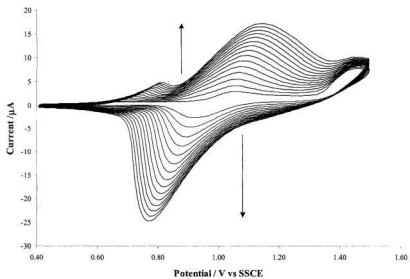


Figure 4.14: Electropolymerization of 5 mM $\text{Ru}(\text{btbtz})(\text{bpy})_2^{2+}$ in neat BF_3OEt_2 ($\nu = 100 \text{ mV sec}^{-1}$).

$A=0.0052 \text{ cm}^2$. Arrows indicate current growth with cycle number.

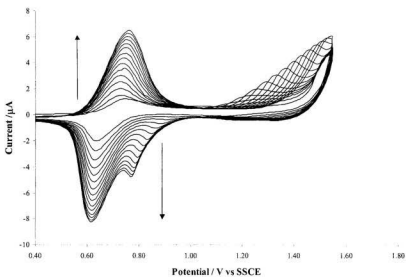


Figure 4.15: Electropolymerization of ca 2.7 mM $\text{Os}(\text{btbtz})(\text{bpy})_2^{2+}$ in neat BF_3OEt_2 ($v = 100 \text{ mV sec}^{-1}$).

$A=0.0052 \text{ cm}^2$.

In order to establish that electropolymerization of these complexes occurs in a manner analogous to the mechanism proposed for acetonitrile solutions (i.e., through the thiophene substituents) $\text{Ru}(\mathbf{btz})(\text{bpy})_2^{2+}$ and $\text{Ru}(\mathbf{bmtz})(\text{bpy})_2^{2+}$ were tested in the same neat solvent, resulting in no film formation.

The cyclic voltammograms showing the electropolymerization of $\text{Ru}(\mathbf{btbtz})(\text{bpy})_2^{2+}$ and $\text{Ru}(\mathbf{btbmtz})(\text{bpy})_2^{2+}$ are identical, as are the voltammograms for the analogous osmium complexes in neat BF_3OEt_2 . This similarity translates into the electrochemistry of the corresponding metallopolymer films, as will be seen later.

It was not possible to electropolymerize $\text{Ru}(\mathbf{bmtbmtz})(\text{bpy})_2^{2+}$ in BF_3OEt_2 . Potential cycling of this monomer produced behavior similar to what was noted above for $\text{Ru}(\mathbf{btz})(\text{bpy})_2^{2+}$ and $\text{Ru}(\mathbf{bmtz})(\text{bpy})_2^{2+}$ in this medium. This is perhaps due to complexation of the methoxy oxygen atoms of $\mathbf{bmtbmtz}$ by BF_3 . Such an adduct is represented in Figure 4.16. It is likely in this situation that the partially vacant π -orbital of boron draws electron density away from the metal complex [95]. This would lower the stability of the oxidized intermediate formed during potential cycling, and inhibit radical coupling necessary for polymer film formation to occur.

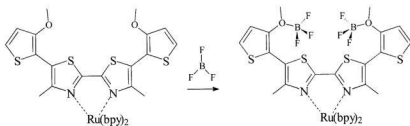


Figure 4.15: Complexation by $\text{BF}_3\cdot\text{OEt}_2$ produces an adduct with less net electron density on the polymerizable bithiazole ligand. Oxidation of this complex produces a less stable intermediate, preventing radical coupling.

Chapter 5

Electrochemistry and Electron Transport Studies of Conjugated Metallopolymers

5.1 Conjugated Metallopolymer Films

This chapter deals with electronic and electrochemical studies on electrodes coated with conjugated metallopolymer films. This section presents an important focus of the project: to demonstrate the contribution of the conjugated π -orbital network to electron transport through these systems (i.e., in which metal coordination is to the π -conjugated backbone, by direct d_M - π_L orbital overlap). Electrochemical Impedance Spectroscopy (EIS) was the technique chosen for these investigations in lieu of other, more commonly reported methods, for reasons described later. Comparisons with other metallopolymers provide evidence of enhanced transport rates and insight on preferred superexchange pathways. The next and final chapter follows up with a summary of the major findings of this work and suggests some directions for the future of the project.

5.2 Electrochemical Studies on Metallopolymer Films

The synthesis of ready-to-study conjugated metallopolymer films of bithiazole metal complexes was described in Section 4.5; however, for the experiments discussed here, it is worth noting that some metallopolymer films were not grown *via* potential cycling, but were instead deposited by potentiostatic (controlled potential) or galvanostatic (controlled current) methods. Analyses of the metallopolymer-coated electrodes were performed in monomer-free solutions of Et_4NClO_4 in CH_3CN . All experiments employed an SSCE reference unless otherwise noted, and a scan speed of 100 mV sec^{-1} .

The electrochemistry of each metallopolymer film was examined at both positive (oxidizing) and negative (reducing) potentials. Typically, films were scanned to potentials high enough to observe the electrochemistry of the coordinated metal centers. In most cases, the electrochemistry of the conjugated backbone could also be observed. The reductive electrochemistry was explored first at moderately low potentials, progressing to lower potentials. In this manner, stable electrochemistry over a limited potential window could be observed for some metallopolymers.

Figure 5.1 contrasts the anodic electrochemistry of poly-**btbmtz** and the metallopolymer poly-[Ru(**btbmtz**)(bpy)₂^{3+/2+}] formed under potential cycling control. The comparison demonstrates an obvious change in the electronic structure of the polymer upon coordination of the bis(bipyridyl)ruthenium(II) center. Most notably, the oxidation peak for the polymer backbone is pushed to higher potentials, by about 0.3 V (also evident is the Ru^{3+/2+} wave near 1.3 V). This is expected, as the electron-poor metal cation should lower the HOMO band energy of poly-**btbmtz**, similar to the effect observed for protonation of the polymer (section 3.4). The electrochemistry of the uncoordinated polymer film is also somewhat broader, particularly for the second wave. In contrast, the metallopolymer backbone exhibits more symmetric voltammetry, confined over a smaller potential window (first scan).

This behavior was noted for the bithiophene-bithiazole copolymer reported by Wolf and Wrighton [37] when coordinated to a rhenium center. They postulated a fluctuating valence band model (section 1.6.1), with lower valence energy periods

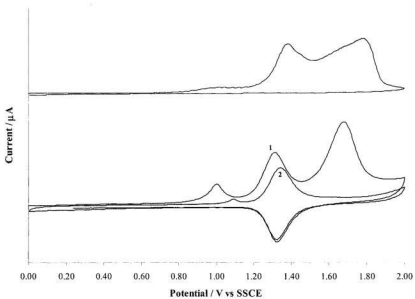


Figure 5.1: Qualitative comparison of the cyclic voltammograms of poly-btbmtz (top) and poly-[Ru(btbmtz)(bpy)₃³⁺²⁺] (bottom). Scan numbers indicated.

coincident with bithiazole segments in the bithiazole-bithiophene copolymer.

Coordination of a metal cation should pronounce this effect, lowering the band energy even more at these positions. This leads to a poorer matching of orbital energies between thiazole and thiophene, resulting in hole localization in the bithiophene regions, and electron localization on bithiazole units.

Further to this, it is well known that the potentials required to polymerize thiophenes lead to degradation of the product as it is forming [96]. This phenomenon has been coined “the polythiophene paradox” and, although it appears that oxidation of the bithiazole complexes in BF_3OEt_2 is advantageous in that it occurs at a potential nearly 200 mV lower than in $\text{CH}_3\text{CN} / 0.1\text{M Et}_4\text{NClO}_4$, it is possible that this potential is still high enough that it effects overoxidation of the forming metallopolymer backbone. This would contribute to the less broadened appearance of the metallopolymer voltammogram.

Similar to what has been described for the cyclic voltammetry of the monomer complexes, the electrochemistry of the metal center can be seen to dominate the voltammetry of the films (e.g. Figure 5.2). Slightly broader bipyridine-based electrochemistry is observed for the polymer complexes, and these are shifted to more negative potentials, indicating a lower tendency to their reduction than for the parent monomer complexes.

The electrochemistry of poly-[Ru(**btbtz**)(bpy)₂^{3+/2+}] is shown in Figure 5.2. The figure is a composite of two series of scans. As described in Section 3.5.3, the voltammetry observed for a polymer film is affected by the film’s history. The anodic

and cathodic halves of this figure were obtained in separate experiments, and so features like counterion uptake/release appear to be largely absent. The electrochemical processes observed for this metallopolymer are labelled in the figure (top). The anodic electrochemistry shows a single M^{III} process at about $E_{1/2} = +1.37$ V. It was possible to observe the electrochemistry of the backbone for this polymer at higher potentials (peak at *ca.* +1.77 V), but this wave disappeared after only one scan (100 mV sec^{-1}). The lack of polymer electrochemistry on the second scan suggests nucleophilic attack on the oxidized backbone by a trace amount of some species in the solvent/electrolyte system, yielding electrochemical deactivation. The Ru^{III} wave is still present, but shifted to higher potentials (by about 30 mV).

The cathodic electrochemistry for poly-[Ru(**btbtz**)(bpy)₂^{3+/2+}] was studied over several potential windows. The first six scans show the electrochemistry between 0 V and -0.9 V. A clear redox wave is seen centered at -0.86 V which showed a slight current drop after each scan. The next potential limits (-1.2 V and -1.5 V) were chosen to probe the reduction of the metallopolymer at moderately low potentials. After the scan to -1.5 V, a significant current drop was observed for the -0.86 V wave. The low potentials required to observe the waves at roughly -1.6 V and -1.9 V cause this wave to disappear almost completely.

A comparison with the parent monomer complex suggests that the wave centered at -0.86 V is attributable to the poly-**btbtz** backbone. The current drop observed for this

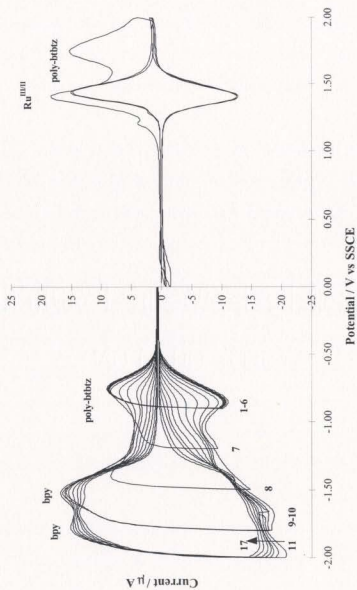


Figure 5.2: Cyclic voltammogram of poly-[Ru(btbz)(bpy)₂]³⁺²⁺ in CH₃CN/0.1 M Et₄NClO₄. Scan numbers are indicated.

wave with each scan to -1.8 V and lower can be explained by deactivation of the conjugated backbone. Thus, the waves at -1.6 V and -1.9 V must be due to bipyridine ligands. Since these waves persist after the backbone electrochemistry has degraded, the metallopolymer film must remain intact. A visual inspection of the electrode confirmed this.

Figure 5.3 shows the electrochemistry of a poly-[Ru(**btbmtz**)(bpy)₂]^{3+/2+} film. There are some obvious similarities with poly-[Ru(**btbmtz**)(bpy)₂]^{3+/2+}. This is not surprising since the oxidative polymerization of both complexes displayed nearly identical behavior. The figure details the electrochemistry of this metallopolymer on a continuous scan (scanning through positive and negative potentials for the same polymer film). The Ru^{3+/2+} process and the waves assigned to bipyridine processes are present here, but the electrochemistry of the backbone appears much less distinct than for poly-[Ru(**btbmtz**)(bpy)₂]^{3+/2+}, because the backbone has undergone degradation after exposure to high potentials on the first part of the scan (0 V to + 2.0 V). The sharp prepeak at + 1.0 V is slightly more noticeable here, and a return peak at -0.7 V is much greater in magnitude, due to solvent and counterion uptake from the CH₃CN / 0.1M Et₄NClO₄ medium in the anodic scan.

Metallopolymers incorporating Os²⁺ centers permit studies of metal-metal communication at potentials lower than those required to observe oxidation of the backbone. This is important, in that the electrochemistry of the metal center is separable from that of the organic backbone. It will also come into play when electron transport pathways are considered.

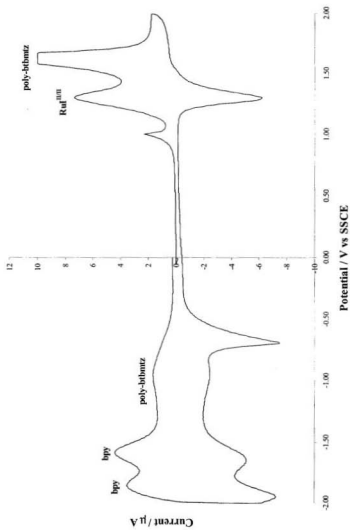


Figure S.3. Cyclic voltammogram of poly-[Ru(bibantz)(bpy)₂]³⁺²⁺ in CH₃CN/0.1 M Et₄NClO₄.

Figure 5.4 displays the voltammogram for a thin film of poly-[Os(**btbtz**)(bpy)₂^{3+/2+}], grown from CH₃CN/Et₄NClO₄/BF₃OEt₂. The appearance of the voltammogram for this polymer film resembles those for poly-[Ru(**btbtz**)(bpy)₂^{3+/2+}] and poly-[Ru(**btbmtz**)(bpy)₂^{3+/2+}]. These data were collected over the +1.0 V to -2.0 V range in one continuous scan, so the sharp uptake/discharge spikes are again seen. The low potential limits were probed as for the poly-[Ru(**btbtz**)(bpy)₂^{3+/2+}] film, revealing that the reversible wave near ~ -1V due to backbone reduction, is stable over several scans. Rapid backbone degradation was seen, however, when cycling to potentials low enough to observe the bipyridine electrochemistry. The Os^{3+/2+} wave was observed at a much lower potential (~-0.9 V) than the Ru^{3+/2+} process in poly-[Ru(**btbtz**)(bpy)₂^{3+/2+}].

Polymer films of this metal complex were also able to be grown from neat BF₃OEt₂ solutions, and the electrochemistry of these films strongly resembled each other. This is not surprising, considering the behavior for both complexes was so similar during electropolymerization (Section 4.5).

Unlike the voltammetry for a film of poly-[Os(**btbtz**)(bpy)₂^{3+/2+}] grown from CH₃CN/Et₄NClO₄/BF₃OEt₂ the reductive electrochemistry for a film of this same metallopolymer grown from a monomer solution in BF₃OEt₂ demonstrated less stability to potential cycling at low potentials (Figure 5.5).^{*} The reversible wave attributed to reduction of the polymer backbone is still present at a slightly lower potential, as is a bipyridine process. An additional peak at ~ -0.4 V is due to charge release from the as-

* Films of poly-Os(**btbtz**)(bpy)₂³⁺ were grown by potential cycling and constant potential methods; their voltammograms did not appear to differ significantly.

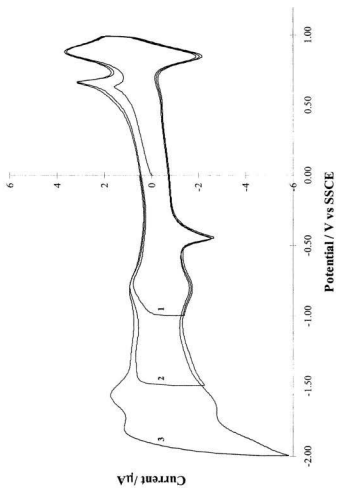


Figure 5-4: Cyclic voltammogram of poly-[Os(tbbtz)(bpy)₂]²⁺ (grown from CH₃CN / Et₄NClO₄ / BF₄OEt₂) in CH₃CN / 0.1 M Et₄NClO₄.

Scan numbers are indicated.

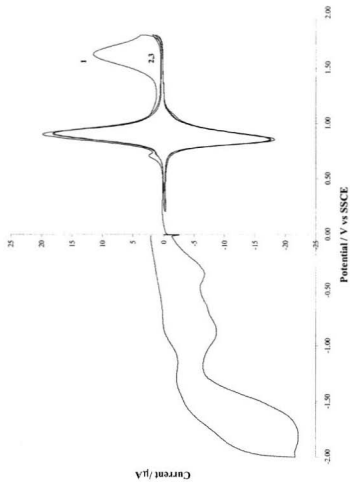


Figure 5.5: Cyclic voltammogram of poly-[Os(btbtz)(bpy)₂]³⁺ in CH₃CN/0.1 M Et₄NClO₄. Scan numbers indicated.

formed, p-doped polymer (present on the first scan only). However, these waves appear less defined than those in Figure 5.4. Scanning to potentials low enough to observe the bipyridine-based electrochemistry caused the wave centered at *ca.* -0.9 V to shift to lower potentials on subsequent scans, lending it an irreversible waveshape. The anodic electrochemistry displayed peaks which were assigned to $\text{Os}^{3+/2+}$ and backbone oxidation (which was not observed for films grown in the $\text{CH}_3\text{CN}/\text{Et}_4\text{NClO}_4/\text{BF}_3\text{OEt}_2$ system). Scanning to potentials high enough to observe the electrochemistry of the backbone resulted in complete loss of this wave after only one or two scans. The absence of this wave from the film shown in Figure 5.4 suggested that potential cycling to +1.65 V may adversely affect the π -conjugation network of the polymer product.

5.3 Electron Transport in Ruthenium and Osmium Metallopolymers

5.3.1 $D_e C_M^2$

Conductivity, σ , is the parameter most often cited in reporting the rate of charge transport through a polymer film. For systems designed with sensory applications in mind, in which the conductivity of the polymer is affected by complexation of some analyte, σ can give an indication of the species' concentration. Since σ is a combination of electronic and ionic contributions, however, it is not generally suited for describing the movement of electrons within a metallopolymer film. The electron diffusion coefficient, D_e , has been used in this study to examine electronic communication between metal centers through a conjugated backbone.

The term is solely ~~ferro~~ferrokinetic in origin, derived through the Fick relation for linear diffusion to an electrode through a thin diffusion layer [97]:

$$i = nFAD_e \frac{dC_{Ox}}{dx} \quad (5.1)$$

where i is the current, n is the number of electrons involved for a given redox reaction, A is the electrode area, C_{Ox} is the concentration of the redox species which undergoes the electron transfer reaction, and x is the distance from the electrode surface.

D_e for the $M^{3+/2+}$ process is constant across the metal wave, provided no contribution from the backbone is present, whereas σ is potential dependant. The D_e term is an uncomplicated rate constant, which can be used for comparison of metal-metal communication between systems.

Isolation of the D_c term requires an estimate of the film thickness, d . This parameter can be obtained from a slow cyclic voltammogram. Integration of the $M^{3+/2+}$ peak of the voltammogram for the metallopolymer yields the charge, Q (C), associated with this redox process ($M^{3+} \rightarrow M^{2+}$), from which can be derived the surface coverage of the metal center in the metallopolymer film, Γ_M (mol cm^{-2}):

$$\Gamma_M = \frac{Q}{FA} \quad (5.2)$$

where F is Faraday's constant (C mol^{-1}).

The film thickness can then be calculated with an approximation of the metal complex's concentration, from crystal packing data:

$$d = \frac{\Gamma_M}{C_M} \quad (5.3)$$

where C_M is the concentration of metal sites in the metallopolymer film (mol cm^{-3}).

In reality, the regularity found in crystal lattices is not seen in polymer films. The morphology of an electrogenerated polymer film is known to change with film thickness, often highly compact close to the electrode [4], and more porous in regions farther away from the electrode. Furthermore, film quality is dependent on the solvent system used in growing the film. When immersed in a solvent-electrolyte medium for analysis, the film thickness can change markedly, due to swelling associated with solvent and counterion uptake [98]. This makes interpretation of electron transport data risky. The problem is circumvented by instead reporting electron diffusion in terms of $D_e C_M^{-2}$.

5.3.2 Methods for Obtaining $D_e C_M^2$

AC Impedance has been shown to be a useful method for the collection of electron transport data for metallopolymer systems [61]. Furthermore, the experimental setup is simple relative to other techniques that have been utilized for this purpose, requiring only a polymer-coated electrode and a conventional electrochemical cell. Rotating disk voltammetry (RDV) can also be employed in order to acquire these data. For RDV, the polymer coated electrode mediates the electrochemistry of some sacrificial species. The electrode is rotated at high speeds in order to maximize the rate of mass transport of the donor species from the solution. This allows kinetic data (i.e., the electron diffusion coefficient) to be obtained. The experiments are, however, sometimes complicated by partial breakage of the film during rotation, and sometimes by permeation by the donor through the polymer film to the electrode surface. Dual electrode voltammetry (DEV) does not involve a third-party donor, but requires a conductive coating to provide an electrical contact between the electrodes through the polymer film. A thin, porous gold layer is employed for this purpose, deposited by evaporation of a small amount of gold wire at low pressure; DEV experiments are thus tedious. Quite often, these experiments fail, due to inhomogeneity of the coating and electrical shorts. Both techniques (RDV and DEV) involve slow potential cycling in order to set up concentration gradients within the film. Typically, limiting currents are obtained easily from stable, sigmoidal wave shapes. Many unsuccessful attempts were made to extract electron transport data with these two methods. For the bithiazole-based metallopolymer considered here, it

was found that because the films were so unstable to the potentials these methods demanded, no reliable information could be obtained. Inevitably, each film rapidly became deactivated during the course of an experiment.

5.3.2.1 AC Impedance Background

Although reports of electron transport measurements with AC impedance are not as widespread as with other electrochemical techniques, it has been shown to be quite effective for obtaining mechanistic and kinetic information for many electrochemical processes. Although the technique draws from basic electronics [99], a full breakdown of the theory involved is still well beyond the scope of this thesis. A rudimentary presentation of the background follows.

The behavior of the polymer-coated electrode-solution interface found in an electrochemical cell can be described in terms of an equivalent circuit model [100], such as the one shown in Figure 5.6. Real experimental observables like Faradaic capacitance (C_f) and film resistance, both ionic (R_i) and electronic (R_e) in origin, can be represented by this “finite transmission line” model. The third resistance, R_s , is the solution resistance, an experimental artifact reflecting the physical limitation of how close the reference electrode can be placed next to the working electrode.

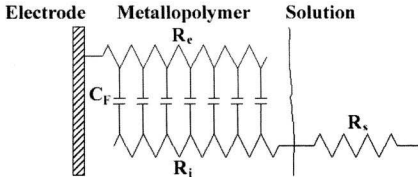


Figure 5.6: Equivalent circuit diagram for a polymer-coated electrode. Adopted from [101].

In conductive coatings like polymers, there exists a finite resistance to both electron and ion movement within the film under an applied DC potential. The relationship between the applied potential (E), the current (I) and resistance (R) is described by Ohm's law:

$$E = IR \quad (5.4)$$

Circuit elements like capacitors and inductors can impede electron flow under alternating current. The impedance (Z) of these systems is described by

$$E = IZ \quad (5.5)$$

For such systems, the current and potential sinusoidal functions are out of phase by θ (rad). The AC waveform is conveniently characterized by vector analysis, and is often reported in coordinate terms of real (Z') and imaginary (Z'') impedance. Thus,

$$Z' + Z''j = \frac{(E' + E''j)}{(I' + I''j)} \quad (5.6)$$

where $j = (-1)^{1/2}$.

Impedance experiments involve perturbation of the polymer film by a potential having a small amplitude (~5 mV) AC component. The frequency of this component is typically scanned from high to low frequency, eliciting a response from different circuit elements contained in the model.

A typical “Nyquist plot” or “complex plane impedance diagram” for a polymer-coated electrode is shown in Figure 5.7. The axes correspond to real impedance (X-axis) and imaginary impedance (Y-axis), with a high-to-low frequency scan corresponding to left-to-right along the X-axis. Real impedance derives from the resistance component of the impedance measurements, while imaginary impedance is calculated from the capacitance.

From the figure, it is seen that at very high frequencies, the capacitance of the film becomes negligible, and an intercept with the real impedance axis is obtained. The high frequency limit is described by:

$$\frac{1}{Z} = \frac{1}{R_i} + \frac{1}{R_e} \quad (5.7)$$

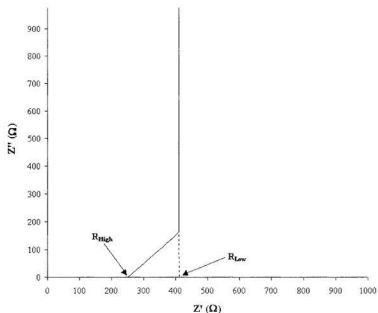


Figure 5.7: Representation of an ideal complex plane impedance plot.

In the high frequency limit, the circuit behaves as two parallel resistances, and the impedance is dominated by the smaller resistance (the current takes the more conducting pathway). The point at which the high frequency impedance intercepts the real impedance axis (R_{High} in Figure 5.7) is given by:

$$R_{\text{High}} = R_s + \frac{1}{1/R_i + 1/R_e} \quad (5.8)$$

As lower frequencies are scanned, a 45° region is observed where the real and imaginary impedance are approximately equivalent. This zone, called the “Warburg” region, corresponds to diffusion within the polymer film. For cases where $R_c \gg R_e$, the breadth of the 45° region varies little with the applied potential [102]. For the case where $R_e \gg R_i$, the length of the Warburg region is seen to vary with potential, and is at a minimum at the formal potential for the redox process of interest (the potential which maximizes electron hopping). The metallopolymer films studied in this project were found to exhibit the latter behavior, and so charge transport must be limited by the rate of electron hopping ($R_e \gg R_i$). For this case, R_{High} corresponds to the solution resistance (R_s) plus the ionic resistance (R_i) of the film. The ionic resistance can thus be obtained by subtraction of the real impedance intercept for an uncoated electrode (i.e., R_s).

At still lower frequencies, the Warburg region translates to a capacitive impedance, having a slope of 90°. Theoretically, the capacitance is constant in this region (vertical line in Figure 5.7). Experimentally, it is found that this line is truly not vertical. This peculiarity has been attributed to dispersion caused by film heterogeneity [99].

R_c can be determined from the difference between the high frequency intercept and the intercept obtained by extrapolation of the low frequency data, R_{Low} :

$$R_c = 3(R_{Low} - R_{High}) \quad (5.9)$$

Solution of the electronic resistance term allows calculation of D_e through

$$D_e = d^2 / R_c C_{Low} \quad (5.10)$$

where C_{Low} is the low frequency capacitance. Since the low frequency capacitance is not constant, the capacitance is best obtained from the slope of a plot of $-Z''$ vs ω^{-1} (Figure 5.8). Substituting for d:

$$D_e = \frac{\Gamma_M^2}{C_M^2 (R_e C_{Low})} \quad (5.11)$$

Thus, $D_e C_M^2$ is obtained from

$$D_e C_M^2 = \frac{\Gamma_M^2}{(R_e C_{low})} \quad (5.12)$$

Chidsey and Murray [54] related dc electronic conductivity, $\sigma(E_{eq})$ ($S\text{cm}^{-1}$), to $D_e(E_{eq})$ through the redox capacity, $\rho(E_{eq})$ ($F\text{cm}^{-3}$):

$$D_e(E_{eq}) = \frac{\sigma(E_{eq})}{\rho(E_{eq})} \quad (5.13)$$

Redox capacity is defined as the charge stored at equilibrium per unit volume per infinitesimal change of the potential (relative to the reference electrode). The redox capacity can be obtained from a cyclic voltammogram for materials which store charge reversibly having volume V (cm^3):

$$\rho(E_{eq}) = \frac{i(E_{eq})}{V\nu} = \frac{C(E_{eq})}{V} \quad (5.14)$$

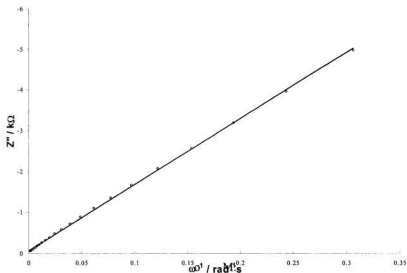


Figure 5.8: Plot of $-Z''$ vs ω^{-1} to obtain low frequency capacitance for poly-Os(btbtz)(bpy) $_2^{2+}$. Data collected in $\text{CH}_3\text{CN}/0.1\text{M Et}_4\text{NClO}_4$ at 0.8 V vs SSCE.

where v is the scan rate (V sec^{-1}). $C(E)$ is the capacitance calculated at a certain potential (E). The volume is obtained by integration of the capacitance over the $\text{M}^{3+/2+}$ process: n_s is the number concentration of sites (1.52 M) N_A , where N_A is Avagadro's number, and e is the electron charge. The concentration term is derived from crystal packing data.

$$V = \int_{\text{MII}}^{\text{MIII}} C(E_{\text{eq}}) dE / (en_s) \quad (5.15)$$

5.4 AC Impedance Experiments and Results

5.4.1 Polymer Film Preparation

For electron transport experiments, metallopolymer films were grown just prior to their analysis. The cyclic voltammograms of films grown by potential cycling, constant potential, and constant current were not significantly different, suggesting that the method chosen for film growth was not important. Still, galvanostatic (constant current) and potentiostatic (constant potential) approaches are preferable to potential cycling, due to concerns with unwanted species (impurities, unreacted monomer) diffusing to the electrode during the low potential portion of each cycle, affecting film makeup and thus possibly affecting the migration of charge. Furthermore, a constant electrode reaction permits the reactive monomer to be utilized more efficiently in the makeup of the film, and is superior insofar as reproducing film thickness.

For poly-[Ru(btbtz)(bpy)₂^{3+/2+}] data considered here, constant current and constant potential polymerizations were employed. In galvanostatic polymerizations, the monomer is oxidized at the rate dictated by the current. If the diffusion layer around the electrode becomes too depleted of monomer, then the potential necessarily rises until another species in solution can be oxidized to meet the current demand. For this reason, the currents employed in these experiments were low (0.15 mA cm⁻²). The potential was carefully monitored so that it did not rise to a level at which overoxidation was an overriding concern. For these films, the potential was seen to drift positively until (typically) about 1.48 V.

Figure 5.9 shows surface coverages (Γ) and $D_e C_M^{-2}$ values for films of poly-[Ru(**btbtz**)(bpy)₂^{3+/2+}] grown at constant current. The surface coverage (mol cm⁻²) of films grown under galvanostatic control appeared to be reasonably controllable by varying the polymerization time. Fairly linear behavior was observed for surface coverage with polymerization times over most of the time interval investigated. The slight drop off of the coverage at longer times was expected, as regions of the film farther removed from the electrode surface would have been less compact and thus less dense. The slightly lower D_e values observed for the thinnest films could be attributed to the greater uncertainty in the estimation of their electronic resistances, which was small relative to the solution resistance.

A series of four films of poly-[Ru(**btbtz**)(bpy)₂^{3+/2+}] was also grown by constant potential (1.45 V vs SSCE) in order to examine the role of the polymerization route on the electron transport properties for these systems. This comparison is important, because the poly-Os(**btbtz**)(bpy)₂²⁺ films reported here were only able to be grown at constant potential (1.5 V vs SSCE). Since relative D_e values for these metallopolymers will be used to evaluate possible superexchange pathways, the role of the polymerization method needs to be established.

It was found that the surface coverage was less controllable for films of poly-Ru(**btbtz**)(bpy)₂²⁺ and poly-Os(**btbtz**)(bpy)₂²⁺ grown at constant potential.

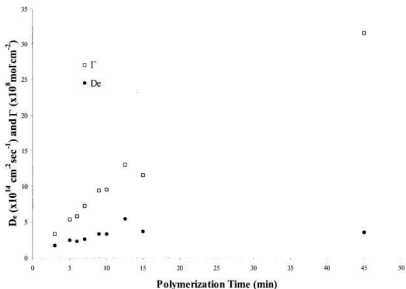


Figure 5.9: Dependence of surface coverage (Γ , \square ($\times 10^6$ mol cm^{-2}) and $D_{C_M}^2$, \bullet ($\times 10^{14}$ mol² cm^{-4} s^{-1}) on polymerization time. Films were grown at a constant current density of 0.15 mA cm^{-2} from ca. 2.2 mM $\text{Ru}(\text{bttz})(\text{bpy})_2(\text{PF}_6)_2$ in $\text{BF}_3 \cdot \text{Et}_2\text{O}$ and tested in $\text{CH}_3\text{CN}/0.1\text{M Et}_4\text{NClO}_4$ at 1.32 V vs SSCE.

5.4.2 Poly-Os(bttz)(bpy)₂²⁺

Figure 5.5 shows that the electrochemistry of the $\text{Os}^{3+/2+}$ process in poly-[$\text{Os}(\text{bttz})(\text{bpy})_2^{3+/2+}$] films is well resolved from the electrochemistry of the polymer backbone (the polymer wave is observed at about +1.75 V, while the $\text{M}^{3+/2+}$ wave is seen at a potential of only +0.9 V). This makes interpretation of electron transport data for this

system straightforward. The impedance across the $\text{Os}^{3+/2+}$ wave follows well the theoretical behavior described in section 5.2.2.1. Impedance experiments for this polymer were able to be conducted at any point on the wave without concern for unwanted reactions during the measurements. This cannot be said for experiments on poly-[Ru(**btbtz**)(bpy)₂^{3+/2+}] films because of partial overlap by the higher potential backbone electrochemistry. For this reason, electron transport in poly-[Os(**btbtz**)(bpy)₂^{3+/2+}] films is dealt with before moving on to a more complicated scenario for ruthenium metallopolymers.

Figure 5.10 shows the AC impedance for a poly-[Os(**btbtz**)(bpy)₂^{3+/2+}] film at 0.75 V (at the very onset of the $\text{Os}^{3+/2+}$ electrochemistry), 0.8 V (a potential on the $\text{Os}^{3+/2+}$ wave, but well before the formal potential) and 0.89 V (close to the formal potential), and at 1.0 V (past the formal potential). It is easily seen that the length of the Warburg line is greater for experiments conducted at potentials farther away from the formal potential. It is shortest near the formal potential. This indicates that the ionic resistance in the polymer film must be much less than the electronic resistance. Otherwise, the 45° region would correspond to ion migration-diffusion, and its length would change little with potential. Furthermore, for the case $R_c \gg R_e$, the high frequency intercept would be expected to migrate to lower values with higher potentials, as ionic resistance is expected to film). The invariance of the high frequency intercept with potentials thus shows that for this system, $R_c \gg R_e$ (Figure 5.11).

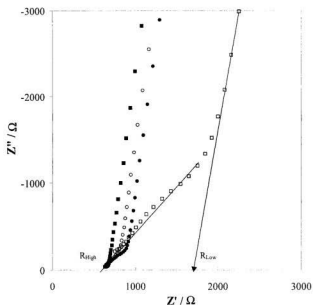
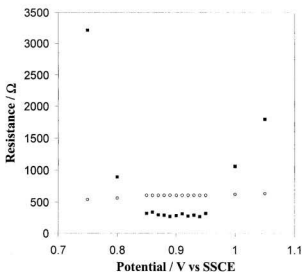


Figure 5.10: AC impedance of a poly-Os(btbtz)(bpy)₂²⁺ film at 0.75 V (□), 0.8 V (●) and 0.89 V (■) and 1.00 V (○) in CH₃CN/0.1M Et₄NClO₄, $\Gamma = 2.2 \times 10^{-8}$ mol cm⁻².

Figure 5.12 shows the capacitance of the same poly-Os(btbtz)(bpy)₂²⁺ film at various potentials across the Os^{3+/2+} wave. The capacitance can be seen to reach a maximum at the formal potential, while the resistance goes through a minimum at this value. Since $D_c C_M^{-2}$ is calculated from both R_c and C_{Low} (eq. 5.12), D_c is found to be relatively independent of potential across the same window (Figure 5.13). In fact, the deviations from straight line behavior have been explained by compositional changes accompanying oxidation of the polymer during electron transport experiments [54].



5.11: Electronic resistance (R_e , ■) and high frequency impedance intercept (R_{high} , ○) for potentials spanning the Os^{III} wave of poly-[Os(**btbtz**)(bpy) $_2^{3+/2+}$] in $CH_3CN/0.1M Et_4NClO_4$, $\Gamma = 2.2 \times 10^{-8} mol\ cm^{-2}$. The relative invariance of R_{high} with potential is indicative of a film in which $R_c \gg R_i$.

The role of the conjugated backbone for poly-Os(**btbtz**)(bpy) $_2^{2+}$ was interrogated by comparison of the electron transport rates obtained for newly made films and overoxidized, deactivated films. Films were deactivated by potential scanning in $CH_3CN/0.1M Et_4NClO_4$ to +2.0 V for at least two scans. Complete deactivation was evidenced by the total lack of electrochemical response over the potential range which encompasses the backbone wave for newly synthesized films. $D_e C_M^{-2}$ for poly-[Os(**btbtz**)(bpy) $_2^{3+/2+}$] was found to be $(5.8 \pm 4.1) \times 10^{-14} mol^2\ cm^4\ s^{-1}$ (8 films). For an

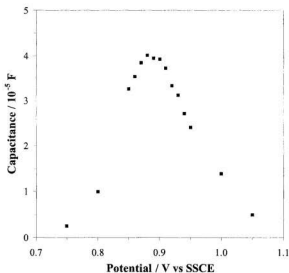


Figure 5.12: Low frequency capacitance for potentials which straddle the Os^{3+2+} process of a poly- $\text{Os}[(\text{btbtz})(\text{bpy})_2^{3+2+}]$ film in $\text{CH}_3\text{CN} / 0.1\text{M Et}_4\text{NClO}_4$. $\Gamma = 2.2 \times 10^{-6} \text{ mol cm}^{-2}$.

overoxidized film, the value dropped to $(0.8 \pm 0.2) \times 10^{-14} \text{ mol}^2 \text{ cm}^4 \text{ s}^{-1}$ (3 films). This corresponds to greater than a seven-fold drop in $D_c C_M^2$ following overoxidation of the conjugated backbone.

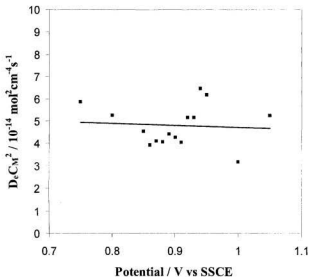


Figure 5.13: $D_e C_M^2$ of a poly-[Os(btbtz)(bpy)₂]^{3+/2+} film over 0.75 V to 1.05 V in CH₃CN / 0.1M Et₄NClO₄.

$$\Gamma = 2.2 \times 10^{-8} \text{ mol cm}^{-2}.$$

5.4.3 Poly-Ru(btbtz)(bpy)₂²⁺

Electron transport studies on the $M^{3+/2+}$ wave for films of poly-[Ru(btbtz)(bpy)₂^{3+/2+}] were not as easily interpreted as for films of poly-[Os(btbtz)(bpy)₂^{3+/2+}] because of partially overlapping backbone electrochemistry. Not only does this present a problem in that a backbone contribution to $D_e C_M^2$ must be considered, but also because the backbone was found to undergo degradation even at low potentials on the $Ru^{3+/2+}$ wave. The slow deactivation of the backbone becomes accelerated as the potential is increased, as shown in Figure 5.14. Although it is evident that experiments conducted at potentials near the $M^{3+/2+}$ formal potential for poly-[Ru(btbtz)(bpy)₂^{3+/2+}] will likely cause partial deactivation of the electronic architecture of the backbone, these experiments were carried out at 1.32 V. The role of the conjugated backbone in electron (hole) transport was then investigated for the deactivated metallopolymer at the same potential. Experiments were conducted at this potential because at the lowest potentials of Figure 5.14, the concentration of Ru^{3+} sites is so low that it introduces an unacceptable degree of uncertainty in the measurement of the $D_e C_M^2$ data. Furthermore, because overoxidation will shift the electrochemistry of the metal process to the right (see Figure 5.2), measurements conducted on deactivated metallopolymer at potentials too low (*ca.* 1.2 V) will fall short of the $Ru^{3+/2+}$ wave. While electron hopping rates are maximized at the formal potential (1.37 V), the operating potential for these experiments was made below this to lower the possibility of polymer-mediated transport.

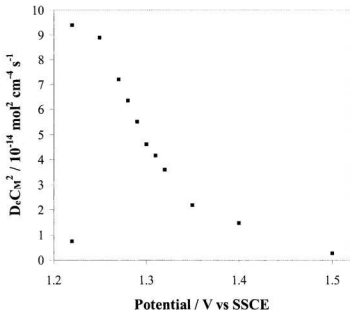


Figure 5.14: Decrease of $D_e C_M^2$ with potential (1.22 V to 1.5 V) across a $\text{Ru}^{3+/2+}$ wave due to backbone deactivation. Experiment performed in $\text{CH}_3\text{CN}/0.1\text{M Et}_4\text{NClO}_4$, $\Gamma_M = 4. \times 10^{-6} \text{ mol cm}^{-2}$. The second point at 1.22 V shows $D_e C_M^2$ after deactivation. Scan duration ~ 60 s.

$D_e C_M^2$ values for poly- $[\text{Ru}(\text{btbtz})(\text{bpy})_2^{3+/2+}]$ films were obtained from two consecutive impedance experiments at 1.32 V, in order to gauge the effect of the operating potential on the data. On average, $D_e C_M^2$ decreased by *ca.* 20 % between measurements, although it did increase in several cases. The $D_e C_M^2$ values obtained at a single potential should be reasonably accurate, since the decay is slow relative to the time

it takes to collect the impedance data.

AC impedance experiments for poly-[Ru(**btbtz**)(bpy)₂^{3+/2+}] films grown by constant current and constant potential yielded $D_e C_M^2$ values of $(3.4 \pm 1.3) \times 10^{-13} \text{ mol}^2 \text{ cm}^4 \text{ s}^{-1}$ and $(2.6 \pm 1.2) \times 10^{-13} \text{ mol}^2 \text{ cm}^4 \text{ s}^{-1}$, respectively. After deactivation of the conjugated backbone (accomplished by holding the potential at +1.8 V for 30-60 s), $D_e C_M^2$ was found to drop to $(4.6 \pm 1.6) \times 10^{-13} \text{ mol}^2 \text{ cm}^4 \text{ s}^{-1}$ for films grown by both routes. Thus the polymerization method does not appear to significantly affect electron transport.

5.4.4 Superexchange Pathways

A comparison of the $D_e C_M^2$ data for poly-[Os(**btbtz**)(bpy)₂^{3+/2+}] and poly-[Ru(**btbtz**)(bpy)₂^{3+/2+}] obtained in AC impedance experiments shows that this data is more than five times greater in the latter system. If outer sphere electron exchange were the dominant form of charge transport, then $D_e C_M^2$ would be expected to be larger in poly-[Os(**btbtz**)(bpy)₂^{3+/2+}] because the greater diameter of the osmium center would enhance contact between neighboring metal complex sites. This would facilitate electron hopping in this system relative to that in the ruthenium metallopolymer. Clearly, the conjugated backbone must be involved in charge transport.

Poly-[Os(**btbtz**)(bpy)₂^{3+/2+}] demonstrates electron transport rates which are more than seven times higher in newly formed films than for overoxidized coatings, when tested at the formal potential. The lack of significant overlapping conjugated polymer

electrochemistry indicates that transport rates are not enhanced by a polymer-mediated mechanism, so a superexchange means of transit must be at work. For the ruthenium system, there is a possibility that a polymer-mediated mechanism could contribute to $D_e C_M^{-2}$, since the backbone electrochemistry is partially obscured by the metal process. Since the voltammetry for poly-[Ru(btbtz)(bpy)₂^{3+/2+}] is unstable at the potential used in these experiments, a major contribution to charge transport by a polymer-mediated mechanism is not as credible as by a superexchange explanation, since the oxidized sites necessary for backbone mediation to contribute would also be unstable. The decay of $D_e C_M^{-2}$ with potential lends credence to a superexchange pathway, because it would be expected that a greater concentration of oxidized sites in the backbone (as the formal potential for the conjugated polymer is approached) would facilitate charge transport by this route. Thus, $D_e C_M^{-2}$ for systems in which superexchange is the prevailing mechanism of electronic movement should be relatively independent of potential. The drop of $D_e C_M^{-2}$ with increasing potential shown in Figure 5.14 is most likely a consequence of backbone deactivation, the effects of which are compounded by each previous measurement. Still, it has been reported for at least one case that polymer mediated metal-metal communication can demonstrate potential independent $D_e C_M^{-2}$ data [66]. For this reason, polymer-mediated communication cannot be entirely ruled out.

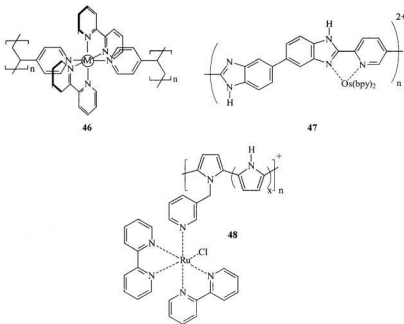
It would appear that the most plausible explanation for enhanced transport rates for bithiazole-bithiophene metallopolymers involves superexchange as the dominant mechanism. The fact that $D_e C_M^{-2}$ values are about five times greater in the ruthenium

polymer than in the osmium system can be explained by better overlap of the Ru d -orbitals with the π -orbitals of the conjugated backbone. This statement is supported by reports of electron transport data in ruthenium and osmium polybenzimidazole systems.

5.3.5 Comparisons with Literature Systems

Table 5.1 summarizes $D_e C_M^2$ values for poly-[Ru(**btbtz**)(bpy) $_2$ $^{3+/2+}$], poly-[Os(**btbtz**)(bpy) $_2$ $^{3+/2+}$], and several other ruthenium and osmium systems reported in the literature. The ruthenium and osmium poly(4-vinylpyridine) metallopolymer designs (**46**) represent redox metallopolymer designs, while poly-[Ru((6,6'-bibenzimidazole-2,2'-diyl)-2,5-pyridine)(bpy) $_2$ $^{3+/2+}$] and poly-[Os((6,6'-bibenzimidazole-2,2'-diyl)-2,5-pyridine)(bpy) $_2$ $^{3+/2+}$] (**47**) are both conjugated metallopolymer designs consisting of a less electron-rich backbone. The metallopolymer poly-[Ru(bpy) $_2$ (3-(pyrrol-1-ylmethyl)pyridine) $_2$ $^{3+/2+}$] (**48**) is a redox-conjugated polymer hybrid in which the redox centers are electronically quarantined from the electroactive backbone by a saturated alkane linkage.

The redox metallopolymer designs are useful for comparisons with the bithiazole materials discussed here as they clearly call into account the role of the conjugated π -system in electronic transport. $D_e C_M^2$ for poly-[Ru(4-vinylpyridine) $_2$ (bpy) $_2$ $^{3+/2+}$] is reported to be about 180 times lower than the data presented here for poly-[Ru(**btbtz**)(bpy) $_2$ $^{3+/2+}$] [65]. Since the saturated poly(4-vinylpyridine) backbone cannot



provide a means of electron transport, the sole mode of metal-metal communication here is through outer sphere electron exchange. As expected, $D_e C_M^2$ for the metallopolymer incorporating the larger osmium center is greater.

For the metallopolymer poly-[Ru(bpy)₂(3-(pyrrol-1-ylmethyl)pyridine)₂]^{3+/2+}, $D_e C_M^2$ is 67 times lower than in poly-[Ru(**btbtz**)(bpy)₂]^{3+/2+}. In this system, electron transport is enhanced relative to poly-[Ru(4-vinylpyridine)₂(bpy)₂]^{3+/2+} because the conjugated backbone can contribute to the overall rate of charge transport. It is still some 3 times less than for poly-[Ru((6,6'-bibenzimidazole-2,2'-diyl)-2,5-pyridine)(bpy)₂]^{3+/2+}.

	$D_e C_M^2$ ($\times 10^{14}$ mol ² cm ⁻⁴ s ⁻¹) ^a	$D_e C_M^2$ ($\times 10^{14}$ mol ² cm ⁻⁴ s ⁻¹) ^b
poly-Ru(btbtz)(bpy) ₂ ²⁺	32 (±13) (13 films)	4.6 (±1.6) (13 films)
poly-Os(btbtz)(bpy) ₂ ²⁺	5.8 (±4.1) (8 films)	0.8 (±0.2) (3 films)
poly-[Ru((6,6'-bibenzimidazole-2,2'-diyl)-2,5-pyridine)(bpy) ₂ ^{3+/2+}] ^c	1.5 (±0.8) ^d	
poly-[Os((6,6'-bibenzimidazole-2,2'-diyl)-2,5-pyridine)(bpy) ₂ ^{3+/2+}] ^c	0.71 (±0.41) ^e	
poly-[Ru(4-vinylpyridine) ₂ (bpy) ₂ ^{3+/2+}] ^f	0.18 (±0.09)	
poly-[Os(4-vinylpyridine) ₂ (bpy) ₂ ^{3+/2+}] ^f	1.2 (±0.4)	
poly-[Ru(bpy) ₂ (3-(pyrrol-1-ylmethyl)pyridine) ₂ ^{3+/2+}] ^g	0.48	

Table 5.1: $D_e C_M^2$ values for Pt coated electrodes for several metallopolymers in CH₃CN/0.1M Et₄NClO₄.

a) Obtained for as-formed film.

b) Obtained after electrochemical deactivation by: i) holding the electrode potential at 1.8 V for 30-60 s; ii) potential cycling between 0 to +2.0 V for at least two full cycles.

c) From ref. [63].

d) + ca. 50 mM HClO₄.

e) + ca. 5 mM Bu₃NOH.

f) From ref. [65].

g) From ref. [66].

It is seen that $D_e C_M^2$ for poly-[Ru(**btbtz**)(bpy)₂^{3+/2+}] is more than twenty times greater than that found in poly-[Ru((6,6'-bibenzimidazole-2,2'-diyl)-2,5-pyridine)(bpy)₂^{3+/2+}] [63]. For these polybenzimidazole films, it was reported that better transport rates were obtained for metallopolymers incorporating ruthenium centers than for osmium centers as a result of better d_M - π_L orbital overlap. Trading this backbone for a poly-**btbtz** chain should raise the HOMO energy of the bridging ligand, as shown in Figure 5.15. This should result in improved overlap of ruthenium's d-orbitals with the π -system and thus result in higher $D_e C_M^2$ values. For ruthenium and osmium benzimidazole metallopolymers, it was found that deprotonation of the backbone enhanced $D_e C_M^2$ for the ruthenium model, but diminished it for the osmium metallopolymer [63]. In conjunction with other observations, this pointed to hole-type superexchange in the ruthenium system and electron-type superexchange for the osmium system, since removal of the imidazole proton in would lower the HOMO and LUMO energy bands of polybenzimidazole. The poly-**btbtz** backbone is more electron rich, and thus the energy of its HOMO band is elevated relative to polybenzimidazole's. The $D_e C_M^2$ data obtained for poly-[Ru(**btbtz**)(bpy)₂^{3+/2+}] suggest that the ruthenium d-orbital energy lies closer to the HOMO band energy of the polymer ($\pi_{\text{poly-btbtz}}$ in Figure 5.1 bottom) than the LUMO energy. Thus, for metallopolymers incorporating this backbone, hole-type superexchange is predicted to occur. The relative difference in the magnitudes of $D_e C_M^2$ for these two systems (**btbtz** and **bbim**) must consider differences in the rigidity of the backbones,

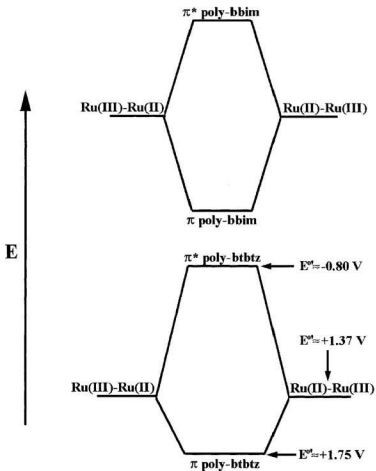


Figure 5.15: Orbital energy diagrams (not drawn to scale) for ruthenium metallopolymer possessing a poly[(6,6'-bibenzimidazole-2,2'-diyl)-2,5-pyridine] (poly-bbim) backbone (top) and a poly[5,5'-bis(2-thienyl)-2,2'-bithiazole] (poly-btbtz) backbone (bottom).

which should be greater in the polybenzimidazole structure. Thus, the higher overall $D_c C_M^{-2}$ values obtained for the bithiophene-bithiazole metallopolymers probably figures in an increased contribution by electron hopping.

Metallopolymer films of $\text{Ru}(\text{btbmtz})(\text{bpy})_2(\text{PF}_6)_2$ were also prepared, as mentioned in section 5.2. Electron transport measurements were carried out for several films at potentials near the bottom of and just below the formal potential of the Ru^{III} wave. These were grown by potential cycling through the **btbztz** ligand oxidation peak, and have not been included in the discussion of $D_c C_M^{-2}$ data.

On a final note, it is interesting that there is no reversal of the relative electron transport rates for the overoxidized metallopolymers. The degradation of the conjugated backbone by electrochemical overoxidation was expected to result in greater $D_c C_M^{-2}$ data for poly- $[\text{Os}(\text{btbztz})(\text{bpy})_2^{3+/2+}]$, as is noted for the redox metallopolymers. The higher transport rate for deactivated for poly- $[\text{Ru}(\text{btbztz})(\text{bpy})_2^{3+/2+}]$ suggests some conjugation remains after holding these films at a high potential. The instability of the polymer electrochemistry with high potentials (Figure 5.2), however, seems to indicate that the application of a 1.8 V potential to such a film for an extended period would greatly affect its conjugation. A small amount of the enol form (**50** of Figure 5.16) of the structure proposed for the overoxidized backbone (**49**) may offer an explanation, since the potentials investigated for poly- $[\text{Os}(\text{btbztz})(\text{bpy})_2^{3+/2+}]$ would be low enough that its contribution to $D_c C_M^{-2}$ would be minor relative to that in for poly- $[\text{Ru}(\text{btbztz})(\text{bpy})_2^{3+/2+}]$.

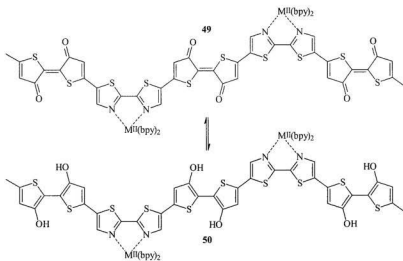


Figure 5.16: Overoxidized poly-Ru(btbtz)(bpy)₂²⁺ segment (**49**) and its conjugated enol form (**50**).

Chapter 6

Summary

The results presented in this thesis further develop the idea that a conjugated backbone can provide a superior means of electron transport between the metal centers of a metallopolymer. The idea was born from results for dinuclear complexes incorporating d^6 metal centers, and was first pursued in studies made on polybenzimidazole systems having relatively high-lying HOMO bands and low-lying LUMO bands. The encouraging findings for these systems led to the conclusion that both hole-type and electron-type superexchange mechanisms were possible, depending on the metal center (Ru or Os). The more electron-rich bithiophene-co-bithiazole backbone was chosen for the work in this thesis to raise the energy of the HOMO band in order to improve energy matching of the metal center with the conjugated backbone. Consequently, the $D_e C_M^2$ values reported here are higher than those for benzimidazole-based metallopolymers.

Studies on poly-[Os(**btbtz**)(bpy)₂^{3+/2+}] and poly-[Ru(**btbtz**)(bpy)₂^{3+/2+}] clearly showed that the π -system in these materials is involved in charge transport. For the osmium system, there was no apparent overlap of the organic backbone's electrochemistry with that of the metal center. The drop of $D_e C_M^2$ for these films after exposure to elevated potentials strongly points to a superexchange pathway. For the ruthenium polymer, the evidence is not as compelling, since there is an opportunity here for oxidized segments of the backbone to contribute to the overall charge transport rate. Still, since it is clear that outer sphere electron exchange cannot be the major contributor here, the high $D_e C_M^2$ for this system must somehow be enhanced by the backbone, be it through superexchange or polymer mediation. A superexchange-dominated scheme would fit the data reported in this thesis, with a hole-type mechanism proposed for poly-



$\text{Ru}(\mathbf{btbmtz})(\text{bpy})_2(\text{PF}_6)_2$ and $\text{Os}(\mathbf{btbmtz})(\text{bpy})_2(\text{ClO}_4)_2$ were synthesized in order to produce poly- $[\text{Ru}(\mathbf{btbmtz})(\text{bpy})_2]^{3+/2+}$ and poly- $[\text{Os}(\mathbf{btbmtz})(\text{bpy})_2]^{3+/2+}$, which should have a better orbital energy match than the **btbtz**-based metallopolymers, and thus display enhanced electron-transport rates. Further work in this area should include electron transport experiments on these two metallopolymers, to compare $D_e C_M^2$ between **btbtz** and **btbmtz** backbones. The study of metallopolymers of **43** and **44** would also be interesting, since their HOMO band energies should lie lower than the HOMO energy of **btbtz**.

The problems associated with overoxidation of the **btbtz** backbone could be alleviated by employing pyrrole as a polymerizable end group, rather than thiophene. Electrochemical properties like charge storage and conductivity are known to be enhanced for polypyrrole films in solvents containing a small percentage of water [96]. It is also believed to facilitate the electropolymerization of pyrrole and inhibit oligomer formation [96].

References

1. Heinze, J. *Synth. Met.* **1991**, 41-43, 2805.
2. Goppelsroeder, F. *Bull. Soc. Ind.* **1876**, 82, 1392.
3. Chiang, C. K.; Park, Y. W.; Heeger, A. J.; Shirakawa, H.; Louis, E. J.; MacDarmid, A. G. *Phys. Rev. Lett.* **1977**, 39, 1098.
4. Skotheim, T. A.; Elsenbaumer, R. L.; Reynolds, J. R., Ed.; *Handbook of Conducting Polymers, 2nd Edition, Revised and Expanded*. Marcel Dekker: New York, 1986.
5. Dotrong, M.; Mehta, R.; Balchin, G. A.; Tomlinson, R. C.; Sinsky, M.; Lee, C. Y.-C.; Evers, R. C. *J. Poly. Sci. A* **1993**, 31, 723.
6. Arbizzani, C.; Mastragostino, M.; Meneghello, L. *Electrochimica Acta* **1996**, 41, 21.
7. Mortimer, R. J. *Electrochimica Acta* **1999**, 44, 2971.
8. Miller, J. S. *Adv. Mater.* **1993**, 5, 587.
9. Miller, J. S. *Adv. Mater.* **1993**, 5, 671.
10. Lau, A. N. K.; Miller, L. L. *J. Am. Chem. Soc.* **1983**, 105, 5271.
11. Murray, R. W.; Ewing, A. G.; Durst, R. A. *Anal. Chem.* **1987**, 59, 379A.
12. Scott, J. C. *Science* **1997**, 278, 2071.
13. Pickup, P. G.; Kean, C. L.; Lefebvre, M. C.; Li, G.; Qi, Z.; Shan, J. *J. New Mater. Electrochem. Sys.* **2000**, 3, 21.
14. Bar-Cohen, Y. *Electroactive Polymers as Artificial Muscles - Capabilities,*

Potentials and Challenges In. *Handbook on Biomimetics*; Osada, Y. Ed.; NTS Inc.: Tokyo, 2000.

15. Burgmayer, P.; Murray, R. *J. Am. Chem. Soc.* **1982**, 104, 6140.
16. Ren, X.; Pickup, P. G. *J. Electroanal. Chem.* **1994**, 365, 289.
17. Salaneck, W. R.; Bredas, J. L. *Synth. Met.* **1994**, 67, 15.
18. Pickup, P. G. *Electrochemistry of Electronically Conducting Polymer Films. In Modern Aspects of Electrochemistry, Vol. 33*; Conway, B. E.; Bockris, J. O'M; White, R. E., Eds.; Plenum: New York, 1999.
19. Diaz, A. F.; Castillo, J. I. *J. Chem. Soc., Chem. Commun.* **1980**, 397.
20. Trouillet, L.; DeNicola, A.; Guillerez, S. *Chem. Mater.* **2000**, 12, 1611.
21. Bao, Z.; Chan, W. K.; Yu, L. *J. Am. Chem. Soc.* **1995**, 117, 12426.
22. Donat-Bouillud, A.; Mazerolle, L.; Gagnon, P.; Goldenberg, L.; Petty, M. C.; Leclerc, M. *Chem. Mater.* **1997**, 9, 2817.
23. Roncali, J. *J. Mater. Chem.* **1999**, 9, 1875.
24. Lere-Porte, J.-P.; Moreau, J. J.; Torrelles, C. *Eur. J. Org. Chem.* **2001**, 1249.
25. Stein, P. C.; Botta, C.; Bolognesi, A.; Catallani, M. *Synth. Met.* **1995**, 69, 305.
26. Chen, W.-C.; Jenekhe, S. A. *Macromolecules* **1995**, 28, 465.
27. Zhou, Z.-H.; Maruyama, T.; Kanabara, T.; Ikeda, T.; Ichimura, K.; Yamamoto, T.; Tokuda, K. *J. Chem. Soc., Chem. Commun.* **1991**, 1210.
28. Maruyama, T.; Suganama, H.; Yamamoto, T. *Synth. Met.* **1995**, **74**, 183.
29. Bolognesi, A.; Catellani, M.; Destri, S.; Porzio, W. *Synth. Met.* **1987**, 18, 129.

30. Schiavon, G.; Zotti, G.; Bontempelli, G. *J. Electroanal. Chem.* **1984**, 161, 323.
31. Zotti, G.; Schiavon, G. *J. Electroanal. Chem.* **1984**, 163, 385.
32. Schiavon, G.; Zotti, G.; Bontempelli, G. *J. Electroanal. Chem.* **1985**, 194, 327.
33. Yamamoto, T.; Saito, N. *Macromol. Chem. Phys.* **1996**, 197, 165.
34. Nanos, J. I.; Kampf, J. W.; Curtis, M. D.; Gonzales, L.; Martin, D. C. *Chem. Mater.* **1995**, 7, 2232.
35. Politis, J. K.; Curtis, M. D.; Gonzalez, L.; Martin, D. C.; He, Y.; Kanicki, J. *Chem. Mater.* **1998**, 10, 1713.
36. Tanaka, S.; Kaeriyama, K.; Hiraide, T. *Makromol. Chem., Rapid Commun.* **1988**, 9, 743.
37. Wolf, M. O.; Wrighton, M. S. *Chem. Mater.* **1994**, 6, 1526.
38. Jenkins, I. H.; Pickup, P. G. *Macromolecules* **1993**, 26, 4450.
39. Yamamoto, T.; Suganuma, H.; Maruyama, T.; Inoue, T.; Muramatsu, Y.; Arai, M.; Komarudin, D.; Ooba, N.; Tomaru, S.; Sasaki, S.; Kubota, K. *Chem. Mater.* **1997**, 9, 1217.
40. Yamamoto, T.; Suganuma, H.; Saitoh, Y.; Maruyama, T.; Inoue, T. *Jpn. J. Appl. Phys.* **1996**, 35, L1142.
41. He, Y.; Politis, J. K.; Cheng, H.; Curtis, M. D.; Kanicki, J. *IEEE Trans. Electron. Dev.* **1997**, 44, 1282.
42. Curtis, M. D.; Cheng, H.; Nanos, J. L.; Nazri, G.-A. *Macromolecules* **1998**, 31, 205.

43. Baker, A. T.; Goodwin, H. A. *Aust. J. Chem.* **1985**, 38, 851.
44. Craig, D. C.; Goodwin, H. A.; Onggo, D.; Rae, A. D. *Aust. J. Chem.* **1988**, 41, 1625.
45. Cosnier, S.; Deronzier, A.; Moutet, J.-C. *J. Electroanal. Chem.* **1985**, 193, 193.
46. Higgins, S.; Crayston, J. A. *Synth. Met.* **1993**, 879.
47. Pickup, P. G. *J. Mater. Chem.* **1999**, 9, 1641.
48. Creutz, C. *Prog. Inorg. Chem.* **1981**, 30, 1.
49. Yamamoto, T.; Maruyama, T.; Zhou, Z.-H.; Ito, T.; Fukuda, T.; Yoneda, Y.; Begum, F.; Ikeda, T.; Sasaki, S.; Takezoe, H.; Fukuda, A.; Kubota, K. *J. Am. Chem. Soc.* **1994**, 116, 4832.
50. Kingsborough, R.; Swager, T. *Prog. Inorg. Chem.* **1999**, 48, 123.
51. McQuade, D. T.; Pullen, A. E.; Swager, T. M. *Chem. Rev.* **2000**, 100, 2537.
52. Yamamoto, T.; Maruyama, T. *Inorganica Chimica Acta* **1995**, 238, 9.
53. Zhu, S. S.; Swager, T. M. *Adv. Mater.* **1996**, 8, 497.
54. Chidsey, C. E. D.; Murray, R. W. *J. Phys. Chem.* **1986**, 90, 1479.
55. Zhu, S. S.; Kingsborough, R. P.; Swager, T. M. *J. Mater. Chem.* **1999**, 9, 2123.
56. Zhu, S. S.; Carroll, P. J.; Swager, T. M. *J. Am. Chem. Soc.* **1996**, 118, 8713.
57. Zhu, S. S.; Swager, T. M. *J. Am. Chem. Soc.* **1997**, 119, 12568.
58. Buey, J.; Swager, T. M. *Angew. Chem. Int. Ed.* **2000**, 39, 608.
59. Vogel, H.; Marvel, C. S. *J. Poly. Sci.* **1961**, L511.
60. Cameron, C. G.; Pickup, P. G. *J. Chem. Soc., Chem. Commun.* **1997**, 303.

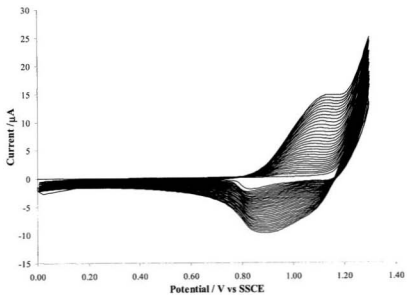
61. Cameron, C. G.; Pickup, P. G. *J. Am. Chem. Soc.* **1999**, 121, 11773.
62. Cameron, C. G.; Pickup, P. G. *J. Am. Chem. Soc.* **1999**, 121, 7710.
63. Cameron, C. G.; Pittman, T. J.; Pickup, P. G. *J. Phys. Chem. B* **2001**, 105, 8838.
64. Haga, M.; Ano, T.; Kano, K.; Yamabe, S. *Inorg. Chem.* **1991**, 30, 3843.
65. Pickup, P. G.; Kutner, W.; Leidner, C. R.; Murray, R. W. *J. Am. Chem. Soc.* **1984**, 106, 1991.
66. Ochmanska, J.; Pickup, P. G. *J. Electroanal. Chem.* **1991**, 297, 197.
67. Bauerle, P.; Scheib, S. *Adv. Mater.* **1993**, 5, 848.
68. Bauerle, P.; Gotz, G.; Hiller, M.; Scheib, S.; Fischer, T.; Segelbacher, U.; Bennati, M.; Grupp, A.; Mehring, M.; Stoldt, M.; Seidel, C.; Geiger, F.; Schweiser, H.; Umbach, E.; Schmelzer, M.; Roth, S.; Egelhaaf, H. J.; Oelkrug, D.; Emele, P.; Port, H. *Synth. Met.* **1993**, 61, 71.
69. Kingsborough, R. P.; Swager, T. M. *Adv. Mater.* **1998**, 10, 1100.
70. Kean, C. L.; Pickup, P. G. *J. Chem. Soc., Chem. Comm.* **2001**, 815.
71. Orrellana, G.; Alvarez-Ibarra, C.; Quiroga, M. L. *Bull. Soc. Chim. Belg.* **1988**, 97, 731.
72. Alo, B.; Kandil, A.; Patil, P. A.; Sharp, M. J.; Siddiqui, M. A.; Snieckus, V.; Josephy, P. D. *J. Org. Chem.* **1991**, 56, 3766.
73. Sullivan, B. P.; Slamon, D. J.; Meyer, T. J. *Inorg. Chem.* **1978**, 17, 3334.
74. Buckingham, D. A.; Dwyer, F. P.; Goodwin, H. A.; Sargeson, A. M. *Aust. J. Chem.* **1964**, 17, 325.

75. Broomhead, J. A.; Young, C. G. *Inorg. Synth.* **1982**, 21, 127.
76. Atkins, P. W., Ed.; *Physical Chemistry, 4th Edition*; W. H. Freeman and Company: New York, 1990.
77. Zotti, G.; Martina, S.; Wegner, G.; Arnulf-Dieter, S. *Adv. Mater.* **1992**, 4, 798.
78. Chosrovian, H.; Grebner, D.; Rentsch, S.; Naarman, H. *Synth. Met.* **1992**, 52, 213.
79. Denisevich, P.; Abruna, H. D.; Leidner, C. R.; Meyer, T. J.; Murray, R. W. *Inorg. Chem.* **1982**, 21, 2153.
80. Slazner, U.; Lagowski, J. B.; Pickup, P. G.; Poirier, R. A. *Synth. Met.* **1998**, 96, 177.
81. MacLean, B. J.; Pickup, P. G. *J. Mater. Chem.* **2001**, 11, 1357.
82. Beck, J. L.; Humphries, A.; Sheil, M. M.; Ralph, S. F. *Eur. Mass Spectrom.* **1999**, 5, 489.
83. Harriman, A.; Romero, F. M.; Ziessel, R.; Benniston, A. C. *J. Phys. Chem. A* **1999**, 103, 5399.
84. Hopfgartner, G.; Piguet, C.; Henion, J. D. *J. Am. Soc. Mass Spectrom.* **1994**, 5, 748.
85. Lide, D. R. Ed.; *Handbook of Chemistry and Physics, 73rd Edition.*; CRC Press: Ann Arbor, 1992.
86. Bryant, G. M.; Fergusson, J. E. *Aust. J. Chem.*, **1971**, 24, 441.
87. Lytle, F. E.; Petrosky, L. M.; Carlson, L. R. *Anal. Chim. Acta* **1971**, 57, 239.
88. Fergusson, J. E.; Harris, G. M. *J. Chem. Soc. (A)* **1966**, 1293.

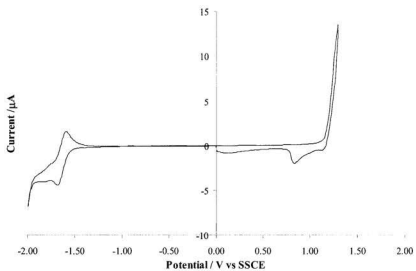
89. Seddon, E. A.; Seddon, K. R. Eds.; *The Chemistry of Ruthenium, Monograph 19*; Elsevier, Oxford, 1984.
90. Abruna, H. D. *J. Electroanal. Chem.* **1984**, 175, 321.
91. Li, C.; Shi, G.; Liang, Y. *Synth. Met.* **1999**, 104, 113.
92. Shi, G.; Li, C.; Liang, Y. *Adv. Mater.* **1999**, 11, 1145.
93. Li, C.; Shi, G.; Liang, Y. *J. Electroanal. Chem.* **1998**, 455, 1.
94. Collomb-Dunand-Sauthier, M.-N.; Deronzier, A.; Le Bozec, H.; Navarro, M. *J. Electroanal. Chem.* **1996**, 410, 21.
95. Cotton, F. A.; Wilkinson, G.; Murillo, C. A.; Bochmann, M. *Advanced Inorganic Chemistry*, 6th Ed. John Wiley & Sons, Toronto, 1999.
96. Nalwa, H. S. Ed.; *Handbook of Organic Conductive Molecules and Polymers, Volume 2. Conductive Polymers: Synthesis and Electrical Properties*; John Wiley & Sons: Toronto, 1997.
97. Bard, A. J.; Faulkner, L. R. Eds.; *Electrochemical Methods*; John Wiley & Sons: Toronto, 1980.
98. Lewis, T. J.; White, H. S.; Wrighton, M. S. *J. Am. Chem. Soc.* **1984**, 106, 6947.
99. EG&G Princeton Applied Research Electrochemical Instruments Group. Application Note AC-1: *Basics of AC Impedance Measurements*. 1984
100. Alberry, J.; Mount, A. R. Transmission Lines for Conducting Polymers. In *Electroactive Polymer Electrochemistry, Part 1*; Plenum Press: New York, 1994.
101. Ren, X.; Pickup, P. G. *J. Chem. Soc. Faraday Trans.* **1993**, 89, 321.
102. Ren, X.; Pickup, P. G. *J. Electroanal. Chem.* **1994**, 365, 289.

Appendix A

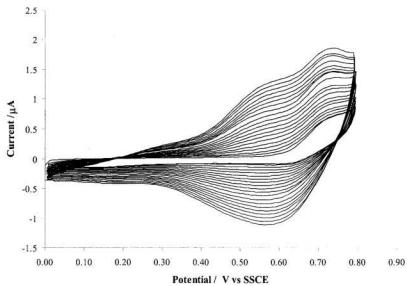
Cyclic Voltammograms



Electropolymerization of ca. 5 mM **btbmtz** in $\text{CH}_2\text{Cl}_2/0.1\text{M Bu}_4\text{NPF}_6$. $A=0.0052\text{ cm}^2$; $v=100\text{ mV sec}^{-1}$.

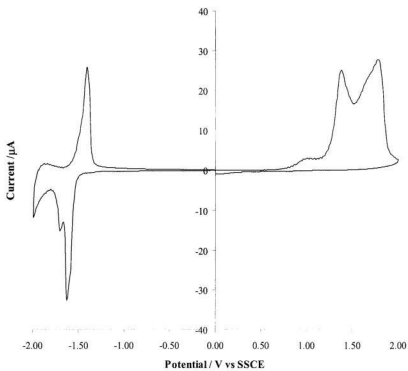


Cyclic voltammogram of ca. 5 mM **btbmtz** in CH₂Cl₂/0.1M Bu₄NPF₆. A=0.0052 cm²; v=100 mV sec⁻¹.

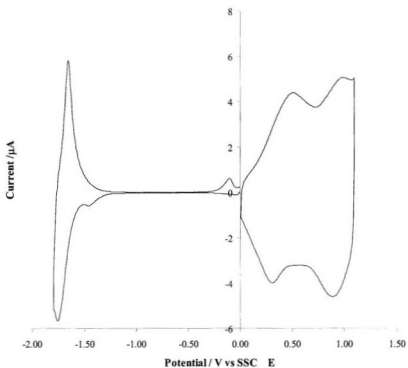


Electropolymerization of ca. 2.5 mM **bmtbmtz** in $\text{CH}_2\text{Cl}_2/0.1\text{M Bu}_4\text{NPF}_6$, $A=0.0052\text{ cm}^2$;

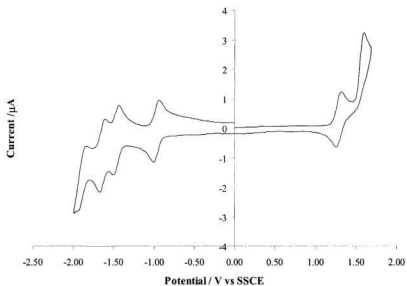
$\nu=100\text{ mV sec}^{-1}$.



P-doping and n-doping of a film of a poly-btbtz film ($\text{CH}_3\text{CN}/0.1\text{M Et}_4\text{NClO}_4$; $v=100\text{ mV sec}^{-1}$).

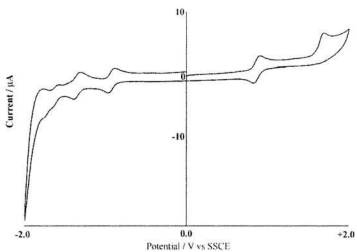


P-doping and n-doping of a film of a poly-bmtbmtz film ($\text{CH}_3\text{CN}/0.1\text{M Et}_4\text{NClO}_4$; $v=100\text{ mV sec}^{-1}$).



Cyclic voltammogram of ca. 1 mM $\text{Ru}(\text{btbmtz})(\text{bpy})_2(\text{PF}_6)_2$ in $\text{CH}_3\text{CN}/0.1 \text{ M Et}_4\text{NClO}_4$, $A=0.0052 \text{ cm}^2$.

$\nu=100 \text{ mV sec}^{-1}$.

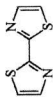
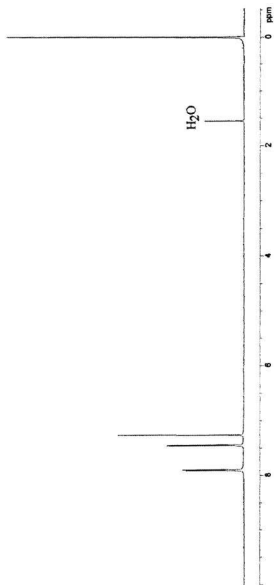


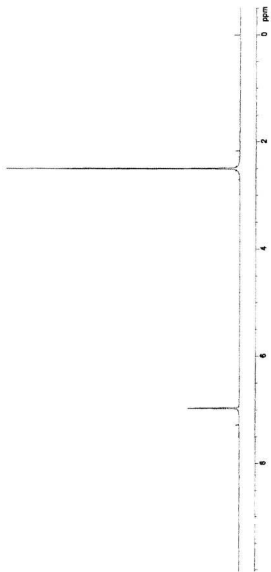
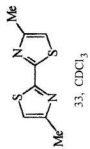
Cyclic voltammogram of 3.9 mM Os(**btbmtz**)(bpy)₂(PF₆)₂ in CH₃CN/0.1 M Et₄NClO₄. A=0.0052 cm².

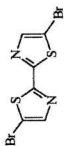
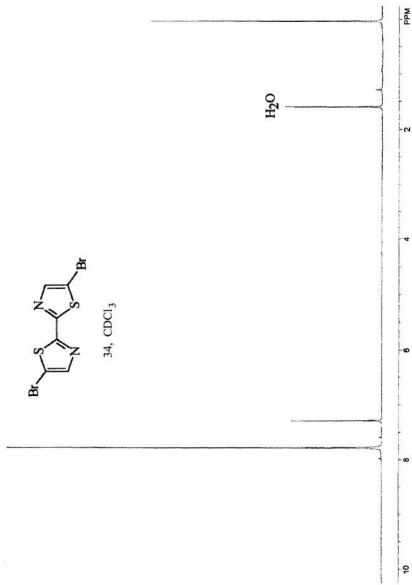
$\nu=100$ mV sec⁻¹.

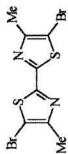
Appendix B

^1H NMR Spectra

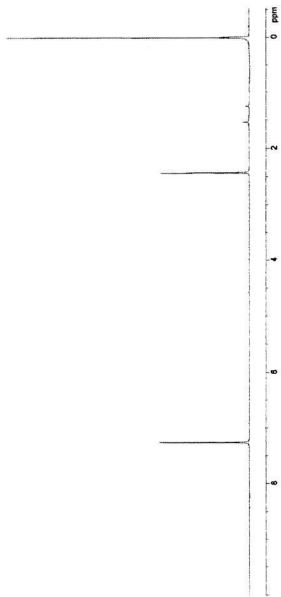
6, CDCl₃

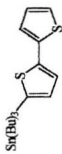
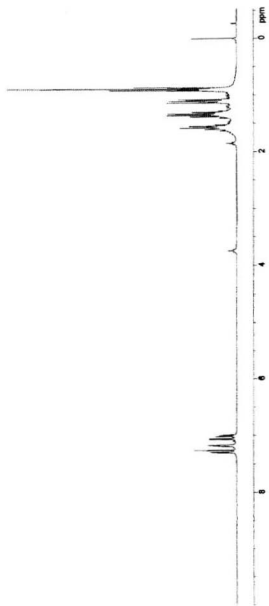


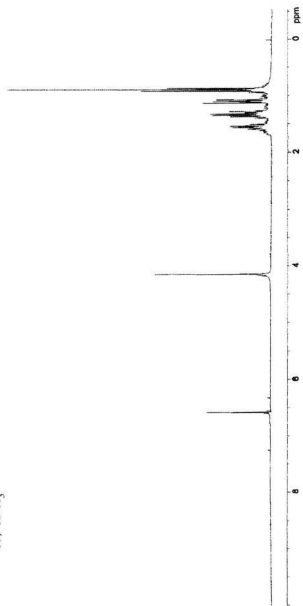
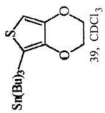
34, CDCl₃

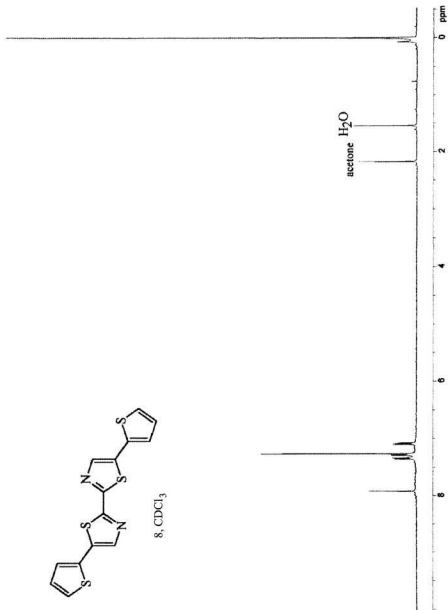
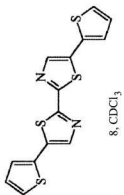


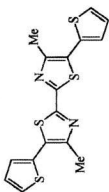
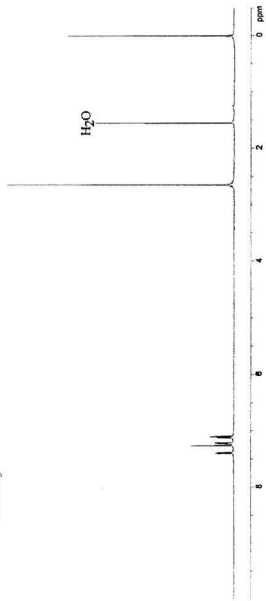
35, CDCl₃

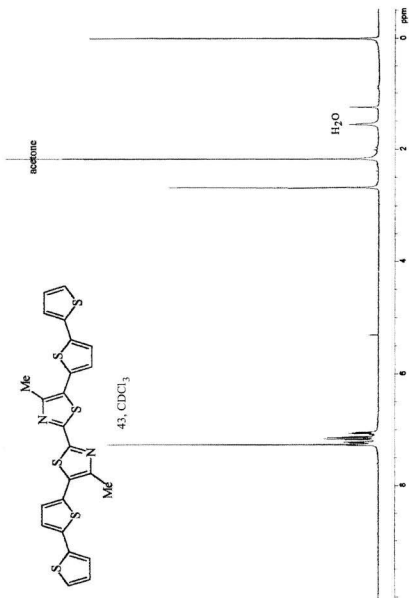


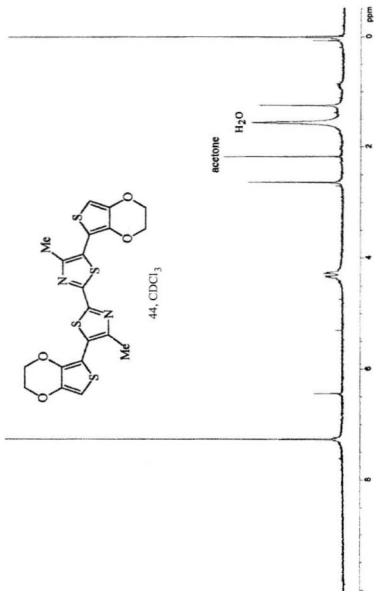
38, CDCl₃

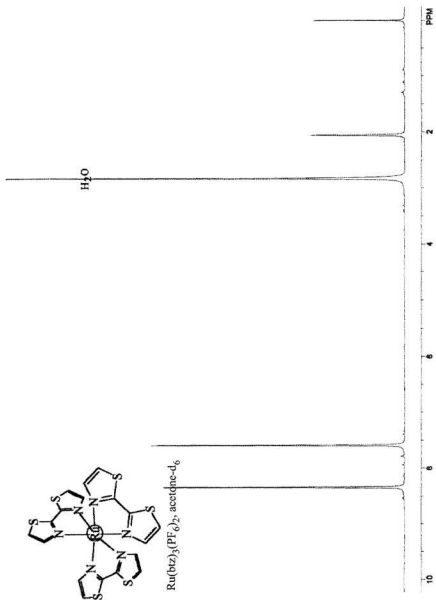


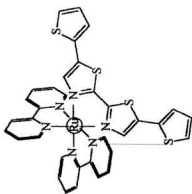


9, CDCl₃

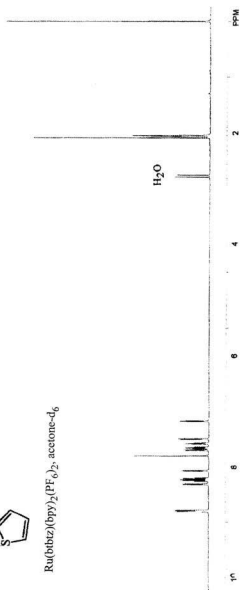


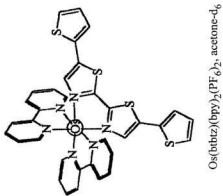


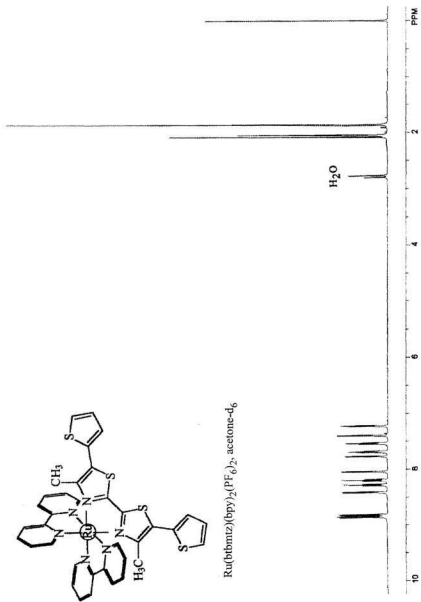


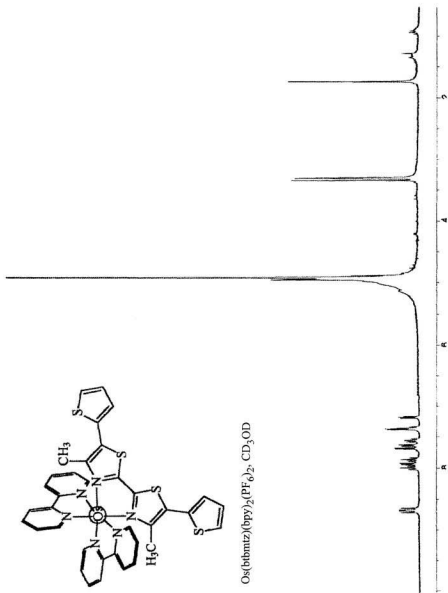


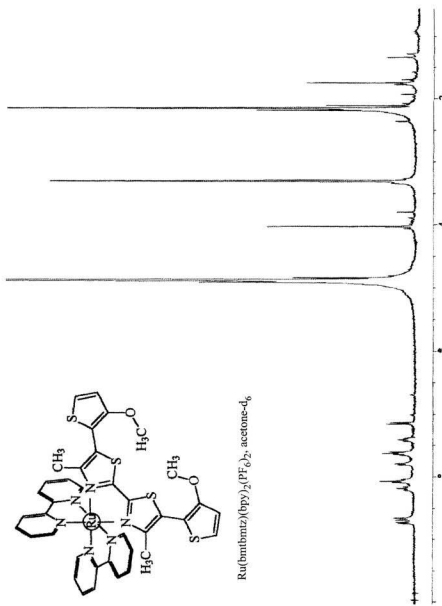
$\text{Ru}(\text{bbbz})(\text{bpy})_2(\text{PF}_6)_2$, acetone- d_6



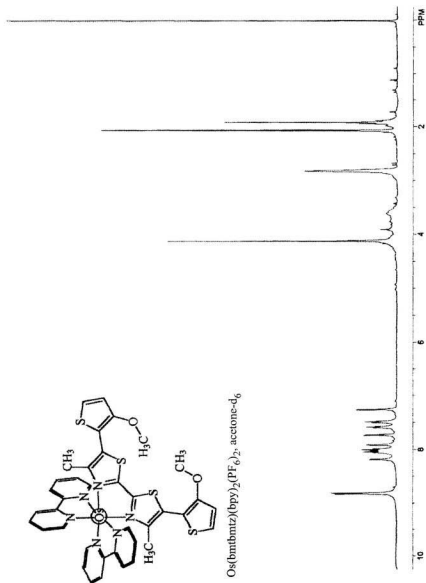








$\text{Ru}(\text{bmbmtz})(\text{bpy})_2(\text{PF}_6)_2$, acetone-d_6



Supplementary NMR Data**Ru(bpy)₃²⁺**

¹H NMR (300 MHz, CD₃OD): δ 8.72 (d, *J* = 8.0 Hz, 1H), 8.14 (dd, *J* = 8.1, 7.9 Hz, 1H), 7.83 (d, *J* = 5.7 Hz, 1H), 7.49 (dd, *J* = 8.0, 5.6 Hz, 1H).

Os(bpy)₃²⁺

¹H NMR (300 MHz, CD₃OD): δ 8.72 (d, *J* = 8.1 Hz, 1H), 7.94 (t, *J* = 7.8 Hz, 1H), 7.74 (d, *J* = 5.6 Hz, 1H), 7.40 (t, *J* = 6.7 Hz, 1H).

Ru(bmtz)(bpy)₂²⁺

¹H NMR (300 MHz, CD₃OD): δ 8.72 (d, *J* = 8.0 Hz, 1H), 8.66 (d, *J* = 7.9 Hz, 1H), 8.17 (t, *J* = 7.9 Hz, 1H), 8.06 (t, *J* = 8.0 Hz, 1H), 7.90 (d, *J* = 5.6 Hz, 1H), 7.78 (d, *J* = 5.5 Hz, 1H), 7.72 (s, 1H), 7.60 (t, *J* = 5.6 Hz, 1H), 7.40 (t, *J* = 6.6 Hz, 1H), 1.60 (s, 3H).

Ru(btbtz)(bpy)₂²⁺ (for Figure 4.4 data)

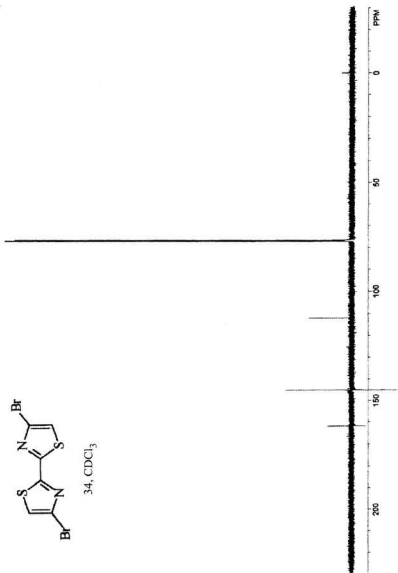
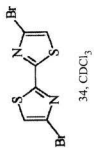
¹H NMR (300 MHz, CD₃OD): δ 8.76 (d, *J* = 8.1 Hz, 1H), 8.70 (d, *J* = 8.2 Hz, 1H), 8.23 (t, *J* = 7.9 Hz, 1H), 8.15 (d, *J* = 5.5 Hz, 1H), 8.08 (t, *J* = 7.9 Hz, 1H), 7.80 (d, *J* = 5.5 Hz, 1H), 7.71-7.63 (m, 2H), 7.46-7.37 (m, 2H), 7.19 (dd, *J* = 5.4, 5.2 Hz, 1H), 1.73 (s, 3H).

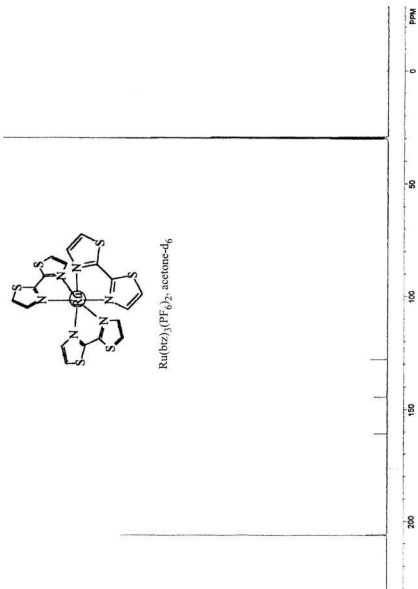
Ru(bmtbmtz)(bpy)₂²⁺

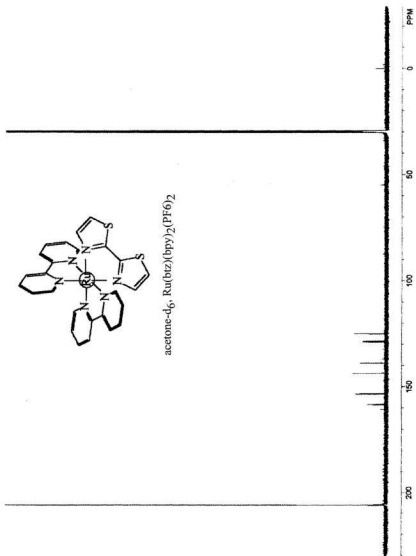
¹H NMR (300 MHz, CD₃OD): δ 8.73 (d, $J = 8.2$ Hz, 1H), 8.67 (d, $J = 8.0$ Hz, 1H), 8.18 (t, $J = 7.6$ Hz, 1H), 8.07 (m, 2H), 7.80 (d, $J = 5.9$ Hz, 1H), 7.67-7.59 (m, 2H), 7.41 (t, $J = 6.6$ Hz, 1H), 7.15 (d, $J = 5.4$ Hz, 1H), 4.03 (s, 3H), 1.75 (s, 3H).

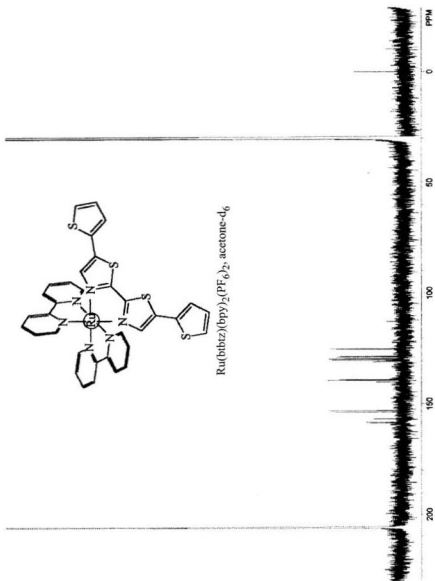
Appendix C

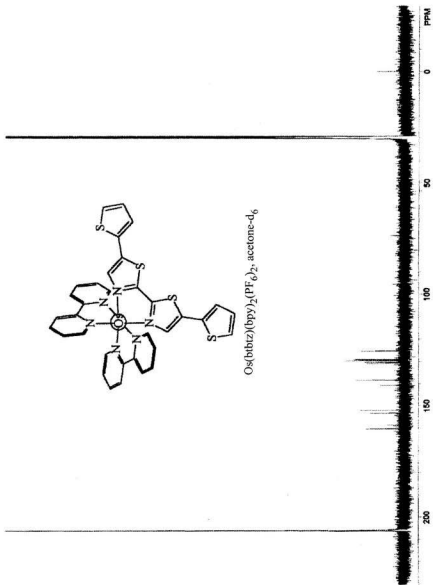
^{13}C NMR

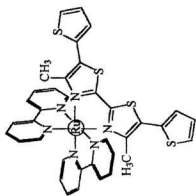




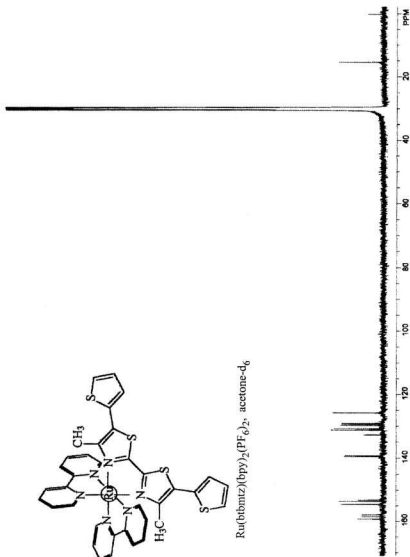






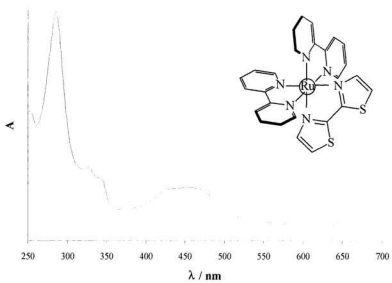
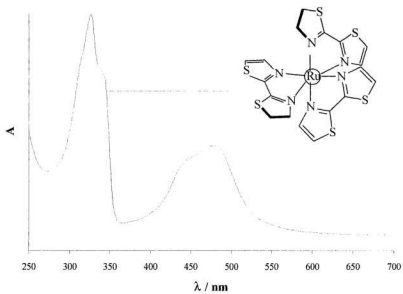


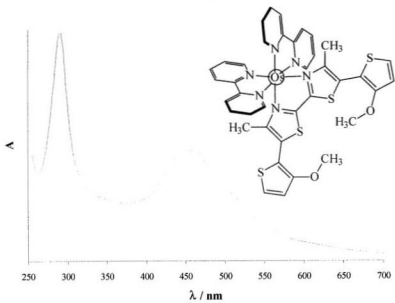
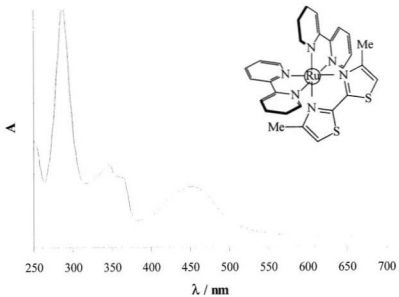
$\text{Ru}(\text{bibmtz})(\text{bpy})_2(\text{PF}_6)_2$, acetone-d_6



Appendix D

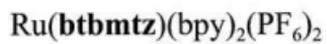
Electronic Absorption Spectra





Appendix E

X-Ray Crystallography Data for



Experimental

Collection, solution and refinement all proceeded normally. Hydrogen atoms were introduced in calculated positions with isotropic thermal parameters set twenty percent greater than those of their bonding partners at the time of their inclusion. They were not refined.

Data Collection

A deep red prism crystal of $C_{39}H_{34}N_6F_{12}P_2S_4RuO$ having approximate dimensions of 0.38 x 0.21 x 0.09 mm was mounted on a glass fiber. All measurements were made on a Bruker P4/CCD system with graphite monochromated Mo-K α radiation and a rotating anode generator.

Cell constants and an orientation matrix for data collection corresponded to a C-centered monoclinic cell with dimensions:

$$\begin{aligned} a &= 12.412(2) \text{ \AA} \\ b &= 28.471(4) \text{ \AA} & \beta &= 98.596(3)^\circ \\ c &= 12.486(2) \text{ \AA} \\ V &= 4363(1) \text{ \AA}^3 \end{aligned}$$

For $Z = 4$ and $F.W. = 1121.98$, the calculated density is 1.71 g/cm^3 . Based on the systematic absences of:

$$\begin{aligned} hkl: & h+k \pm 2n \\ h0l: & l \pm 2n \end{aligned}$$

packing considerations, a statistical analysis of intensity distribution, and the successful solution and refinement of the structure, the space group was determined to be:

C2/c (#15)

The data were collected at a temperature of $-80 \pm 1^\circ\text{C}$. The full hemisphere of data was collected with 30 sec., 0.3 deg. frames to a maximum 2θ value of 52.9° .

Data Reduction

Of the 10826 reflections which were collected, 4449 were unique ($R_{int} = 0.055$). The linear absorption coefficient, μ , for Mo-K α radiation is 7.2 cm^{-1} . The Siemens area detector absorption routine (SADABS) was used to correct the data with maximum and minimum effective transmissions of 0.9382 and 0.7722 respectively. The data were corrected for Lorentz and polarization effects.

Structure Solution and Refinement

The structure was solved by direct methods² and expanded using Fourier techniques³. The non-hydrogen atoms were refined anisotropically, Hydrogen atoms were included but not refined. The final cycle of full-matrix least-squares refinement⁴ on F^2 was based on 3295 observed reflections and 297 variable parameters and converged (largest parameter shift was 0.00 times its esd) with unweighted and weighted agreement factors of:

$$R1 = \Sigma ||F_o| - |F_c|| / \Sigma |F_o| = 0.079$$

$$wR2 = [\Sigma (w (F_o^2 - F_c^2)^2) / \Sigma w(F_o^2)^2]^{1/2} = 0.230$$

The standard deviation of an observation of unit weight⁵ was 1.02. The weighting scheme was based on counting statistics. The maximum and minimum peaks on the final difference Fourier map corresponded to 1.95 and $-1.06 \text{ e}^{-\text{\AA}^3}$, respectively.

Neutral atom scattering factors were taken from Cromer and Waber⁶. Anomalous dispersion effects were included in F_{calc} ⁷; the values for $\Delta f'$ and $\Delta f''$ were those of Creagh and McAuley⁸. The values for the mass attenuation coefficients are those of Creagh and Hubbell⁹. All calculations were performed using the teXsan¹⁰ crystallographic software package of Molecular Structure Corporation except for refinement, which was performed using SHELXL-97¹¹.

References

- (1) CrystalClear: Rigaku Corporation, 1999.
- (2) SIR92: Altomare, A., Cascarano, M., Giacovazzo, C., Guagliardi, A. (1994). *J. Appl. Cryst.*, 26, 343.
- (3) DIRDIF94: Beurskens, P.T., Admiraal, G., Beurskens, G., Bosman, W.P., de Gelder, R., Israel, R. and Smits, J.M.M. (1994). The DIRDIF-94 program system, Technical Report of the Crystallography Laboratory, University of Nijmegen, The Netherlands.
- (4) Least Squares function minimized: (SHELXL97)
- $$\sum w(F_o^2 - F_c^2)^2 \text{ where}$$
- $$w = 1 / [\sigma^2(F_o^2) + (0.1545 \cdot P)^2 + 10.8227 \cdot P]$$
- $$P = (\text{Max}(F_o^2, 0) + 2F_c^2) / 3$$
- (5) Standard deviation of an observation of unit weight:
- $$[\sum w(F_o^2 - F_c^2)^2 / (N_o - N_v)]^{1/2}$$
- where: N_o = number of observations
 N_v = number of variables
- (6) Cromer, D. T. & Waber, J. T.; "International Tables for X-ray Crystallography", Vol. IV, The Kynoch Press, Birmingham, England, Table 2.2 A (1974).
- (7) Ibers, J. A. & Hamilton, W. C.; *Acta Crystallogr.*, 17, 781 (1964).
- (8) Creagh, D. C. & McAuley, W.J. ; "International Tables for Crystallography", Vol C, (A.J.C. Wilson, ed.), Kluwer Academic Publishers, Boston, Table 4.2.6.8, pages 219-222 (1992).
- (9) Creagh, D. C. & Hubbell, J.H.; "International Tables for Crystallography", Vol C, (A.J.C. Wilson, ed.), Kluwer Academic Publishers, Boston, Table 4.2.4.3, pages 200-206 (1992).
- (10) teXsan for Windows version 1.06: Crystal Structure Analysis Package, Molecular Structure Corporation (1997-9).
- (11) SHELX97: Sheldrick, G.M. (1997).

EXPERIMENTAL DETAILS

A. Crystal Data

Empirical Formula	$C_{39}H_{34}N_6F_{12}P_2S_4RuO$
Formula Weight	1121.98
Crystal Color, Habit	deep red, prism
Crystal Dimensions	0.38 X 0.21 X 0.09 mm
Crystal System	monoclinic
Lattice Type	C-centered
Lattice Parameters	a = 12.412(2) Å b = 28.471(4) Å c = 12.486(2) Å β = 98.596(3) ° V = 4363(1) Å ³
Space Group	C2/c (#15)
Z value	4
D _{calc}	1.708 g/cm ³
F ₀₀₀	2256.00
μ (MoK α)	7.17 cm ⁻¹

B. Intensity Measurements

Detector	Bruker P4/CCD
Radiation	MoK α ($\lambda = 0.71073 \text{ \AA}$) graphite monochromated
Temperature	$-80 \pm 1^\circ\text{C}$.
Scan Rate	30s, 0.3 deg.frames
$2\theta_{\text{max}}$	52.9 $^\circ$
No. of Reflections Measured	Total: 10826 Unique: 4449 ($R_{\text{int}} = 0.055$)
Corrections	Lorentz-polarization SADABS Correction (trans. Factors: 0.9382 – 0.7722)

C. Structure Solution and Refinement

Structure Solution	Direct Methods (SIR92)
Refinement	Full-matrix least-squares on F^2
Function Minimized	$\sum w (F_o^2 - F_c^2)^2$
Least Squares Weights	$w = 1 / \{ \sigma^2(F_o^2) + (0.1545 \cdot P)^2 + 10.8227 \cdot P \}$ where $P = (\text{Max}(F_o^2, 0) + 2F_c^2)/3$
Anomalous Dispersion	All non-hydrogen atoms
No. Observations ($I > 2.00\sigma(I)$)	3295
No. Variables	297
Reflection/Parameter Ratio	11.09
Residuals: R1; wR2	0.079 ; 0.230
Goodness of Fit Indicator	1.02
Max Shift/Error in Final Cycle	0.00
Maximum peak in Final Diff. Map	$1.95 \text{ e}^-/\text{\AA}^3$
Minimum peak in Final Diff. Map	$-1.06 \text{ e}^-/\text{\AA}^3$

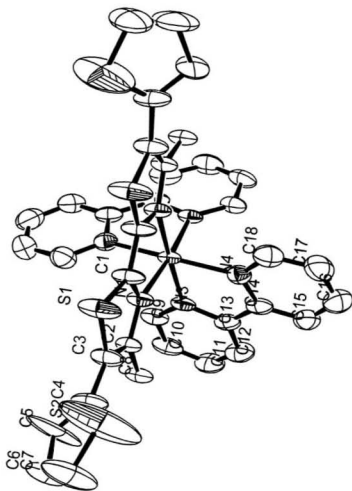


Table 1. Bond distances (Angstroms) for
Ru(btbtz)(bpy)₂(PF₆)₂

AtomA	B	Dist	ADC(A)	ADC(B)	Atom A	B	Dist	ADC(A)	ADC(B)
C1	N1	1.337	55501	55501	C17	C18	1.406	55501	55501
C1	C1	1.435	55501	65502	C18	N4	1.347	55501	55501
C1	S1	1.700	55501	55501	C18	C17	1.406	55501	55501
C2	C3	1.378	55501	55501	C19	C20	1.465	55501	55501
C2	N1	1.393	55501	55501	C20	C19	1.465	55501	55501
C2	C8	1.491	55501	55501	C20	C19	1.465	55501	55602
C3	C2	1.378	55501	55501	N1	C1	1.337	55501	55501
C3	C4	1.452	55501	55501	N1	C2	1.393	55501	55501
C3	S1	1.731	55501	55501	N1	Ru1	2.144	55501	55501
C4	C5	1.375	55501	55501	N3	C9	1.338	55501	55501
C4	C3	1.452	55501	55501	N3	C13	1.385	55501	55501
C4	S2	1.641	55501	55501	N3	Ru1	2.056	55501	55501
C5	C4	1.375	55501	55501	N4	C18	1.347	55501	55501
C5	C6	1.451	55501	55501	N4	C14	1.384	55501	55501
C6	C7	1.205	55501	55501	N4	Ru1	2.063	55501	55501
C6	C5	1.451	55501	55501	S1	C1	1.700	55501	55501
C7	C6	1.205	55501	55501	S1	C3	1.731	55501	55501
C7	S2	1.673	55501	55501	S2	C4	1.641	55501	55501
C8	C2	1.491	55501	55501	S2	C7	1.673	55501	55501
C9	N3	1.338	55501	55501	Ru1	N3	2.056	55501	55501
C9	C10	1.397	55501	55501	Ru1	N3	2.056	55501	65502
C10	C11	1.364	55501	55501	Ru1	N4	2.063	55501	55501
C10	C9	1.397	55501	55501	Ru1	N4	2.063	55501	65502
C11	C12	1.346	55501	55501	Ru1	N1	2.144	55501	55501
C11	C10	1.364	55501	55501	Ru1	N1	2.144	55501	65502
C12	C11	1.346	55501	55501					
C12	C13	1.398	55501	55501					
C13	N3	1.385	55501	55501					
C13	C12	1.398	55501	55501					
C13	C14	1.480	55501	55501					
C14	C15	1.376	55501	55501					
C14	N4	1.384	55501	55501					
C14	C13	1.480	55501	55501					
C15	C16	1.362	55501	55501					
C15	C14	1.376	55501	55501					
C16	C15	1.362	55501	55501					
C16	C17	1.381	55501	55501					
C17	C16	1.381	55501	55501					

Table 2. Bond angles (degrees) for Ru(**btbmtz**)(bpy)₂(PF₆)₂

Atom	A	B	C	Angle	ADC(A)	ADC(B)	ADC(C)
N1	C1	C1		118.62	55501	55501	65502
N1	C1	S1		115.06	55501	55501	55501
C1	C1	S1		126.28	65502	55501	55501
C3	C2	N1		113.96	55501	55501	55501
C3	C2	C8		125.03	55501	55501	55501
N1	C2	C8		121.01	55501	55501	55501
C2	C3	C4		130.13	55501	55501	55501
C2	C3	S1		110.35	55501	55501	55501
C4	C3	S1		119.51	55501	55501	55501
C5	C4	C3		131.68	55501	55501	55501
C5	C4	S2		105.96	55501	55501	55501
C3	C4	S2		120.54	55501	55501	55501
C4	C5	C6		111.76	55501	55501	55501
C7	C6	C5		113.15	55501	55501	55501
C6	C7	S2		112.00	55501	55501	55501
N3	C9	C10		122.34	55501	55501	55501
C11	C10	C9		118.96	55501	55501	55501
C12	C11	C10		120.22	55501	55501	55501
C11	C12	C13		120.17	55501	55501	55501
N3	C13	C12		120.36	55501	55501	55501
N3	C13	C14		115.17	55501	55501	55501
C12	C13	C14		124.47	55501	55501	55501
C15	C14	N4		121.80	55501	55501	55501
C15	C14	C13		123.77	55501	55501	55501
N4	C14	C13		114.42	55501	55501	55501
C16	C15	C14		120.52	55501	55501	55501
C15	C16	C17		118.66	55501	55501	55501
C16	C17	C18		119.81	55501	55501	55501
N4	C18	C17		121.48	55501	55501	55501
C19	C20	C19		126.00	55501	55501	55602
C1	N1	C2		110.61	55501	55501	55501
C1	N1	Ru1		112.06	55501	55501	55501
C2	N1	Ru1		137.33	55501	55501	55501
C9	N3	C13		117.95	55501	55501	55501
C9	N3	Ru1		126.85	55501	55501	55501
C13	N3	Ru1		115.20	55501	55501	55501
C18	N4	C14		117.64	55501	55501	55501
C18	N4	Ru1		126.78	55501	55501	55501
C14	N4	Ru1		115.43	55501	55501	55501
C1	S1	C3		89.91	55501	55501	55501

AtomA	B	C	Angle	ADC(A)	ADC(B)	ADC(C)
C4	S2	C7	95.16	55501	55501	55501
N3	Ru1	N3	85.88	55501	55501	65502
N3	Ru1	N4	79.77	55501	55501	55501
N3	Ru1	N4	92.60	55501	55501	65502
N3	Ru1	N1	97.90	55501	55501	55501
N3	Ru1	N1	174.55	55501	55501	65502
N3	Ru1	N4	92.60	65502	55501	55501
N3	Ru1	N4	79.77	65502	55501	65502
N3	Ru1	N1	174.55	65502	55501	55501
N3	Ru1	N1	97.90	65502	55501	65502
N4	Ru1	N4	169.64	55501	55501	65502
N4	Ru1	N1	91.94	55501	55501	55501
N4	Ru1	N1	96.08	55501	55501	65502
N4	Ru1	N1	96.08	65502	55501	55501
N4	Ru1	N1	91.94	65502	55501	65502
N1	Ru1	N1	78.62	55501	55501	65502

